University of study of Catania

PhD School – Materials science and nanotechnology

XXXV CICLO

Ph.D. Thesis

Anisotropic noble metal nanoparticles for plasmon sensing

Mario Pulvirenti

Ph.D. Coordinator: Prof. G. Compagnini

Tutor: Prof. G. Compagnini

Abstract

Sensors based on surface plasmon resonance (SPR) has received considerable attention due to their prompt responses and because they do not need complex and high cost instrumentation to work properly. In particular the high sensitivity of the plasmon band position due to refractive index changes is not only the most studied effect, but the most relevant one.

In the first part of this thesis, I will show some different synthesis methodologies to produce anisotropic noble metal nanoparticles. Particularly the attention will be focused on the synthesis of anisotropic silver nanoparticles through seed mediated growth and laser ablation in liquids. Nanoparticles obtained with both methods will be characterized from optical e morphological point of view.

The second part of the thesis is devoted to describe the correlations between optical and morphological features of the produced nano-systems, while the third part will be focused on the development of a sensor device, based on the plasmon sensitivity properties of silver anisotropic nanoparticles. In particular I will present a cost-effective, reusable, and high-responsive SPR device based on silver nanoplates paved PMMA cuvettes.

The same method will be used for glass cuvettes for which specific biosensor device based on the biotin-avidin interaction is presented. The results shown can serve as a first step and proof in order to develop low cost plasmonic sensor device based on refractive index changes suitable for a future integration and miniaturization.

Introduction: The breakthrough of noble metal nanoparticles

Nanoparticles (NP) are generally defined as any particulate material for which at least one dimension lies in the range of 1–100 nm. They can exist in various shapes, such as spheres, rods, wires, planes, stars, cages, multipods, etc. The various chemical processes that guide the synthesis of materials in the nanometre scale can be defined as nano chemistry, which plays a critical role in tailoring the physical and chemical properties of nanoparticles. Nanoparticles have several unique properties not found in their bulk counterparts, which include high surface-to-volume ratio, high surface energy, unique mechanical, thermal, electrical, magnetic, and optical behaviours, etc[1]. Their chemical reactivity and dispersibility in various solvents can be regulated by modifying their surface with desired functional groups to suit a particular application. The fundamental properties of the nanoparticles and nanostructures are functions of not only the size but also nanomorphology, as described by the shape (dimensional anisotropy), structure, crystallinity, and phase of the nanomaterial. This gives an opportunity to generate new properties and tune these properties by varying the morphology of the nanomaterials. Dramatic changes in the properties of metallic nanomaterials may result from small changes in their morphologies. Chemists are familiar with the relationships among valence, stoichiometry, molecular geometry (i.e., the way the atoms or molecules arrange themselves), and reactivity of molecules and solids. The molecular morphology has been observed toaffect the properties of polymeric materials. Similarly, in nanomaterials where a few tens to hundreds of atoms (or molecules) are put together as a single entity, it is logical to expect that the particle morphology will be an important factor in determining the properties of the nanomaterials. However, in nanoparticles, the surface energy becomes a major player in determining the particle geometry unlike the valence shell electron pair repulsion and bond energy in the molecules (and small clusters), because of the larger size of the nanoparticles compared to the molecules (and clusters). The size domain of nanoparticles matches a multiple of the de Broglie wavelengths of the electrons, phonons, and excitons propagating in them. This leads to the spatial confinement of the electrons, phonons, and electric fields in and around these particles and the quantum effects begin to dominate. For example, the electron confinement effect in a nanoparticle modifies its spectral properties via shifting of quantum levels and change in transition probabilities[2]. Nanoparticles have very large surface area-to-volume ratio because of their small sizes. The large ratio of surface area to volume affects their individual as well as interaction properties. Surface atoms have coordinatively unsaturated dangling bonds. Furthermore, nanoparticles bear a high fraction of edge- and cornerlike curved regions[3]. Edges and corners have more coordinatively unsaturated atoms (dangling bonds) than the flat surfaces. Large fractions of undercoordinated surface, corner, and edge atoms in a nanoparticle increase the surface energy and affect its surface bonding properties and chemical reactivity. The surface of a nanoparticle can be unstable due to the high surface energy and large surface curvature. This may cause deviations from the usual bulk atomic arrangements. Large surface area and changed electronic properties are very important in the context of catalysis, active sites, adsorption, and electrode activities. Properties such as particle–particle or particle–environment interactions are affected by the large surface area-to-volume ratio as well as spatial confinement phenomena. Nanoparticles of complex morphologies are essentially in kinetically frozen states with metastable structures [4] and offer characteristic orientational confinements and further modifications in the internal structures and surface characteristics. Nanomaterials, in particular the ones that are composed of metallic atoms such as silver, gold and copper show an interesting optical property that is called plasmon resonance. These metallic nanomaterials were used from the ancient time, for example and maybe the most famous is the Lycurgus cup (400 A.C.) in which are present silver and gold nanoparticles and in particular, this object exhibit different colours based on interaction with light, for example in transmitted light the cup becomes red instead in reflection green[4]as shown in figure 1.

Figure 1: Lycurgus cup in reflection and transmission, image taken from British museum

The reason tied to this phenomenon remains undiscovered until the 20th century and in 1990[5]the scientists with Transmission Electron Microscope (TEM) they found the presence of gold and silver nanoparticles that explain the dichroism of the Lycurgus cup. Beside how mankind in history have used nanoparticles, it is interesting to understand how metallic nanoparticles can be applied into many applications such as catalysis, sensors, biomedical and photovoltaics due to their optical and electronic properties above all the plasmon resonance which is the key to combine all kind of metallic nanoparticles with the so cited applications[6]. From a historical point of view the first person who has introduced the concept on nanotechnology was the noble prize Richard Feynman in 1959 and presented a lecture entitled “There is a plenty’s of room at the bottom”. During the lecture he exposed an idea in which where was possible to construct materials that had similar dimension just like molecules. After that lesson, his own hypothesis was correct and for this reason Feynman nowadays is considered the father of nanotechnology. The first man who used and gave the definition to the word “nanotechnology” was Norio Taniguchi. He thought that it could be possible to transform macroscopic materials into nanoscopic ones as the atoms or molecule. The union of these two currents of thought lead to the modern ways to synthetize nanomaterials: bottom up and top-down synthesis method. These two methods open many possibilities to create many different nanomaterials and they are fundamentals to understand the final properties of the nanomaterials synthetized. Strict control of the nanoparticle morphology is therefore required to obtain materials of desired properties. In other words, one can generate particles with new properties from the same materials and can fine-tune the properties of the nanoparticles by simply tuning the nanoparticle morphology.

Chapter 1: Metal nanoparticles: synthesis, properties and applications

Due to their interesting properties and small volume of nanoparticles (NPs) have made them desirable for a lot of studies and applications in many frontiers scientific and technological fields. The synthesis route is crucial in tuning the volume as well as the properties of NPs. Many properties, that normally for bulk materials are known to be constant, vary with the size, shape, and surface structure of the nanomaterials. For this reason, one needs to develop the synthesis methodologies that can produce NPs of precisely controlled size, shape, crystal structure, surface chemistry, and chemical composition. During the past years this has prompted the researchers to produce an impressive range of NPs through various physical and (bio)chemical methods of synthesis. With the progress in synthesis, many exciting new nanomaterials with unique properties have been generated, which in turn has initiated numerous new scientific studies and technological applications. NPs can be produced in the solid, liquid, solution, or gaseous state, by following two basic approaches: top-down and bottom-up synthesis route.

1.1 Classification and some common synthesis methods

A lot of different NMNPs has become available due to the many synthetic efforts over the years. However, it does not exist any nomenclature and classification systems. The composition of nanomaterials has been used frequently as the basis for their classifications, and there are a lot of compositions like, monometallic, bimetallic, metal oxide, magnetic, semiconductor, hybrid, composite. Another common way to give names to nanomaterials is related to the geometrical parameters such as shape and size. Indeed, it is possible to find nanorods[7,8],nanowires[9,10],nano-dumbbells, nano-cubes, tetrahedra, decahedra, icosahedra, octahedra, prisms, pyramids, stars, multipods, nano-cages, striped particles, core–shell and so on[11–13]. In figure 1 are reported some structure of noble metal nanomaterials.

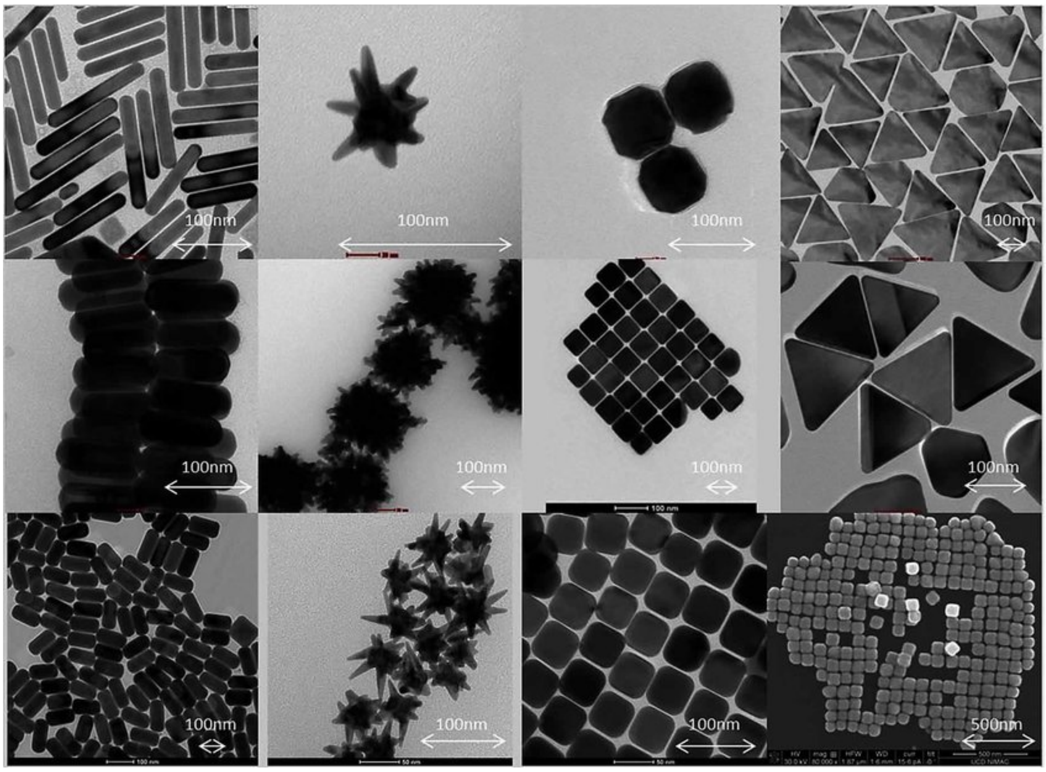

Figure 1: Different structures of noble metal nanoparticles (taken from the book "Emerging research on Bioinspired Materials Engineering[14] *(pp. 35-68)*

Differently, the synthesis methods are generally well classified, thus distinguishing between physical and chemical methods or (more commonly) between top-down or bottom-up approaches. In the top-down approach, one achieves structure sizes in the medium to lower nanometer range, starting from large materials entity and using physical or lithographic principles. A typical example of top-down synthesis is that obtained by performing a laser ablation procedure in a liquid medium (Pulsed Laser Ablation in liquids or PLAL). PLAL is based on the ejection of material by a laser pulse irradiating a solid target immersed in liquid[15,16]. The laser matter interaction and the consequent ablation are strongly dependent on the irradiance and the duration of the pulse, on the background liquid, on the sample geometry and morphology as well as on the focusing condition. Fig. 2 schematically illustrates these processes.

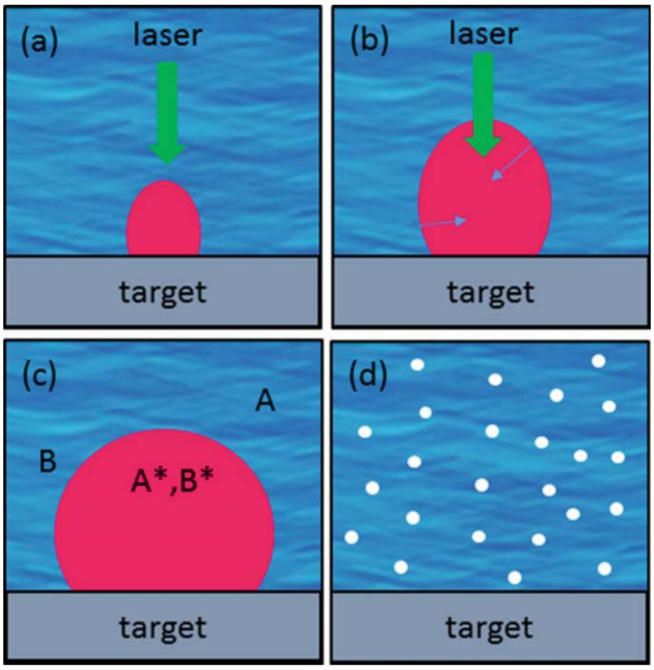

Figure 2: Scheme of liquid laser ablation synthesis method picture taken fromLaser Micro-NanoManufacturing and 3D Microprinting[17]

In the bottom-up approach, ionic, atomic, and molecular units assemble through various processes to form structures of nanometer length scale. The bottom-up approach in essence is the chemical synthesis method. In this approach, chemical synthesis principles are primarily employed starting from the generation of the constituents to their growth into nano entity. In principle bottom-up approach allows to produce and design nanoparticles(NPs) of any size and morphology deposition of the constituents unit-by-unit. This approach offers an opportunity and allows to understand the aspects of the morphology development and the structure–

property relationship in a particle from atomic/molecular point of view. The bottom-up solution-phase synthesis methods are often and denoted as chemical colloidal methods because they involve precipitation of nanometer-sized particles within a continuous solvent matrix forming colloidal sols. The materials produced with chemical colloidal methods are suitable for further processing; this is essential and allows the integrations of NPs in complex systems and devices. Indeed chemical colloidal methods have been preferred methods for producing a wide-ranging NPs and nanocomposites of a variety of materials (e.g., metals, alloys, intermetallic, semiconductors, and ceramics). Chemical colloidal synthesis routes have been extensively employed to prepare metal NPs, especially noble metal nanoparticles. (NMNPs).The synthesis of chemical colloidal NPs basically involves the (bio)chemical reduction of metal salts, photochemical and electrochemical pathways thermal decomposition of metallic compounds in aqueous or organic solvents in the presence of a variety of additives, such as surfactants, ligands and polymers. In the next sections will be described different synthesis methodologies starting from the most common and one so far which is the chemical reduction method. From the basic concepts of this one, they will be created some new other method with the goal to further improve the particle morphology.

1.1.2 Chemical reduction method

In the chemical reduction methods, inorganic and organic chemical reducing agents are used to prepare NMNPs and in the figure 3 below is reported the typical evolution process of NMNPs occurring during chemical reduction. Reduction reactions may occur at room or elevated temperatures, reducing reaction requirements depends on the strength of the reducing agents.

One of the most well-known techniques for the synthesis of AuNPs is based on the reduction of $HAuCl_4$ by citrate in water. This was first designed by Turkevich[18] in 1951. In this method, the HAuCl4 solution is boiled, and the trisodium citrate dihydrateis then rapidly added into the boiling solution under vigorous stirring. After a few minutes, the color of the solution changes from light yellow to wine red. This method results in AuNPs measuring about 20 nm in diameter. In this technique, citrate ions play a double role, as both stabilizing and reducing agents, in the figure 3 is reported the formation of the NPs during chemical reduction process.

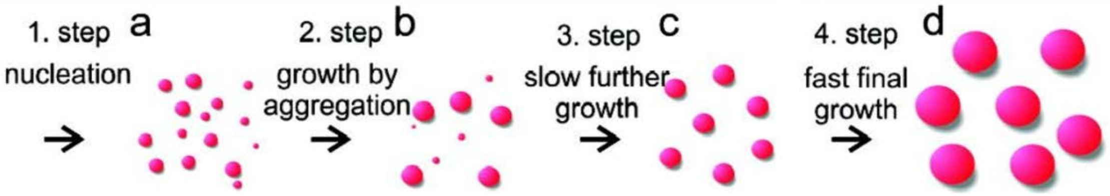

Figure 3: Typical evolution process occurring during the chemical reduction method[19]

From chemical reduction method the scientists have developed some advanced synthesis technique like template approach (or template-directed synthesis), preformed seed-mediated synthesis (or seeding growth method), and high-temperature reduction method, particularly polyol synthesis method. Such chemical reduction improved methods have produced the most diverse sets of particle morphologies.

1.1.3 - Template directed synthesis.

By using media/templates it can be possible to direct the growth of NPs. Indeed, the particle morphology depends on many factors when a template is used. The main factor is the structure of the template and plays a major role in determining the resulting particle morphology. Template agents commonly are called guiding agent. Some templates provide spatially and dimensionally constrained structures that simply function as reaction cages or platforms, thereby physically restricting NP growth in particular dimensions or geometries[20,21]. For some templates, their chemical properties are used for the control of nucleation and growth of the new particles[22,23]. Templating has been demonstrated to be a good strategy for make particles with different morphologies[24]. Using template agents appears to be an effective strategy for building nanoscale structures and architectures with more complex hierarchy, since physical structures are used for guiding the nucleation and growth in this case. A diverse range of templates can be employed for the controlled synthesis of NPs, which can be divided into two types: hard and soft templates as shown in figure 4.

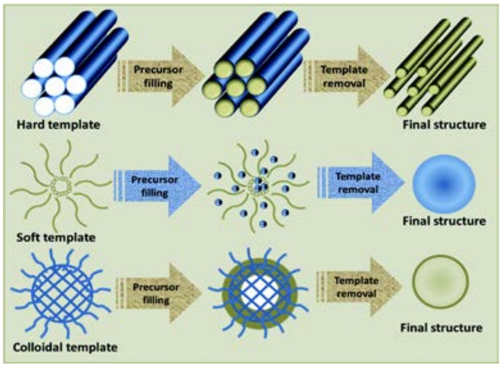

Figure 4: template directed synthesis schemes in which are represented three different templates(picture taken from ref)[25]

Some examples of hard templates are preformed NPs, dielectric colloids, carbon nanotubes (CNTs), and porous membranes such as polymer and alumina films containing track-etched channels and pores. Preformed metal NPs for the size and morphology-controlled synthesis of new NPshave been used and becomes part of the new particle and in such cases can undergoes to destructive chemical transformations during the new particle formation.

The preformed metal NPs, commonly, are called seeds and instead of templates they become part of the new particles. On the other hand, the preformed NPs are called sacrificial templates, if they undergo chemical transformations in the process of new particle formation. Dielectric colloids, such as polystyrene, poly-(methyl methacrylate), silica spheres and so on, have been used as templates for the nucleation and growth of varied thickness nano shells of noble metals on their surfaces[26,27]. In most of the cases, epitaxial growth conditions for NMNPs are not met on the surfaces of dielectric colloid templates. It is therefore necessary to modify the template surface with some metal ion binding agents that accumulate metal ions around the template via coordination or electrostatic interactions. Then, the metal ions are reduced by suitable reducing agents leading to the nano shell formation via direct nucleation[28,29]. In some cases, preformed seed particles have been first attached to the surface-modified dielectric colloid templates to facilitate templated development of the nano shell morphology. Carbon nanotubes have also been used to template metallic nanostructures providing both the outside surface and the hollow interior as scaffolds for the deposition of other materials[30].

1.1.4-Seed mediated growth

Preformed seed-mediated synthesis method is a very popular chemical colloidal method that has been employed for the preparation of NMNPs with different morphologies[31,32]. This method allows manipulation of the particle size and the aspect ratio, for 1D nanostructures[33–35]. In the seeding growth method (SGM), preformed fine metal particles are added to an appropriate growth solution for further growth as seeds. The seed particles are often produced by reducing metal ions by a suitable reducing agent. The growth solutions contain the same or different metal ion(s) along with other additives such as dopants, capping and etching agents, and so on. By varying the quantity and the features (e.g., internal structures, facets, composition, and size) of the seeds in the growth solution, NMNPs of different sizes and shapes can be prepared[16,36–39]. In the nucleation and growth of the crystal formation, the formation of seed nuclei and their growth occur generally consecutively in the next section it will be seen in detail the mechanisms of nucleation and growth. A variation of the preformed seed-mediated method, in situ seeding method has also been reported[40,41]. In this method, seed particles are generated in the growth solution itself, not in a separate step, by introducing a small quantity of a strong reducing agent to initiate the homogeneous nucleation in the reaction solution. A mild reducing agent is already present in the reaction solution and carries forward the growth of the seeds by the reduction of additional metal ions present in the reaction solution. Nanorods/nanowires; rectangle-, cube-, and tetrapod like gold NPs; and silver nanoplates and disks have been synthesized in aqueous solution at room temperature by this method. In the experimental part I will discuss in more comprehensive way this synthesis method.

1.1.5)- High temperature Reduction method

Some reagents such as oxidizable solvents (e.g., polyols, dimethylformamide (DMF)), polymers (e.g., polyvinyl alcohol (PVA)), and citric acid show weak reducing behaviour at room temperature toward most of the metal precursors. Indeed, several metal ions can be reduced at elevated temperature by using these weak reducing agents[42,43]. Polyol reduction method, which involves refluxing a solution of the metal precursor in ethylene glycol

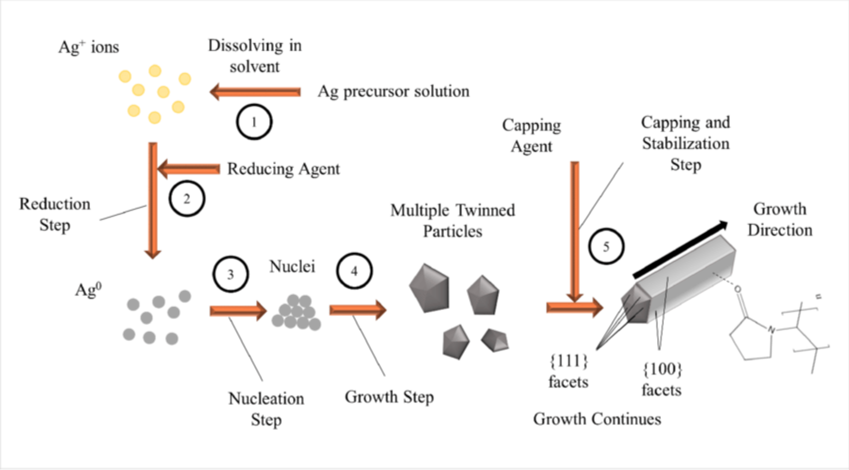

Figure 5: Polyol synthesis method picture taken from ref[44]

or larger polyols, is one of the popular methods of morphology-controlled NP synthesis as shown in the figure 5. In most of the cases, these reagents play multiple roles, such as of solvent, reducing agent, dispersing agent, and so on. Depending on the reduction potentials of the metal precursor and the weak reducing agent system, the temperature and time required for reduction process vary[45]. Metal NPs with various morphologies have been prepared using these methods.

1.1.6- Galvanic displacement method

Galvanic replacement method is based on electrochemical reaction without the application of the electric current from an external source but utilizing potential difference between the plating metal and the substrate (template). This method originates from the early publication by Brenner and Riddell[46] and has attracted increasing attention over the past 60 years owing to its simplicity and low cost for many applications, such as electroless nickel and copper deposition, in electronics. Electroless plating may happen through three different mechanisms: autocatalytic, substrate-assisted catalyzed, and the galvanic replacement[10]. The galvanic replacement reaction can be carried out in the absence of any additional reducing agent and is a one-step process driven by the standard electrode potential differences between the elements and resulting in the deposition of noble metals at the cost of dissolution of the less noble metal component[10]. The deposition process of a metal from aqueous solution thus involves both oxidation and reduction of two different metals/metal ions. The less noble metal component serves as pre-synthesized template that is oxidized under loss of electrons, while the reduction half-reaction is characterized by the gain of electrons and concomitant deposition of noble metals. After these initial reports, researchers have made several important additions to the sacrificial template-mediated synthesis of hollow/porous morphologies. For example, use of Ag NP sacrificial templates and $HAuCl_4$ gives rise to insoluble AgCl species, which contaminate the shell formation process. Several practical improvements have been proposed to avoid the insoluble AgCl problem[47,48]. For example, when the redox reaction was carried out in an organic solvent, displacement between Ag NP templates and Au^{3+} ions occurred at room temperature and did not result in AgCl precipitates[48]. The resulting metal replacement process is a simple and facile method to deposit noble metal materials on differently sized and shaped less noble metal templates, which is especially suitable for producing nano-catalysts. In the following figure 6 is reported a typical bimetallic nanoparticle synthesis by galvanic displacement reaction.

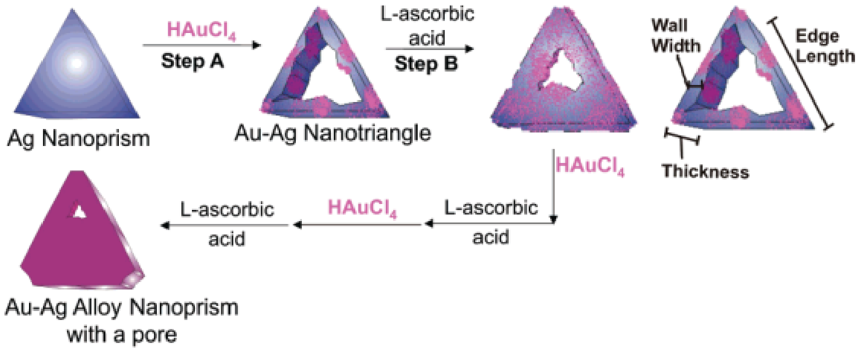

Figure 6: Hollow bimetallic nanostructures obtained by using galvanic displacement method picture taken from ref[49]

1.1.7 Final remarks about synthesis

These multiple synthesis approach, allows a wide tunability of both the dielectric core size and the shell thickness. This in turn allows a high degree of localized surface plasmon resonance (LSPR) tunability from the visible to the near-IR region. In the next chapter will be introduced some simple concept about plasmon resonance.

1.2) Optical properties of metal nanoparticles and the plasmon resonance phenomenon

1.2.1) Surface plasmons

Surface Plasmons (SP) resonance consists of a collective oscillation of conduction electrons excited by the electromagnetic field of light. SP resonance is in the origin of optical properties hardly achievable with other physical processes[50–52]. In the case of metallic nanoparticles, where the electrons are confined in the three dimensions, the electron oscillations induce an electric field around the NP that can be much larger than the incident light one. SP represents one of the best examples that things are different at the nanoscale. The optical properties of a metallic particle when the size is reduced to the few nanometres range, are dramatically modified by the appearance of SP and its behaviour results completely different than the bulk metal one. SP open the possibility to amplify, concentrate and manipulate light at the nanoscale, overcoming the diffraction limit of traditional optics and increasing resolution and sensitivity of optical probes[53]. For these reasons SP can be used in a wide range of fields, including biomedical[54–57], energy[58–60], environment protection[61–63], sensing[64] and information technology[52,53,65] applications. The exact resolution of Maxwell equations with the appropriate boundary conditions[50] is needed to analyse SP and the solution of these equations is only possible for certain conditions and the results are mathematical series that do not explain from a physical what SP are. Metallic NPs can be described as a lattice of ionic cores with conduction electron moving almost freely inside the NP. The electromagnetic field of the light exerts a force on these conduction electrons moving them toward the NP surface this phenomenon happens when metallic nanoparticles are under illumination. Under these conditions the electrons, that normally are confined inside the NP, moves towards one side of the surface creating an electric dipole. This dipole generates an electric field inside the NP opposite to that of the light that will force the electrons to return to the equilibrium position (figure 7). The larger the electron displacement, the larger the electric dipole and consequently the restoring force. The situation is like a linear oscillator with a restoring force proportional to the displacement from the equilibrium position. If the electrons are displaced from the equilibrium position and the field is later removed, they will oscillate with a certain frequency that is called the resonant frequency; in the case of SP it is named the plasmonic frequency. The electron movement inside the NP exhibits some damping degree. The ionic cores and the NP surface partially damp the electron oscillations. Thus, the system is like linear oscillator with some damping.

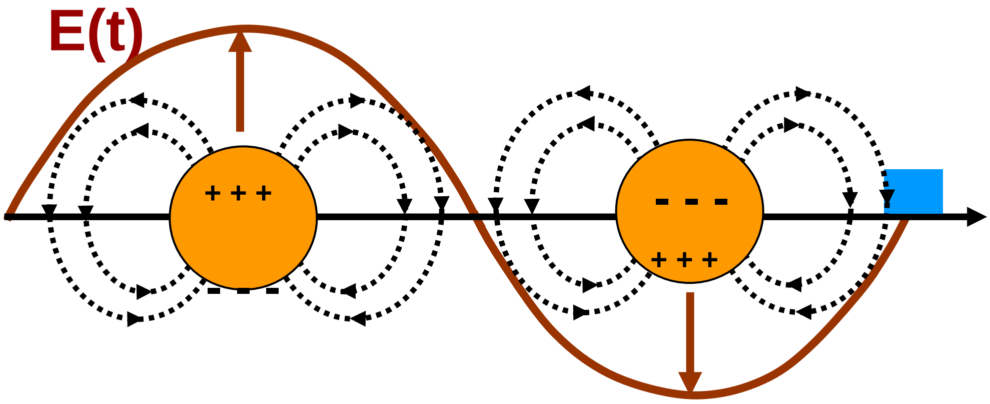

Figure7 : Interaction between light and metal nanoparticles

When an alternating force is applied to a linear oscillator, the system oscillates with the same frequency than the external force, but the amplitude and phase will depend on both the force and the intrinsic parameters of the oscillator. In particular, the oscillating amplitude will be maxima for the resonant frequency (figure 8a).

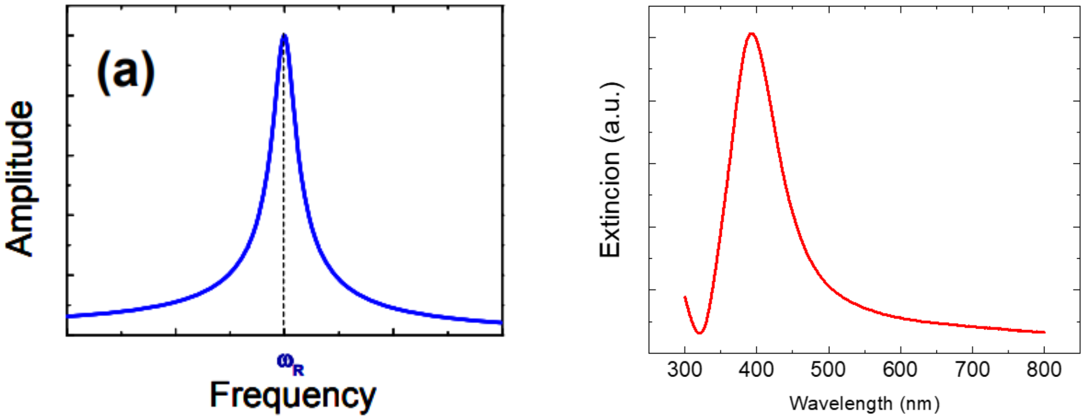

Figure 8a: Typical oscillation amplitude for a linear oscillator 8b: Plasmon resonance spectrum of silver spherical nanoparticles

It is quite straightforward to understand that if the frequency of the external force is the same that the plasmonic frequency of the NP, it will be easy to make the electrons oscillate, but as we move far away from this frequency the movement of electrons will be more difficult, with reduced amplitude. It is impossible to directly observe the electrons movement to determine their oscillating amplitude, but, it can be determined this amplitude indirectly because the electronic oscillation implies an increase of kinetic and electrostatic energies associated to the electric fields of the dipole. Therefore, the light extinguishes partially when exciting SP inside the NP. The larger the electron oscillations, the larger the light extinction, so the optical absorption spectrum allows to detect the excitation of SP. The resonant frequency for these oscillations in metallic NPs corresponds typically to UV-Vis light and consequently, the SP arise absorption bands in this region of the spectrum as figure 8b illustrates. What makes the SP unique are the numbers of these processes. The absorbing efficiency of a particle is given by its absorption cross section. Classically it corresponds to the geometrical section of an ideal opaque particle absorbing the same number of photons than the studied particle.

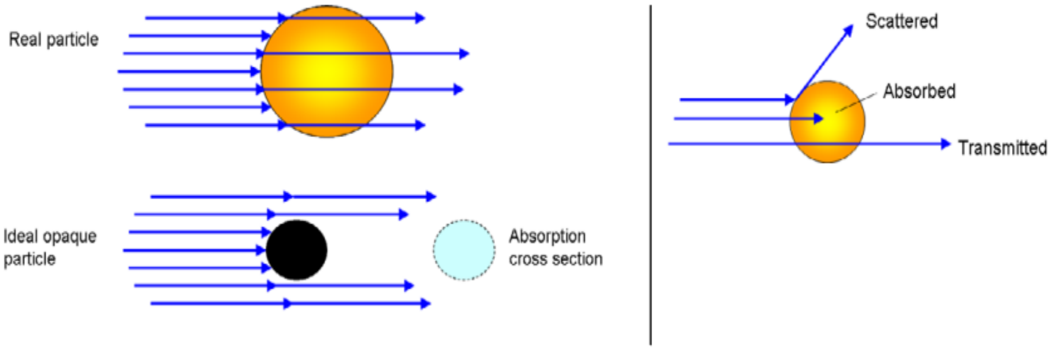

Figure 9: Scheme of absorption cross section (left). Concept of typical scattering absorption and transmission process(right)[66]

As figure 9 illustrates, it is possible to replace the absorbing NP by a perfect opaque one (absorbing any photon reaching its surface) that will absorb the same number of photons that our real particle. The section of this ideal particle represents the absorption cross section of the NP. For instance, if a NP absorbing half of the photons reaching its surface, the absorption cross section will be half of its geometrical section. Besides absorption, light interacting with matter can be scattered, changing the propagation direction and eventually also energy and moment. For this process, it can be also defining the scattering cross section as the geometrical section of an ideal scattering particle with the same scattering efficiency than the real particle.

The sum of absorption and scattering cross section is defined as the extinction cross section that represents the efficiency of the particle to remove photons from an incident beam. For perfect opaque particles the extinction cross section can be at maximum the particle section ($\pi \cdot r^2$). However, for few nm NPs, extinction cross sections larger to 10% of the geometrical section are scarcely found for other processes different to SP excitation[67,68]. In figure 10 is reported the resonant wavelength and the extinction cross section for 10 nm size metallic NPs, for noble metal NPs the extinction cross section can be up to 10 times their geometrical section; that is, the NP is capable of absorbing and scattering photon even away from its physical position. Somehow, the excitation of the SP is equivalent to concentrate the light passing by the NP to induce a huge extinction. A light beam propagating across a medium with metallic NPs decay in intensity as represented in equation 1:

$$I(x) = I_0 e^{-C\sigma x} (1)$$

being I_0 the initial intensity, C the concentration of NPs per unit volume, σ their extinction cross section and x the travelled distance. Indeed, a moderate increase in the extinction cross section can lead to a huge enhancement of light absorption.

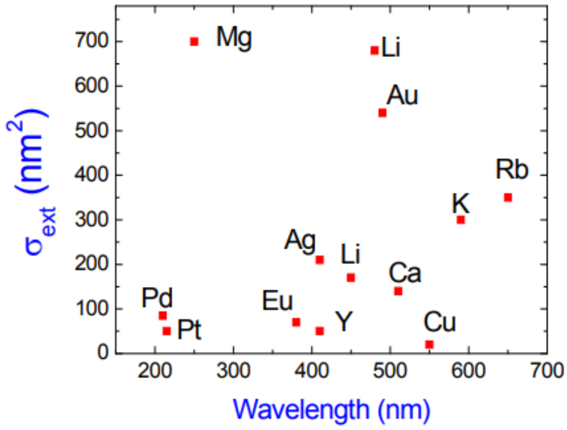

Figure10: Extincion cross section as a function of resonant wavelength[66]

1.2.2Surface plasmons and the Mie model

An accurate calculation of the SP and the associated light absorption requires solving the Maxwell equations at the NP region using the proper boundary conditions. The analytic solution can be obtained only for certain geometries, and it was developed by Gustav Mie in the early 1900[50,69]. The Mie theory provides an exact solution for spherical NPs assuming that they are non-interacting. In this case, Maxwell equations can be solved analytically, and the extinction cross section is given by the equation 2

$$\sigma_{ex} = \frac{2\pi}{|k^2|}\sum_{L=1}^{\infty}(2L+1)Re[a_L + b_L] \qquad 2$$

Where a_L and $b_L$can be written:

$$a_L = \frac{m\Psi_L(mx)\cdot\Psi'_L(x) - \Psi'_L(mx)\cdot\Psi_L(x)}{m\Psi_L(mx)\cdot\eta'_L(x) - \Psi'_L(mx)\cdot\eta_L(x)}\;;\quad b_L = \frac{\Psi_L(mx)\cdot\Psi'_L(x) - m\Psi'_L(mx)\cdot\Psi_L(x)}{\Psi_L(mx)\cdot\eta'_L(x) - m\Psi'_L(mx)\cdot\eta_L(x)}$$

Where k is the light wavevector in the dielectric medium, $x=|k|\cdot R$, R is the NP radius $m=n/nm$ being n and nm the refraction index of the metal (complex) and that of the surrounding dielectric medium respectively, and Ψ_L and η_L are the cylindrical Bessel-Ricatti functions.

There is a large list of theories that allow calculating the light absorption associated with SP for specific size ranges or when NPs are not spherical, or they are interacting. An excellent review of these theories is given in[50].

1.2.3 Dipole approximation

The dipolar approximation allows to consider the electric field inside the nanoparticles when the NPs diameter has value below 50 nm. With this approximation is possible to calculate light absorption of metallic NPs because NP size's is smaller than the light wavelength). SP resonance band falls at the visible part of the spectrum (~360-720 nm), the condition of small NPs is usually achieved for NPs diameter below ~50 nm.

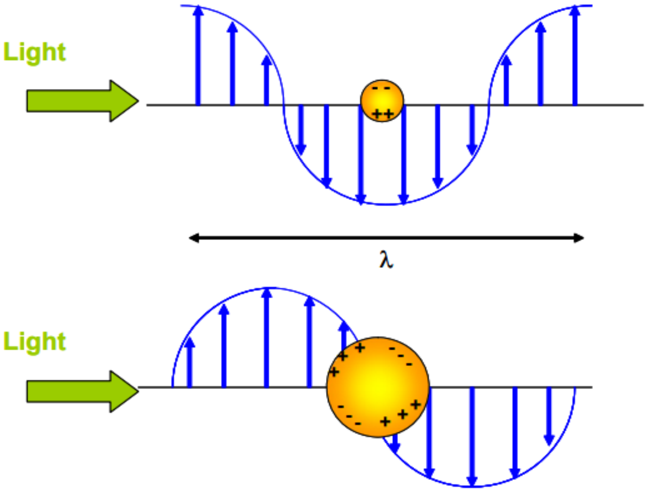

Figure 11: Electric field distribution for a small nanoparticle and for a nanoparticle which as comparable dimension with light's incident wavelength

Within this approximation, the absorption cross section is given by:

$$\sigma_{ext} = \frac{24\,\pi^2 R^3 \varepsilon_m^{3/2}}{\lambda}\frac{\varepsilon_2}{(\varepsilon_1+2\varepsilon_m)^2+\varepsilon_2^2} \qquad (3)$$

As the NPs size increases, the approximation is not valid anymore since the electric field inside the NP cannot be considered uniform.

1.2.4 Size and shape effects

SP resonance processes and consequently on the optical properties of the NPs strictly depends on particles size and shape. Considering only shape parameter it is necessary to distinguish between two regimes: one corresponding to small NPs (Mie theory and dipolar approximation are valid only in this regime) and large ones with size comparable to the wavelength.As said before the assumption that the NP described by a uniform dielectric dipole is valid. NP size affects the width and the intensity of the SP resonance band. By studying size effects in this range, it can be possible to distinguish intrinsic and extrinsic size effects. Damping of the electron oscillationscan fully describe the intrinsic effects. When SP are excited, the electrons are damped in their movement by the scattering with the ionic cores and with the surface.The damping constant for the electron oscillations reported in the equation (4) is given by:

$$\gamma = \gamma_0 + A\frac{V_F}{R} \quad (4)$$

(γ_0) describes the damping due the scattering of the oscillating electrons withthe ionic cores and this term is size independent, and is value is given by $\gamma_0 = V_F / l_\infty$, being V_F the velocity of the conduction electrons (Fermi velocity) and l_∞ the electron mean free path in the metal. This term depends just on the nature of the metal and the crystal structure.

A is a material dependent constant that considers the features of the surface scattering.

Figure 12 presents the optical absorption spectra of silver NPs embedded in silica (n=1.5) with different size. The resonance absorption intensity increases with particle size while the resonance peak slightly moves.

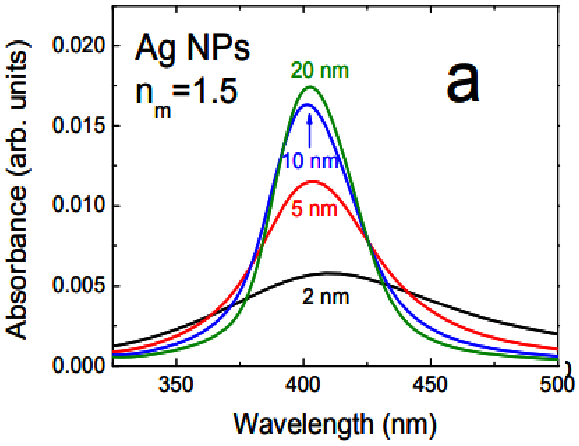

Figure 12: Optical absorption spectrum for different silver nanoparticles obtained with Mie theory

NPs with radius larger than 50 nm cannot be considered anymore much smaller than the light wavelength inside the metal. Thus, the particle is no more described by a dipole (figure 11) and further multipolar terms are required. Therefore, the resonance band splits into several peaks: two peaks for quadrupole, three peaks for an octupole, etc[70]. Figure 13 shows the contribution of the different terms in equation 2 to the extinction cross section of Au NPs. For Au NP with radius below 60 nm, the quadrupolar term (L=2) is negligible and the multipolar effects must be considered.

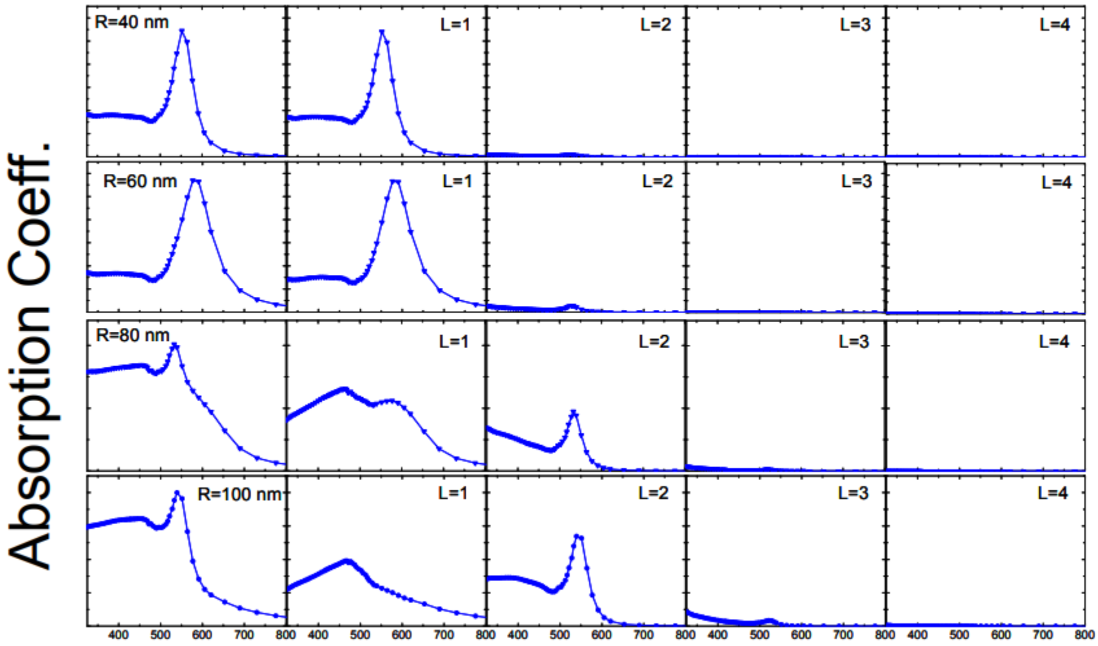

Figure 13: Optical absorption spectrum for Au NP with different size calculated according with Mietheory for n_m =1,5 and the contribution of multipolar terms[66]

If the NP size is further increased, NPs cannot be considered anymore as multipoles and the SP become propagating waves with well-defined modes or dispersion relations[51]. In the chapter 2 I will show experimentally size effect and the description of plasmon resonance band of anisotropic silver nanoparticles

1.2.5 The effect of the environment

SP does not depend only on the NPs morphological features, but it is also significantly modified by the surrounding medium as shown in the equation 3. Dielectric function of the surrounding medium determines the light wavelength at the vicinity of the NP electric field at the NPs surface is also altered. During SP excitation, the charge accumulation creates an electric field in the vicinity of the NPs. This field induces the polarization of the dielectric medium, resulting in a charge accumulation at the edges of the medium that will partially compensate the charge accumulation due to the conduction electrons movement. This reduction of charge depend on the dielectric function of the media; the larger is the dielectric function of the surrounding medium ε_m, the larger the polarization charge, and hence, the larger the effect on the SP. Thus, increasing the dielectric constant of the surrounding media will shift the SP resonant band toward larger wavelengths (i.e., smaller frequencies). Figure 14 shows the absorption spectra for anisotropic silver nanoparticle with 100 nm size in different media with different dielectric functions. The resonance intensity also increases with the dielectric function of the medium.

The effect of the surrounding medium will be one of the major topic of this thesis because it defines the ability of the metal nanoparticles to serve as materials for plasmon sensing

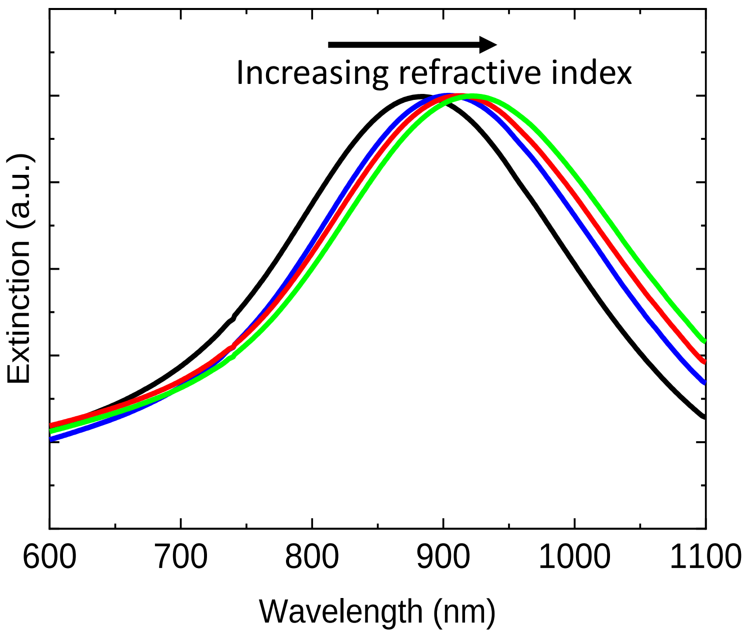

Figure 14: Optical absorption spectra of gold nanoparticles in different surrounding media having different refractive indices

Before to dive in the next part of the thesis it will be useful to know that in the chapters 2,3 and 4 are reported the AFM images in amplitude mode because it was easier to show the nanoparticles morphology, the relative section are acquired in tomography mode along with their scale bar.

Chapter 2: Synthesis by seed mediated growth and sensing features

The shape that has the lowest-energy ratio between volume and surface is the sphere, and in general a simple reduction metal salts leads to the formation of spherical nanoparticles. By controlling the experimental parameters such as concentration of the metal precursor, reducing agents, and stabilizers and reaction conditions such as temperature and time, it is possible to change the shape of the nanoparticles[71]. For these reasons, many different chemical and physical synthesis approaches have been proposed and investigated: seed-mediated synthesis, polyol synthesis, photochemical synthesis, electrochemical synthesis template-mediated synthesis, are just some of the most used. Among the chemical synthesis, seed-mediated growth results to be the best synthesis for the aims of this work, because it's a simple, rapid, low-cost method and as it is accessible with ubiquitous laboratory equipment and offers the possibility to prepare higher quantities of nanoparticles than with other methods.

Seed mediated growth is a wet chemical synthesis and it is constituted by two steps leading to the great advantage to split up the process of nucleation from the growth process. Dividing the whole synthesis in two well defined process leads to a better control of the shape and growing ratio of the final product of the synthesis. In the first step of synthesis a metal is reduced by a strong reducing agent, in the presence of stabilizing agent. The second step is related to the growth of the nanoparticles, by growing and shaping them, using different coordinating agents, mild reducing agents, and a precursor solution of the metal. The surfactant molecules will form suitable templates that facilitate the growth process to yield nanoparticles of desired morphology. This chapter is devoted to the synthesis of some silver nanoparticles in the colloidal state obtained by a Seed Mediated Growth (SMG) method. In the first part the SMG mechanisms will be discussed in the frame of the nucleation and growth theory. In the second part I will discuss some experimental findings based on the publication

Growth kinetics and sensing features of colloidal silver nanoplates[72]

together with some simulation performed in the frame of the so-called Discrete Dipole Approximation method (DDA). These results are correlated to the “in liquid” plasmonic properties of the produced particles and to their plasmon sensitivity.

2.1 The nucleation and growth phenomena

For the description of the formation of colloidal particles, it is convenient to introduce the concept of the "monomer unit" as the minimal building unit of a crystal of the particles. Monomers can either form crystal particles or dissolve back into the solution. The level of supersaturation, S, is defined as $[M]/[M_0]$, where $[M_0]$ is the equilibrium monomer concentration of the bulk solid. This concept greatly simplifies the theoretical description of colloidal solution synthesis by circumventing the difficulty of identifying the chemical properties of the solute. In the classical theory of nucleation, a nucleus is regarded as a sphere of a condensed phase and its free energy is defined by thermodynamic terms. [73,74] The free energy of a nucleus with radius r, is expressed in the following equation (1) as a

$$\Delta G = \frac{4}{3}\pi r^3 \Delta \bar{G} + 4\pi r^2 \sigma \quad (1)$$

where σ is the surface free energy per unit area and $\Delta\bar{G}$ is the free energy per unit volume of bulk crystal and is expressed as the difference between the free energy of the monomer in the crystal and in solution, and $\Delta\bar{G}$ strictly depends on the temperature as reported in the two following equations but to describe in a simple way it will be used the first equation 2.

$$\Delta\bar{G} = -\Delta T \cdot \Delta S_{Fus} \text{ (2) or}$$

$$\Delta\bar{G} = -\frac{RT\ln(S)}{V_m}$$

Where ΔT in the equation 2 is the difference between melting point temperature and undercooling temperature (T-T$_f$) and ΔS_{Fus} of the function entropy is:

$$\Delta S_{Fus} = \frac{\Delta Q_{Rev}}{T_f} \quad (3)$$

Inserting equation 3 into equation 2 led to equation 4

$$\Delta\bar{G} = -(T - T_f)\frac{\Delta H_{Fus}}{T_{Fus}} \quad (4)$$

Equation 4 is the difference between the free energy of the monomer in the crystal and in solution. By substituting equation 4 in the equation 1 it will be obtained the fully explained relation between temperature and free nucleation energy equation (5)

$$\Delta G = \frac{4}{3}\pi r^3 \Delta\bar{H}_{Fus}\frac{T - T_f}{T_f} + 4\pi r^2 \sigma \quad (5)$$

During crystallization process T is always lower than T_f , to put this concept in more strictly direct terms the first term of the nucleation energy is always negative and depends on temperature, instead the surface energy term $4\pi r^2\sigma$ not depends on the temperature. Bulk terms present in the upper equation became more negative by increasing undercooling temperature, in the figure 1 is shown the whole nucleation free energy

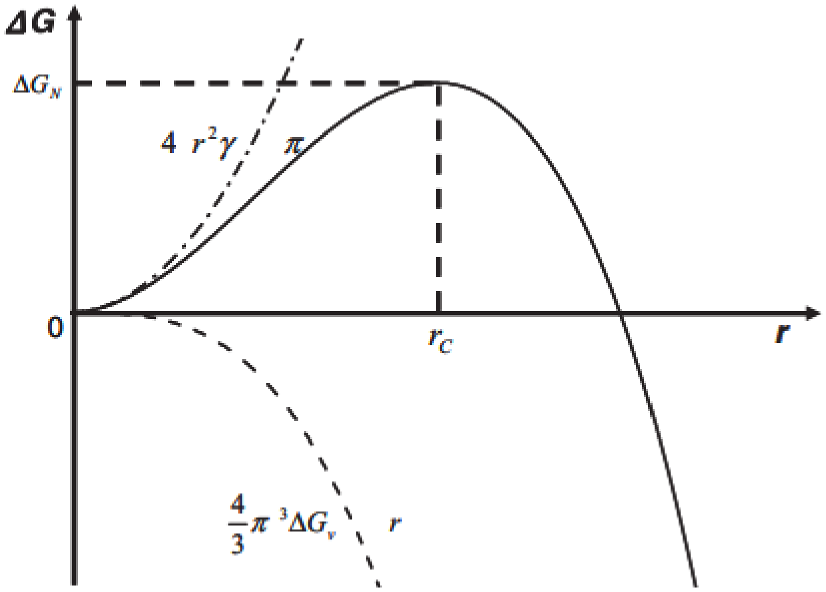

Figure(1): Plot for the crystallization free energy vs particle radius

Here in Equation 6, V_M is the molar volume of the monomer in crystal. In Figure 1, ΔG of nucleation is plotted with its two components, namely, the surface and volume terms. As shown in the figure, the volume term favours the formation of crystals if $S > 1$, to relieve the excess free energy of the monomers in the supersaturated solution. However, the surface term imposes an extra free energy requirement for the formation of nuclei. As a result, nuclei smaller than a critical radius, r_c, cannot grow further, but only dissolve back into the solution as the monomers, because this is the only way for them to decrease their free energy. In other words, the critical radius is the minimum size of nuclei that can resist dissolution and grow further. The value of r_c can be found from the relation dΔG/dr = 0 at r = r_c

$$r_c = \frac{2\sigma V_m}{RTlnS} \quad (6)$$

The reaction rate for the formation of nuclei can be written in the Arrhenius form and the formation energy of nuclei, ΔG_N, is equal to ΔG (rc). Then, wehave in the equation 7

$$\frac{dN}{dt} = A \exp\left(-\frac{16\pi\sigma^3 V_M^2}{3k_b^3 T^3 N_A^2 (lnS)^2}\right) \quad (7)$$

where N, A, kB, NA and T are the number of nuclei, the preexponential factor, the Boltzmann constant, Avogadro's number, and temperature, respectively. Due to the energy barrier, ΔG_N, the supersaturation level for homogeneous nucleation is generally far higher than that for the growth of colloidal particles. The presence of an energy barrier for homogeneous nucleation is very important for the control of the size distribution in the colloidal synthesis of nanocrystals. The classical nucleation model has some apparent problems. Equation 7 contains the surface free energy (σ) and monomer molar volume (Vm) terms, which are defined for a bulk solid. In Equation 7, there are three experimentally controllable parameters: the level of supersaturation, temperature, and surface free energy. The nucleation rate can be adjusted by changing the surface free energy. In the synthesis, modifying the nature and concentration of the surfactant in the solution can change the surface free energy to control the nucleation rate.To fully comprehend the growth step that occurring during seed mediated growth process it is wise to introduce the concept of heterogeneous nucleation and diffusion. In the two-stage process, monomers first nucleate to form something like a dense, metastable liquid, which then overcomes an additional energy barrier to initiate crystallization and growth. Even though the two-stage mechanism has been recognized for a variety of materials, it is yet to be extended to the synthesis of metal nanocrystals. One of the major challenges is that the transition from metal precursor to nucleus continues to evade our understanding, while remaining difficult to control. As a means to avoid the enigmatic process of homogeneous nucleation, monomers or even the precursors can be added to preformed nanocrystals (the so-called seeds) at a concentration below supersaturation. During this process, monomers undergo phase transformation directly on the surface of a seed, a route known as heterogeneous nucleation. Modelling this process requires two additional surface energy contributions: the substrate–medium surface energy ($\gamma_{\alpha m}$) and the nucleus–substrate surface energy ($\gamma_{\alpha\beta}$). As shown in Figure, a nucleus in equilibrium with a surface forms a contact angle q according to a relationship defined by the Young equation (8) . From this equation, we can obtain the barrier to heterogeneous nucleation (ΔG^*_{hetero}) as a function of the contact angle θ and (ΔG^*_{homo}) as shown in eq (9) .

$$\cos\theta = \left(\frac{\gamma_{\beta m} - \gamma_{\alpha\beta}}{\gamma_{\alpha m}}\right) \qquad 8$$

$$\Delta G^*_{\text{hetero}} = \left(\frac{2 - 3\cos\theta + \cos^3\theta}{4}\right)\Delta G^*_{\text{homo}} \qquad 9$$

Equation (9) indicates that the barrier to heterogeneous nucleation cannot physically surpass the barrier to homogeneous nucleation since the q-dependent term in the parenthesis is bounded by 0 and 1. For a special case, where the nucleus has a hemispherical morphology and q = 90°, the energy barrier to heterogeneous nucleation is exactly half of what is required for homogeneous nucleation, which implies that, in the same reaction system, less driving force (i.e. requiring a lower concentration of monomers or a lower reaction temperature) is needed for heterogeneous than for homogeneous nucleation (Figure 4 b). As a preventative measure, supersaturation can be treated as the upper limit to protect against the formation of additional seeds from homogeneous nucleation during seed-mediated growth.

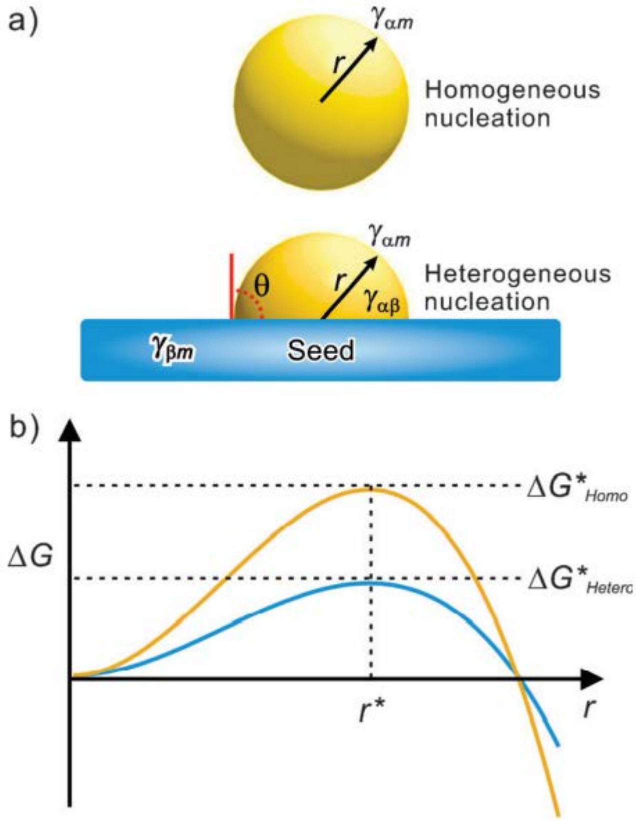

Figure 2: Homogeneous and heterogeneous nucleation comparation between their nucleation mode and variation of their Gibbs free energy as a function of size

The growth of spherical crystal particles in the solution occurs via two steps, as shown in Figure 3. The first is the transport of the monomers from the bulk solution onto the crystal surface and the second is the reaction of the monomers on the surface. The description of the first process begins with Fick's law of diffusion,

$$J = -D\frac{d[M]}{dx} \quad (10)$$

where J and D, are, the monomer flux and the diffusion constant, respectively. The concentration gradient around the surface of a spherical nanocrystal particle is shown in Figure 3, along with a schematic of the diffusion layer structure.

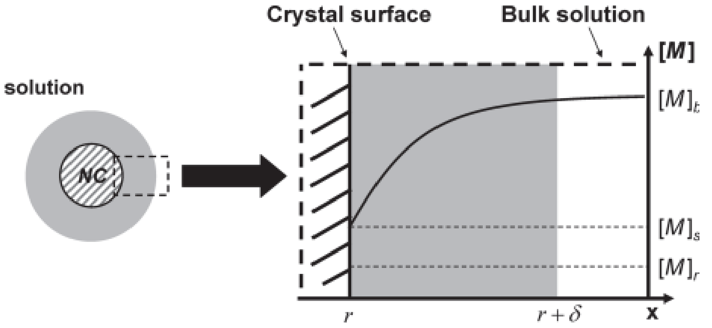

Figure3: Diffusion layer structure near the surface of a nanocrystal[19]

Let x be the radial distance from the center of the particle. The monomer concentration is $[M]_s$ at the surface of the crystal (x = r). At a certain point far enough from the particle ($x=r + \delta$), the concentration reaches $[M]_b$, the bulk concentration of the solution. From Equation 10, the total flux of the monomer J onto the surface of the particle can be calculated as

$$J = 4\pi\, Dr([M]_b - [M]_s)\ (11)$$

Because of the mass balance, J is equal to the monomer consumption rate by the surface reaction of the particle. The monomer consumption (equation 12) rate by the growth of the particle can be written as

$$J = 4\pi r^2 k([M]_s - [M]_r)\ (12)$$

where k is the reaction constant and $[M]_r$ is the solubility of the spherical particle of radius r. [71,75,76] This equation assumes that the reaction constant k is independent of the particle size because it depends on the local point where the monomer and the surface of the particle make contact. The larger particles have the lower solubility due to Gibbs–Thomson effect, as mentioned below and grow faster than the smaller ones. There is a relationship between the monomer consumption rate and the rate of the particle volume change as

$$J = \frac{4\pi r^2}{V_m} \cdot \frac{d_r}{d_t}\ (13)$$

From Equations 11 and 12, an expression for [M] s is obtained that

$$[M]_s = \frac{D[M]_b + k[M]_r}{D + kr}\ (14)$$

By inserting this equation into Equation 12 and using Equation 14, it will be obtained the expression for the growth rate as[76]

$$\frac{dr}{dt} = \frac{DV_m([M]_b - [M]_r}{r - D/k} \quad (15)$$

In the nanometer scale, the solubility of a particle is extremely sensitive to its radius. According to the Gibbs–Thomson relation, a spherical particle with radius r has extra chemical potential, $\Delta\mu$, equal to $2\gamma V_m/r$. Then $[M]_r$ can be expressed as a function of r as

$$[M]_r = [M]_\circ \exp\left(\frac{2\gamma V_m}{r RT}\right) \qquad 16$$

By inserting this expression into Equation 15, we have a general growth rate equation for a spherical particle as follow[76,77]

$$\frac{dr^*}{d\tau} = \frac{S - \exp(1/r^*)}{r^* + K} \qquad 17$$

wherein three dimensionless variables are defined as follows.[78,79]

$$r^* = \frac{RT}{2\gamma V_m} r \qquad 18$$

$$\tau = \frac{R^2 T^2 D[M]_\circ}{4\gamma^2 V_m} t \qquad 19$$

$$K = \frac{RT}{2\gamma V_m} \frac{D}{k} \qquad 20$$

In Equations 18,19,20, 2 γVm/RT and K are called the capillary length and Damköhler number (Da), respectively. The capillary length is a measure of the size effect on the chemical potential of a particle. Damköhler number indicates whether the diffusion rate (D) or reaction rate (k) dominates the growth reaction.[78] The growth rate equation derived above provides a general basis for the description of the growth process. As shown in Figure 8, the growth of a particle is largely affected by its size.

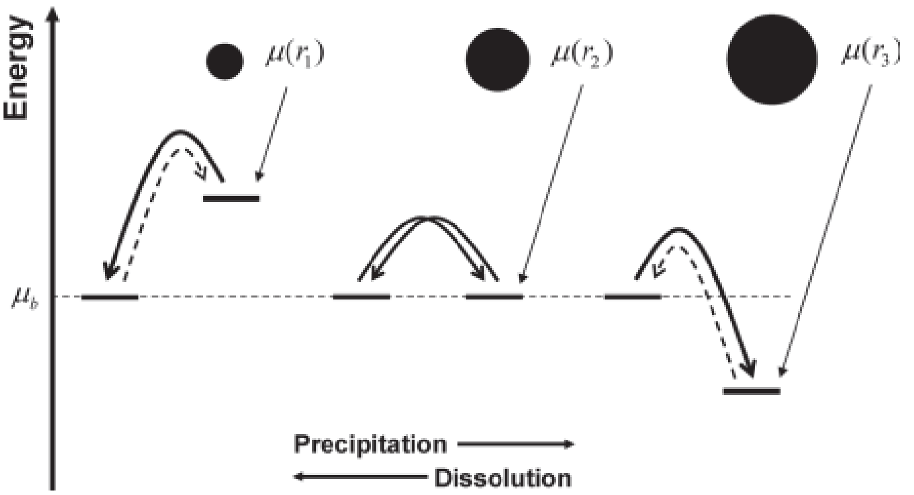

Figure 4: Schematics of chemical potential versus reaction coordinate for particles of different size[19]

When the particle is so small that the chemical potential of its monomers is lower than that of the monomers in the solution, the dissolution reaction is favoured. In other words, the distribution in the solubility of the particles provides the driving force for Ostwald ripening. The effects of Ostwald ripening on the size distribution of nanocrystals and on the larger particles are quite different. As shown in Equation 16, the solubility of the nanocrystals is extremely sensitive to their size, which strongly motivates Ostwald ripening. In the ripening process, the larger particles grow faster than the smaller ones, opposite to the focusing effect. As a result, Ostwald ripening 'defocuses' the size distribution of the monodisperse nanocrystals. If the size distribution is initially quite broad, the size uniformity can be improved to a certain degree via Ostwald ripening(see reference 80) as the smaller particles dissolve away. For the particles whose size is far larger than the capillary length, the solubility of the particles in Equation 16 can be approximated as

$$[M]_r = [M]_\circ \left(1 + \frac{2\gamma V_m}{r RT}\right) \quad 21$$

Under these conditions the effect of Ostwald ripening is not as extensive as for the nanocrystals, and the size distribution of the particle's changes little in terms of the relative standard deviation during the ripening process[78].The mean size of the particles and the value of σ_r slowly increase during Ostwald ripening. The size distribution of the particles turns into a stationary state in the later period of Ostwald ripening and the mean size in this state mainly depends on the surface free energy[76–80].

2.2 Experimental methods

Silver nitrate ($AgNO_3$, 99.9%), tri-sodium citrate (TSC, 99%), sodium borohydride ($NaBH_4$, 99%), and hydrated hydrazine (50–60%) have been purchased from Sigma-Aldrich and used as received without further treatment. Deionized water (>18.4 MΩ·cm) was used in all of the synthesis processes. Silver seed solution is obtained by reducing a silver nitrate solution by using sodium borohydride ($E_0 = -0.78$ V), in the presence of TSC as a stabilizing agent. In particular, we added 0.5mL of a 20mM $NaBH_4$ solution to 10mL of a 59mM $AgNO_3$ one, in the presence of TSC (1 mL, 35 mM). The reaction is conducted at 293 ± 1K under strong stirring. The as-prepared colloid was then aged for 24 hours before use to ensure a complete reduction of $AgNO_3$. Defined aliquots of colloidal seeds, ranging from 20 µL to 1mL (±1 µL), are mixed with a freshly prepared 20mL solution of hydrated hydrazine ($N_2H_4 \cdot 2H_2O$) and TSC. Each of these former colloids is a reactor (solution A) for the growth of specific silver nanoplates. From here on, a 59mM solution of $AgNO_3$ (solution B) is added dropwise to solution A, by varying the addition rate from 0.1 mL/min to 10 mL/min.The addition rate has been controlled by using a peristaltic pump with an error below 0.01 mL/min. All the experiments have been performed at 293 ± 1K in a thermostatically controlled room. The obtained colloidal dispersions have colors which change from yellow to orange, pink, red, green, and finally to blue (Figure7), according to the shape and size of the nanoplates (from here on Ag NPTs). The blue color corresponds to the biggest Ag NPTs.

Figure 7: Various silver nanoparticles at different plasmon resonance

It was seen that during the growth process is used as capping agent the trisodium citrate, indeed his role is fundamental to obtain the plate like nanostructure. Ag seeds with a spherical shape can be directed to grow into nanocrystals enclosed by {111} or {100} facets by introducing citrate ions

(CA) or poly(vinylpyrrolidone) (PVP) as the capping agent[77].Citrate ions and PVP can bind selectively to {111} and {100} facets of Ag, respectively, their capability to bind different crystalline deeply influence the shape of the final product figure 8.

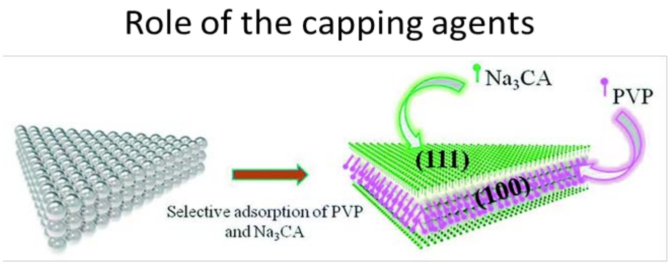

Figure 8: Interaction for PVP and CA with the silver's crystalline structure

Indeed, due to this behaviour silver nanoplates are very interesting model system for investigating the roles of defects and capping agents in controlling the evolution of shape or morphology. Both top and bottom surfaces of Ag are covered by {111} facets and contain twin planes and stacking faults on the side faces along the vertical direction[81]. Ag nanoplates would undergo lateral growth along the twin defects and stacking faults to produce larger thin plates. Vertical growth that can significantly increase the thickness of Ag nanoplates has not been reported to date. Even for lateral growth, this process tended to cease at a certain point, so only thin Ag plates with edge lengths below 1 nm can be generated. The nanoplate had a triangular cross-section along the direction perpendicular to the large, flat faces, with some slight truncation at the corners. The nanoplate is enclosed by two {111} planes as the top and bottom faces, and by round planes as the side faces. This result indicates that, in the presence of citrate ions, the newly formed Ag atoms were preferentially deposited on the side faces of an Ag nanoplate instead of the top and bottom faces covered by {111} facets, thus, demonstrating the feasibility of this approach for confining the growth of a nanoplate seed to the lateral directions. In both cases, the {111} facets are expected to grow more slowly than other facets such as {100} during a seed mediated growth process when sodium citrate is present. Consequently, although {111} planes also exist on the side faces of a nanoplate, Ag deposition could still occur at these sites to facilitate lateral growth.

2.3 Size control and plasmonic features

Now let's have a look to the extinction properties of the various obtained colloids. Fig 9 reports a comparison between a colloid of spherical particles and one of nanoplates. Besides interband transition signals located below 300 nm, the resonance spectra of spherical nanoparticles and those of platelets deeply differ (see fig9).

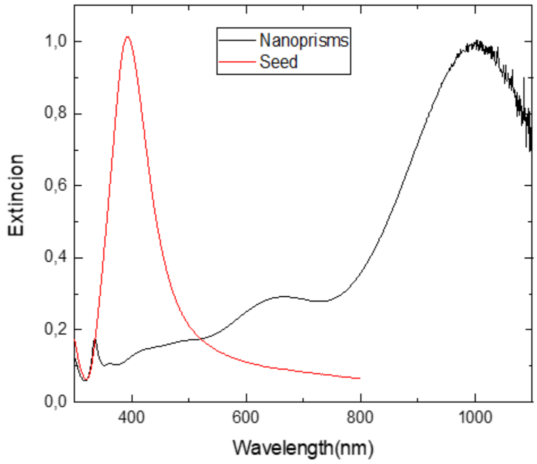

Figure 9: Typical extinction spectra of spherical silver nanoparticles (red) and silver nanoplates (black).

The former has single sharp resonances at around 395nm (red line) while the latter presents many plasmon modes which are generally attributed to the following:

(a) Longitudinal in-plane dipole mode at 600nm

(b) Longitudinal quadrupole and transverse dipole modes at 400nm

(c) Transverse out-of-plane quadrupole mode, which is characteristic of flat particles at 334nm

The addition rate of $AgNO_3$ (solution B) to the nutrient one (solution A) represents an important parameter to trigger silver nanoplate morphology since the growth reaction kinetics is driven by the instantaneous concentration of reactants in solution. It has been well established[82] that in a seed-mediated growth at least two possible mechanisms are possible. In one mechanism, the surfactants form a template with a certain size. This size is dependent on the surfactant concentration and the ionic strength of the solution. When a seed is introduced into the growing solution, the surfactant-capped seed becomes part of the soft template, and the growth starts by diffusing the silver atoms into the template. It is also possible that the surfactant-capped seed starts growing and as the new atoms join the nanocrystal lattice, they are protected by the surfactant monomers coming from the solution. In any case, there is a specific competition between Ostwald ripening and secondary nucleation events[83] if $AgNO_3$ is added step by step, the instantaneous concentration of Ag^+ ions will always be lower than that of reducing ($NaBH_4$) and complexing agents (TSC): Ag^+ reduction rate will certainly depend on the concentration of species as well as on the ability of citrate to complex Ag^+ ions slowing down their reduction. If the above-mentioned solutions are mixed at a specific addition rate, seed concentration will determine the nanoplate size and their aspect ratio. As an example, Figure 10a reports the evolution of the extinction spectra and the corresponding particle morphologies as a function of the nutrient addition rate between 6 mL/min and 0.3 mL/min. Here, we have chosen the reactor with 80 µL of initial seed colloid dispersed into 20 mL TSC and hydrazine solution. We expect a secondary nucleation which produces mostly spherical nanoparticles at high addiction rates because at high rates this process is faster than Ostwald ripening process. Indeed, at addition rates above 1.5 mL/min, the overall plasmon spectrum retains a signal at 400 nm, as expected for the presence of spherical nanoparticles. Meanwhile, the competing Ostwald ripening mechanism contributes with the characteristic in-plane dipole mode, which is red shifted during the growth of the platelets. It is important to note that the signal at 400 nm is slightly shifted with respect to that obtained for the primitive seed colloid. This is certainly due to the size difference between the seeds (below 20 nm) and the spherical nanoparticles grown by secondary nucleation, in which sizes can be appreciated in Figure 10(b). TEM data reported in Figure 10(b) give an idea of the situation, once the $AgNO_3$ nutrient solution addition rate is increased. Initially (high addition rates), the plates are quite small and the presence of spherical nuclei is evident. As the addition rate decreases, the signal at 400 nm is reduced in intensity and the longitudinal in-plane dipole mode moves towards the infrared and increases in intensity because of the plate breadth modification. In Figure 9, we present the evolution of the longitudinal dipole mode position (localized surface plasmon resonance wavelength, λ_{LSPR}) which is related to the growing silver platelets, as a function of the nutrient solution addition time. The plot regards three different reactors (solution A) with three different concentrations of seeds. For all of them, the data show a classical saturation behavior, which can be well presented by the empirical relation (equation 22):

$$\lambda_{\mathrm{LSPR}} = \lambda_{\mathrm{sat}} + (\lambda_{\mathrm{sat}} - \lambda_0)e^{-kt}. \qquad 22$$

We identify a saturation value λ_{sat}, a kinetic constant k, and the parameter λ_0 which represents the plasmon wavelength position at $t = 0$ λ_{sat} gives the final position of the longitudinal dipole mode once the growth is finished. Saturation changes significantly by changing the seed concentration and reaches values above 1000 nm in the case of very diluted reactor colloids (below 80 μL). The kinetic constant k indicates how fast the growing process is. Of course, the smallest the breadth of the final particles is, the faster is the growing process, as can be seen in Table 1, where we report the fitting results obtained using equation (22).The empirical relation in equation (22) clearly originates from a first-order kinetics. Xia et al[84] have recently proposed the use of such a law in seed-mediated growth of colloidal metal nanocrystals. They considered that in all those cases in which the reductant is supplied in excess and the types of reagents and temperature involved are fixed, the reductant concentration remains relatively constant throughout the synthesis and so the instantaneous precursor concentration at time t can be modelled using pseudo-first-order law. These data reflect some features of the growing mechanism. On the other hand, it is to be considered that a seed mediated growth (heterogeneous nucleation) is always in competition with a homogeneous nucleation procedure.

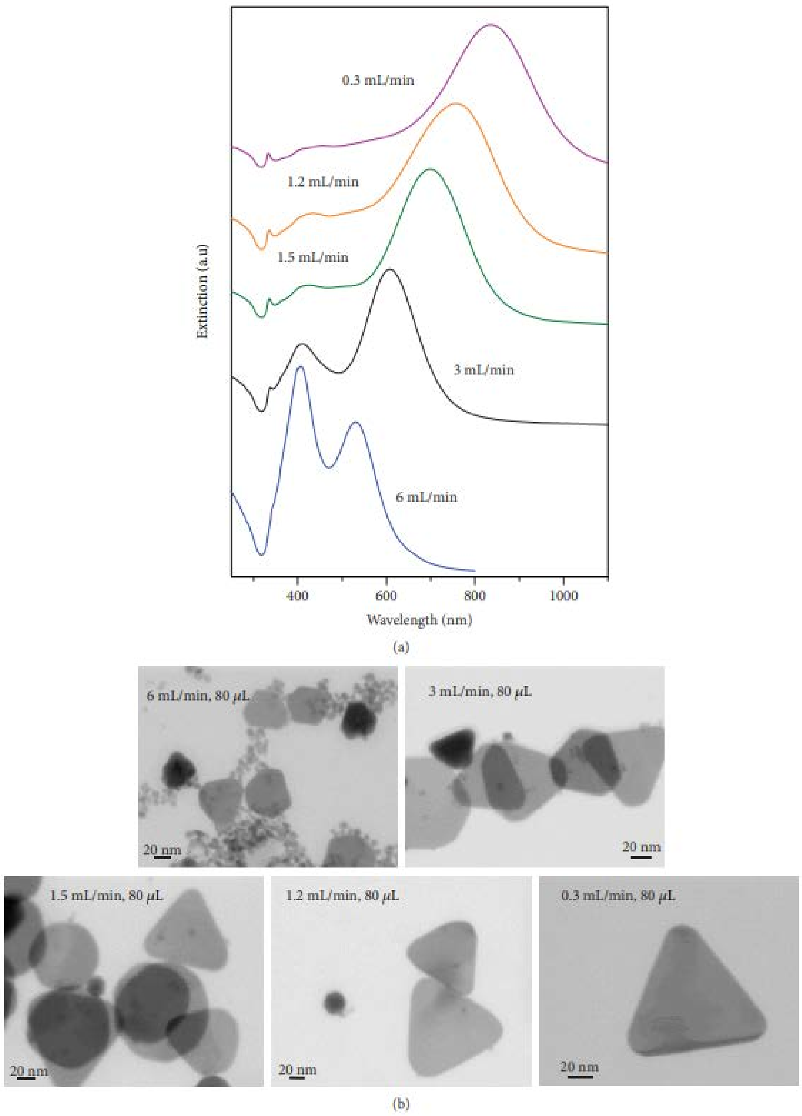

Figure 10:(a) *Plasmon signals for several platelet colloids, each obtained by changing the nutrient solution addition rate. (b) Some TEM images showing the geometric features of the silver nanoparticles obtained after different addition rates.*

However, if we maintain the growing driving force sufficiently low, homogeneous nucleation can be prevented and heterogeneous nucleation prevalently occurs.

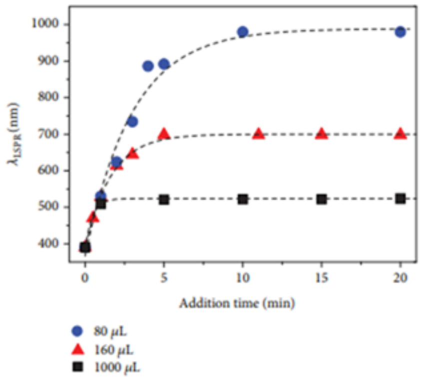

	80 μL	160 μL	350 μL	1000 μL
λ_{sat}	989	700	615	524
λ_0	388	367	389	390
k (min^{-1})	0.33	0.63	1.07	2.2

Figure 11: Evolution of the longitudinal dipole mode position as a function of addition of the nutrient solution time with three different seed concentrations, in the table are shown the parameters obtained as a results of the fit generated bu the equation 22. Image taken from ref[2]

This is the core of our experiment where the different batches are characterized by the number of available seeds, ready to act at the same precursor conditions. For this reason, the different kinetic constants are due to a more favourable (and then faster) environment during the growth as the initial concentration of seeds increases. The already-mentioned differences in the saturation values indicate that the lower the seed concentration is, the greater is the average aspect ratio of the platelets grown (higher λ_{LSPR}) since the available (constant) Ag^+ ions in solution are forced to feed a lower quantity of nuclei. Of course, the time constants reflect this feeding process with values that follow a consistent trend. Figure 12 reports the extinction spectra obtained for different seed aliquots in saturation conditions (Figure 11(a)) and the relative AFM observation once each colloid is suitably deposited onto a flat surface (Figure 12(b).

The spectral differences correspond to an increase of the aspect ratio from 3 (1000 µL) to 20 (20 µL). The plasmon resonance of the latter extends deeply into the near-infrared region. Figure 12(b) also shows a fluctuation of the plate heights from 12 to 20 nm. This has no relevant effect on the aspect ratio since the size of the plate basal plane is at least one order of magnitude larger than the height. We ascribe the observed fluctuation to a moderate distribution of the seed size, whose diameters should be in the range 10–20 nm, as the plasmon resonance is given at 395 nm[85].

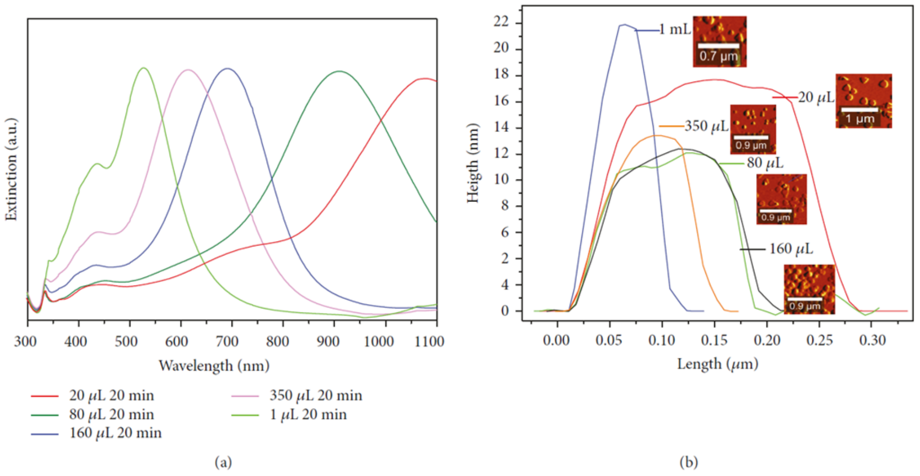

Figure 12: (a) Plasmon resonances in a saturation condition (very low addition rates) for several reactors, each with a different initial seed concentration. (b) The AFM profile for some of the platelets obtained.

2.4 "In liquid" Plasmon Sensitivity

The plasmon sensitivity quantifies the dependence of the plasmon resonance wavelength or frequency on changes in the dielectric properties of the surrounding medium. Nano plasmonic refractometric sensing enables the detection of small refractive index (RI) changes in the dielectric medium surrounding the metal nanostructure[86,87]. This happens through the changes of either the plasmon peak position or the intensity per refractive index units (RIU). In this work, we have defined a refractive index sensitivity[88] S as follows:

$$S = \frac{d\lambda_{\mathrm{LSPR}}}{dn} = \frac{d\epsilon'_{\mathrm{LSPR}}/dn}{d\epsilon'(\lambda)/d\lambda}, \qquad 23$$

where n is the refractive index of the host matrix, λ_{LSPR} is the wavelength at the maximum plasmon resonance (in-plane dipole, in our case), and ϵ' is the real part of the dielectric function of the metal constituting the nanoparticle. These measurements are generally performed by monitoring the spectral changes that occur when the plasmonic material is exposed to solutions with various well-known RIs. Literature data[89] largely report the RI sensitivity as highly dependent on the nature of the plasmonic nanoparticles (i.e., size, shape, and metal composition), so we expect to find a variety of different efficiencies in our class of silver nanoplates. So, for the silver nanoplates produced by chemical reduction method and light driven synthesis method we have tested their plasmon sensitivity properties and reported their respective results. We have tested the sensitivity of both type of particles by controlling the surrounding refractive index with sucrose solutions prepared at different concentrations. Indeed, sucrose molecules do not interact chemically with the nanoparticles, and, at the same time, the correlation between the solution refractive index and its sucrose concentration is well established in the range between 1.333 (pure water) and 1.46 (70% w/w).For the chemical silver nanoplates in Figure 13(a) are reported some results after an investigation of the dipole plasmon sensitivity for some of the colloidal nanoplates under study. We have limited our study to different initial seed concentrations after a sufficiently slow $AgNO_3$ addition (saturation conditions). In the figure, $\Delta\lambda_{max}$ is the difference between the in-plane dipole plasmon resonance position of the nanoparticles at a given sucrose concentration (and then at a given refractive index) and that found in pure water. At first glance, it seems that the higher the platelet aspect ratio is (ratio between the breadth and the thickness of the particle), the better is the observed dipole plasmon resonance sensitivity. Indeed, it reaches $\Delta\lambda/\Delta n$ = 450 nm/RIU for the particles prepared using 20 μL of seed solution. Some authors have observed that this trend is misleading and that the sensitivity changes are merely due to a variation of the spectral position of the plasmon resonance. In particular, Saison-Francioso et al.[90] determined an analytical expression of S in the quasistatic approximation. They found that $\Delta\lambda_{LSPR}/\Delta n$ is related to the LSPR wavelength position, the refractive index of the host matrix, and the wavelength dispersion of the real part of the dielectric function on the nanoparticles. Under the hypothesis of a quadratic dependence of ϵ' λ as[88]

$$\epsilon'(\lambda) = A\lambda^2 + B\lambda + C, \qquad 24$$

the final expression for S is given by

$$S = \frac{2\left(A\lambda_{\mathrm{LSPR}}^2 + B\lambda_{\mathrm{LSPR}} + C\right)}{n(2A\lambda_{\mathrm{LSPR}} + B)}. \qquad 25$$

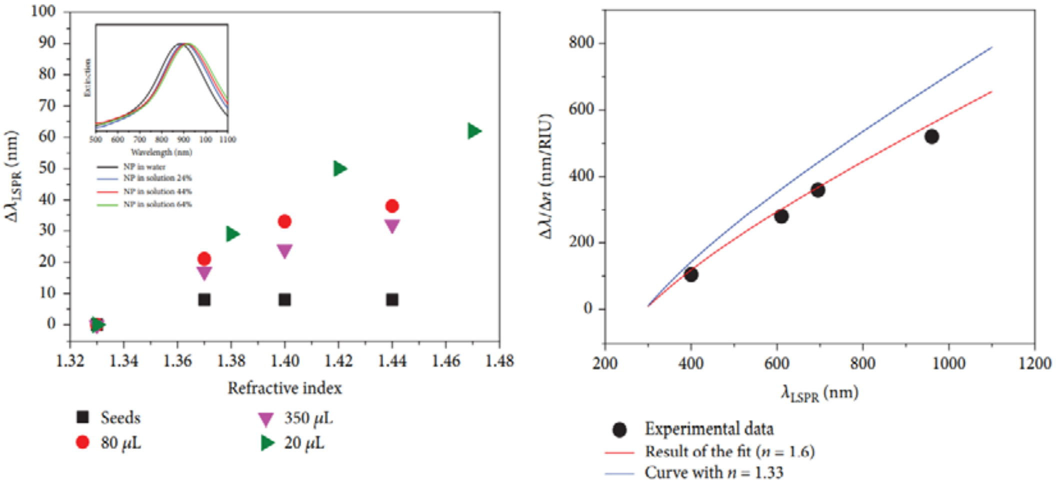

Figure13: (a) Results after an investigation of the dipole plasmon sensitivity for some of the colloidal nanoplates under study. (b) Sensitivity as a function of the plasmon resonance position.

This simple correlation has been tested theoretically by comparing the analytical expression (equation (25)) with numerical simulations performed by using the well-known finite difference time domain (FDTD) method which has been used to simulate each single-plasmon resonance[91]. We want now to test such a theory with the colloidal samples previously described. We have first obtained the parameters A, B, and C by fitting ϵ′ λ using equation (3) in the wavelength interval of interest (300–1500 nm)[92](Figure 14).

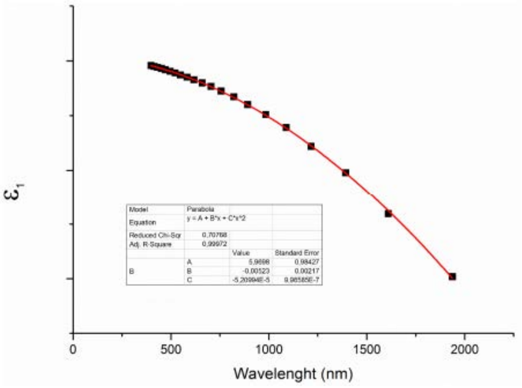

Figure 14: Fit of ϵ′(λ) using Equation 2 in the wavelength interval of interest (300-2000 nm)

and have been obtained using the optical constants taken by ref. [89]. Once these parameters have been calculated, they are used to perform a final fitting procedure, using equation (24) as reported in Figure 13(b). The red curve represents a fitting with the method presented in ref.[87]. The hypothesis of Saison-Francioso et al. is respected, and a surrounding medium refractive index value of n = 1.6 is obtained by the fit. The value is not so far from the refractive index of water (1.33). Figure 13(b) also reports the behaviour of the same curve at n = 1.33. We can ascribe this discrepancy to two different reasons:

(a) A deviation from the quasistatic approximation which is evident at high λLSPR

(b) Due to reaction by-products, the effective refractive index of the liquid surrounding the particle deviates from that of pure water. Further investigation is underway to clarify this point.

2.5 Plasmon resonance simulations

The nanoplates are first obtained with controlled shapes, as colloid, by a proper seed-mediated growth procedure and then paved on the cuvette inner surfaces. The results of in liquid sensing measurement are interpreted with the Boundary Element Method (BEM) calculations [93,94] that give support to the experimental results. Before to comment our results, it is necessary to spend some words about BEM. BEM has emerged as a powerful numerical technique for solving a wide variety of computational engineering and science problems. The method has remote deep roots in the history of mechanics and its mathematical foundations include the theorems of Gauss, Green and Stokes – they allow the basic reduction from volume differential equations to boundary integral equations and to do this, one approximates the surface charge as a discrete number of points located at the centroids of small surface elements

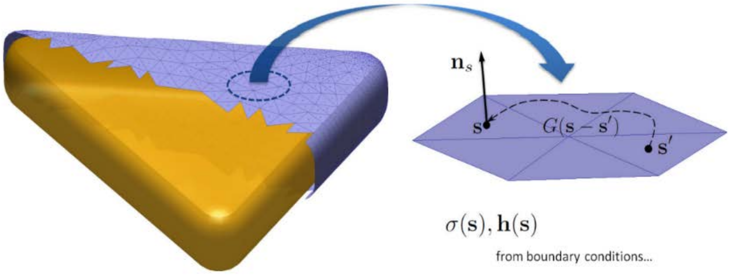

Figure 15:After discretizing the particle surface the corresponding continuous surface charges and currents are approximated as points in the centroids of the small surface elements. The Green function connects these different points with each other(picture taken from ref[95]).

By discretizing the particle's surface with BEM see fig 15 it is possible to determine the electromagnetic fields (shown in the figure below) and simply compute the scattering, absorption, and extinction cross sections from the Poynting vector (in the equation shown below).

$$
\begin{aligned}
C_{\text{sca}} &= n_b \oint\limits_{\partial\Omega} \Re\mathrm{e}\left\{\hat{\boldsymbol{n}}\left(\boldsymbol{E}\times\boldsymbol{B}^*\right)\right\}\, da, \\
C_{\text{ext}} &= -\frac{1}{n_b} \oint\limits_{\partial\Omega} \Re\mathrm{e}\left\{\hat{\boldsymbol{n}}\left(\boldsymbol{E}\times\boldsymbol{B}^*_{\text{inc}} + \boldsymbol{E}^*_{\text{inc}}\times\boldsymbol{B}\right)\right\}\, da, \\
C_{\text{abs}} &= C_{\text{ext}} - C_{\text{sca}}.
\end{aligned}
$$

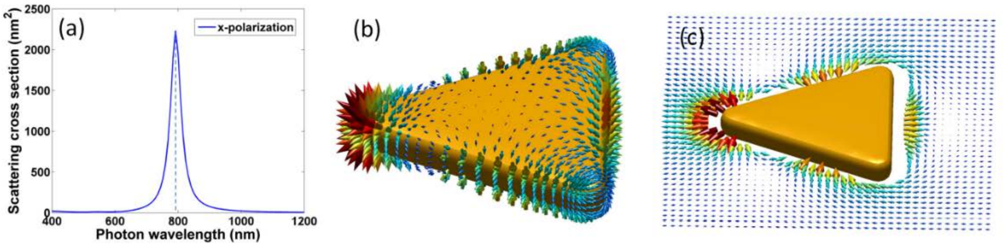

Figure 16(a): Scattering cross section of a gold nanotriangle. Figure (b) and (c): it is reported the electromagnetic field inside (b) and outside of the nanoparticle[95]

So we have compared the results of plasmon sensitivity of experimentally obtained nanoparticles with their simulated (BEM) counterpart. As said before to obtain the sensitivity results of our silver nanoparticles after the growth in water (n = 1.33), the surrounding refractive index of the plates in suspension, has been varied up to 1.42, by adding different aliquots of a sucrose solution. DRS values of 342 nm/ RIU (refractive index units) and 457 nm/RIU are found for the 600 nm and 800 nm colloids, respectively. The results are shown in Fig17. as full dots. These values agree with those reported in literature, even higher in the case of 800. Differently shaped noble metal NPs (spherical, cubic, pyramidal) has also been also studied by H.Chen et al., with results in the range between 44 and 390 nm/RIU[96]. The same colloidal system it was replicated with BEM measurements and the simulated data are perfectly comparable to the experimental ones (see figure17).

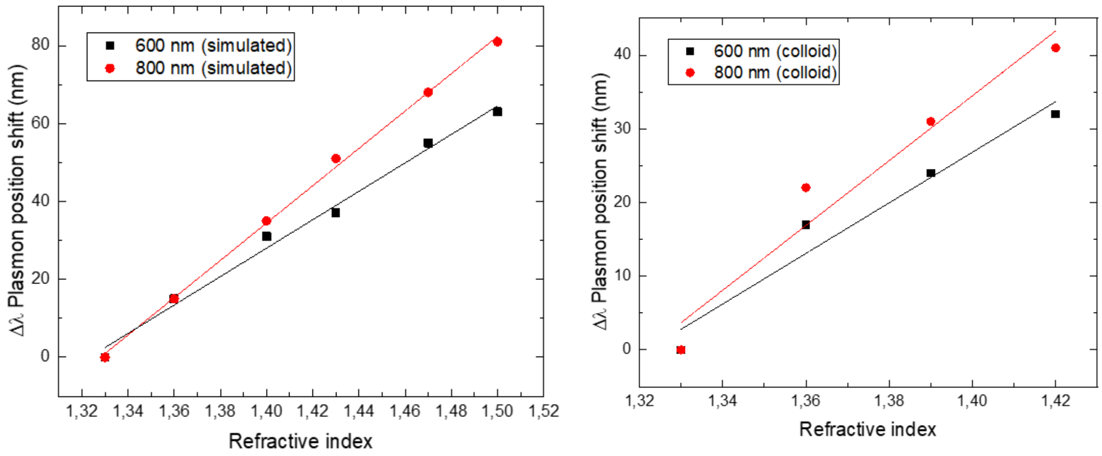

Figure 17: Simulated plasmon sensitivity compared with experimental plasmon sensitivity

Chapter 3: Light driven synthesis

We have seen that Ag nanoplates synthesis often occurs in two steps, since the first step is required to produce spherical NPs, while the second step transforms them into flat triangular nanoplates. This is necessary to separate the nucleation of new particles from their growth and shape transformation. The most widely used process so far is the so-called seed-mediated growth, where spherical particles are first produced by chemical reduction of Ag ions by $NaBH_4$, then transformed chemically by hydrazine and citrate (see previous chapter). Other methods were also proposed in place of the first or second step of the seed-mediated growth or both.

For example, chemically produced NPs can be transformed into NPTs using light irradiation or H_2O_2 or a combination of both. More recently, Ag NPTs were produced from laser-ablated Ag NPs using light irradiation and hydrogen peroxide (H_2O_2), fully avoiding the chemistry involved in the seed-mediated growth[97]. A few examples of a single-step synthesis of anisotropic Ag NPs have been reported[98]. However, most of the processes reported are very time consuming (from 12 h to 90 h). In this chapter, we report on the synthesis of Ag NPTs in a single step, combining the laser ablation process with light irradiation and H_2O_2, a process that is completed within less than one hour. We also investigated the plasmon sensitivity of such nanoparticles under a varying refractive index.

This chapter is based on the publications:

- Vittorio Scardaci, Marcello Condorelli, Matteo Barcellona, Luca Salemi, Mario Pulvirenti, Maria Elena Fragalà, Giuseppe Compagnini "Fast One-Step Synthesis of Anisotropic Silver Nanoparticles" Appl. Sci. 2021, 11(19), 8949
- V Scardaci, M Pulvirenti, M Condorelli, G Compagnini "Monochromatic light driven synthesis and growth of flat silver nanoparticles and their plasmon sensitivity" J. Mater. Chem. C, 2020,8, 9734-9741

3.1 Producing silver nanoparticles by laser ablation in water

Laser synthesis of colloids, powered by robust, high-power lasers, appears to be a key enabling process that is chemically clean and environmentally friendly, and appealing[99] for industrial manufacturing of functional nanomaterials while being useful in many different areas, such as: hydrogen generation and hydrogen storage[100], heterogeneous catalysis using colloidal high-entropy alloy NPs, anticancer, antimicrobial research, drug monitoring[101], additive manufacturing applications, and nonlinear nanophotonics[102]. In addition, NPs prepared by the Laser Ablation in Liquids

(LAL) have been recently used for various and unique applications like friction reduction, solar nanofluids, optical limiting devices [103] and so on. Laser Ablation in Liquid (LAL) for the production of nanostructures is based on the ejection of material by a laser pulse irradiating a solid target immersed in liquid. The laser matter interaction and the consequent ablation are strongly dependent on the irradiance and the duration of the pulse, on the background liquid, on the sample geometry and morphology as well as on the focusing condition. As it has been clearly established, ns-PLAL is based on a sequence of different processes: laser ablation and plasma induction, energy exchange from plasma to the liquid and consequent generation of the cavitation bubble and release of particles from the bubble to the solution. In (Figure 1)[104] the different LAL steps are summarized.

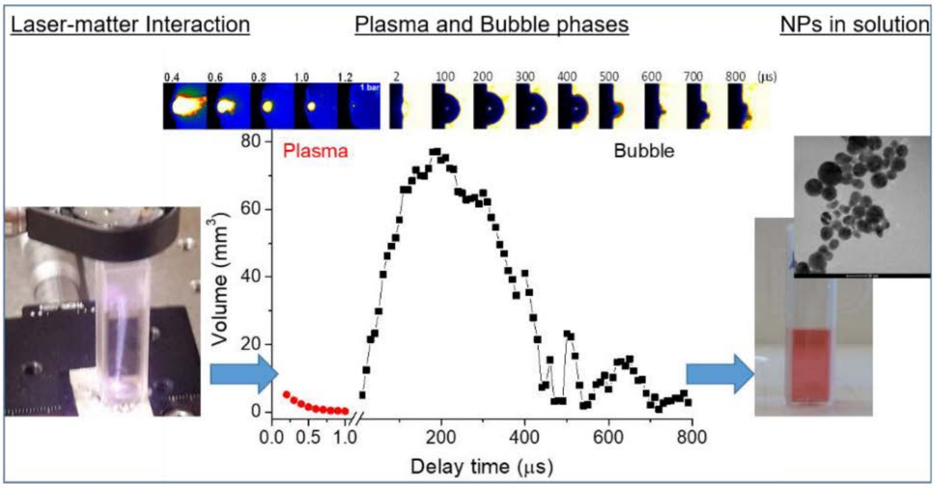

Figure 1: Schematic LAL steps picture taken from ref[104]

The basic mechanisms inducing the laser ablation in liquid, as well as their dependence on laser pulse properties, do not differ notably, with respect of laser ablation in gaseous environment. In the case of ns-laser ablation, just a portion of the laser pulse directly reaches the target surface, while most of the laser pulse is spent in electron heating by inverse bremsstrahlung. This implies that the ablated material is converted to a plasma phase during the laser pulse irradiation. Differently to what can be observed in a gas background environment, because of the water incompressibility, the ablated material is strongly confined and in turn reaches high density. This effect decreases the penetration of the laser through the plasma during the initial stage of expansion, inducing the propagation of gradient of temperature in the ejected material, i.e the plasma.The mechanisms concerning the evolution of the ejected material after laser ablation are strongly correlated to the duration of the laser pulse. Ideally, with a laser pulse with a shorter duration than a few tens of fs, the effect of the interaction of the laser pulse with the ejected material can be neglected and the evolution of the ablated material can be investigated with atomistic models. On the contrary, when the laser pulse is long enough (as in the case of ns) to effectively interact with the ablated material, inducing further ionization and electron heating, the role of the plasma becomes dominant and kinetics models coupled with fluidoynamics are required for a full description of the phenomenon.The fast transfer of energy from the plasma to the surrounding water induces the formation of a thin layer of vapor around the plasma border with high temperature and high pressure. In order to reach the equilibrium with the liquid, the vapor expands, producing a cavitation bubble. The bubble expands until it reaches the equilibrium with the surrounding liquid. Due to the fast expansion, the liquid at the border of the cavitation is compressed and when the pressure of the bubble reaches the minimum at the maximum of the expansion, the bubble is compressed and its shrinking stage begins. During this stage, the bubble increases its pressure again and impacts the target, eventually pushing back the material to the target surface. There are several models describing the evolution of a laser-induced bubble[105]. Most of these descriptions are based on a theoretical model simulating the bubble radius evolution, assuming the mass and momentum conservation equations in the liquid phase, and that the vapor pressure inside the bubble is balanced by the pressure on the liquid side of bubble wall.As a matter of fact, the high pressure of the plasma at this condition, i.e., under water confinement, allows for condensation at higher temperatures than those in standard condition. This observation indicates that NPs can be formed in the bulk of the plasma and not only in the border of the plasma where the plasma cools down fast as a consequence of the rapid exchange of energy between the plasma and the surrounding liquid. It may be assumed that also the material on the plasma border condensates in particle but being this zone of the plasma out of equilibrium, it produces particles with various sizes and shapes. On the contrary, particles formed in the bulk of the plasma, being the result of thermodynamic equilibrium between the processes of growth and the evaporation, are characterized by a spherical shape with narrow size distribution. Ag spherical nanoparticles can be prepared by pulsed laser ablation in liquid (see fig. 2). The full process is described elsewhere [106] and can be summarized as follows: a 1064 nm Nd:YAG laser (pulse duration 5 ns, repetition rate 10 Hz, fluence 0.6–1 J/cm2) is focused onto a silver target, which is immersed into an aqueous solution containing trisodium citrate (TSC) 10 mM. This process continues until the desired concentration is reached. In our case, we empirically determined that a sufficient concentration is achieved when the absorbance of the solution, measured in a 1 cm optical path cuvette, which typically happens beyond 0.05–0.06 mg/ml. This was estimated by measuring the weight loss of the Ag target during the process, once the volume of the liquid was known. We usually reached such desired concentrations within 30 min.

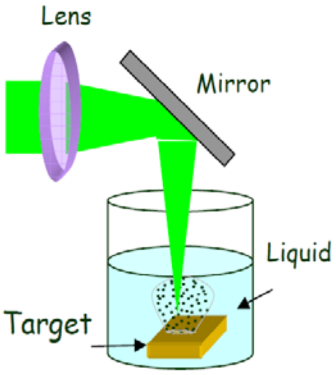

Figure 2: Our LAL configuration

3.2 Light driven reshaping

Silver nanoparticle seeds are stable if stored in the dark. This is because they can undergo size and shape change when the plasmon is excited with visible light. In fact, many groups have reported on thermal methods, as well as light induced morphological control of AgNP colloids[107]. For thermal methods of making nanoparticles, the presence of twinning defects in crystals as well as the choice of capping agents are two crucial factors to consider. Twinning defects occur when a single particle has at least two portions that are lattice mismatched with respect to each other. That is to say that these particles have crystalline regions but a plane between them since the crystalline portions do not align. Figure 3 depicts these types of particles, as well as a particle without twinning defects that can be formed from the migration of twinning defects upon annealing. It has been suggested that twinning defects are necessary in the formation of silver decahedra that are multi-twinned and silver nanoplates that have only one defect plane parallel to the plane of the largest exposed facets[108].

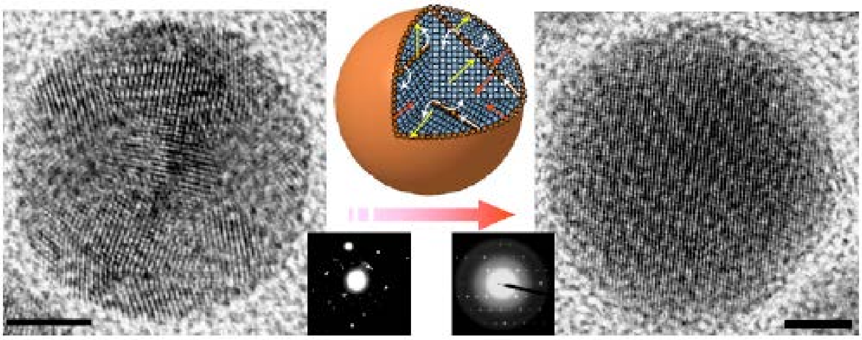

Figure 3: Representation of twinning defects[108]

The other major factor to consider in growing different shapes by thermal methods is the capping agent. AgNP crystalize in the face-centred cubic (fcc) crystal structure, and so, while spherical and spheroid nanoparticles expose both {111} and {100} facets, it is thermodynamically more stable for particles to form that expose the lowest energy {111} facets[109]. However, the different possible facets in a crystal have different surface energies, and different molecules bind preferentially to different facets. Therefore, by selecting the appropriate capping agent that preferentially binds to certain facets, one can slow down the addition of silver on these facets and in doing so control the final particle size and shape. This is the main idea in the well-known polyol synthesis for making nanoparticles of specific shapes. The polyol synthesis is possibly the most common synthesis technique for making various shapes of AgNP and AuNP. In this method, usually ethylene glycol serves as both the solvent and reducing agent, and poly (vinyl pyrrolidone (PVP) serves as a capping agent. The ratio between metal salt and PVP concentrations are crucial to the final morphology of the particles. The final shape of the particles is determined by the ratio of the growth rates on the {100} and {111} facets where a ratio of 1.73 provides octahedra and tetrahedra shaped particles that expose *{*111*}* facets, whereas a ratio of 0.58 provides cubic particles with less stable *{*100*}* facets exposed. It is believed that PVP either retards the growth rate on the *{100}* facets or increases the growth rate on the *{111}* facets, in which case the ratio of the growth rates is appropriate for forming cubes. Different particle morphologies expose surface atoms that can behave chemically different depending on which facet they are in, or if they are at vertices in a crystal. That is why various shapes of nanoparticles are often desirable in catalysis, for much the same reason that capping agents can affect the morphology during growth, which is due to preferential binding to particular facets. For example, the oxidation of styrene has been shown to occur preferentially on different shapes of nanoparticles[108]. Nanoplates, truncated nano cubes and other shapes have also been made by modified polyol processes. Photochemical synthesis of AgNP with various shapes has also been realized by a number of different groups[110]. In many of these reports, the realization of particular shapes has been attributed to twinning defects directing the growth of the particles, and in others the choice of capping agents has been attributed with the resultant shapes. From the large variety of shapes that were attainable from reaction solutions, and from the fact that precursor solutions with significant variations could beused to make the same morphologies of particles, the question of what the true growth mechanism is in most photochemical routes was brought into question.

3.3 Silver nanoplates by simultaneous ablation and irradiation - Experimental

Ag NPT synthesis took place according to the scheme shown in Figure 4. A quartz optically transparent reaction vessel was filled with a 1 mM solution of trisodium citrate (TSC). This gave a pH in the region of 8.5–9. A silver target was immersed in the vessel.

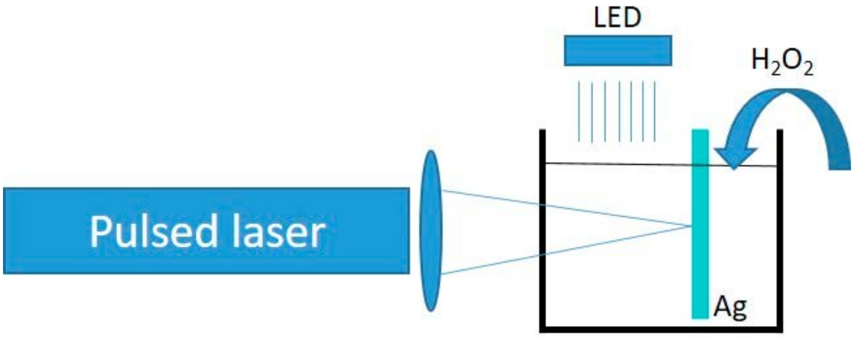

Figure 4: Schematic representation of our experimental setup

The beam of a Nd:YAG pulsed laser (Quanta System Spa, Varese, Italy) at 1064 nm (fluence 0.6–1 J/cm2, 5 ns pulse duration, 10 Hz repetition rate) was focused by a lens onto the silver target and produces Ag NPs by laser ablation. During the laser ablation process, a white light LED (Ekoo IP66, 100 W, see figure 5 for the emission spectrum) illuminated the reaction vessel, and H_2O_2 flowed into the solution as regulated by a peristaltic pump at a flow of 69 µL/min.

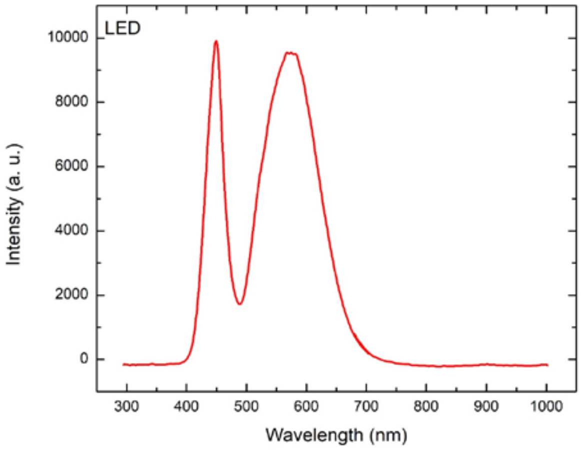

Figure 5: White LED emission spectrum

The overall setup is schematized in Figure 4. Small aliquots of the solution were taken at regular intervals to monitor the evolution of the reaction by UV-Vis spectroscopy (Agilent Cary 60 spectrometer, Santa Clara, CA, USA).The morphology of the obtained Ag NPTs was characterized by scanning electron microscopy (SEM) using a Zeiss SUPRA 55-VP (Carl Zeiss Microscoy, Oberkochen, Germany) system and atomic force microscopy (AFM) using a Witec Alpha 300 RS system (WITec, Ulm, Germany). For the SEM and AFM analysis, the Ag NPTs were deposited onto a silane-functionalized Si substrate immediately after synthesis. SEM image analysis was performed using the software ImageJ (Author: Wayne Rasband, National Institute of Mental Health, Bethesda, MD, USA). For plasmon sensitivity measurements, a solution obtained by the described process (15 mL) was initially centrifuged for 20 min at 10 K rpm. After the supernatant was removed, the deposit was redissolved in 1 mL of water and homogenized by very short ultrasonication (1 min). Then, 100 µL of the solution was added to 3 mL of water for a refractive index of 1.333 and to 3 mL of sucrose solution (22%, 40%, and 50% for a 1.367, 1.399, and 1.420

refractive index, respectively), and the absorption spectrum was then measured.

3.4 Light driven synthesis during the ablation

Figure 6 shows the UV-Vis absorption spectra of a solution that was exposed to our process for 30 min at 69 µL/min H_2O_2 flow, as well as a solution that was produced by laser ablation only. The latter showed a single sharp feature at 395 nm arising from the surface plasmon resonance of spherical Ag NPs. On the other hand, the spectrum exposed to irradiation and H_2O_2 flow during the laser ablation process appeared significantly different, as the main feature was red-shifted from that of spherical NPs, and additional features arose, including a low intensity one at 335 nm. Indeed, this is strong evidence that the Ag NPs in solution in this case were far from spherical and suggests that the nanoplates were formed during the process. The spectrum did not show significant variations by changing the H_2O_2 flow rate between23 µL/min and 69 µL/min, while increasing the flow rate above 100 µL/min caused complete oxidation of the formed material, and the corresponding absorption spectrum would appear flat. Similarly, decreasing the TSC concentration to 0.1 mM did not change the absorption spectrum significantly, while increasing it up to 10 mM caused complete oxidation of the formed material (flat absorption spectrum).

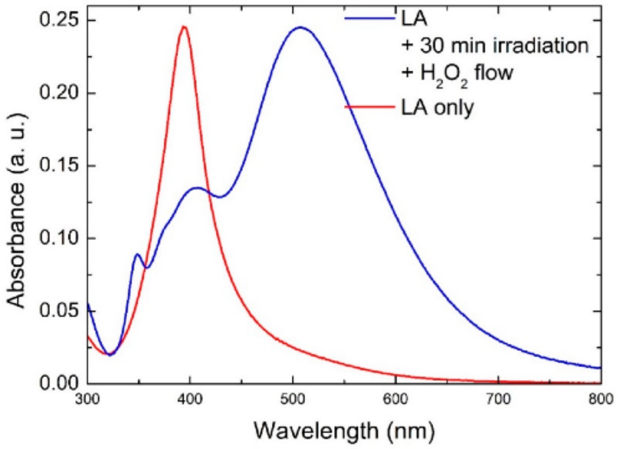

Figure 6: UV-vis absorption spectra of silver nanosphere red curve and silver nanoplates blue curve

As mentioned in the previous chapter, the main feature around 500 nm can be attributed to the in-plane dipole mode, while the peak at 335 nm can be attributed to the out-of-plane quadrupole mode, which is typical of Ag anisotropic structures. The other feature around 400 nm may be attributed to larger spherical NPs and/or to the in-plane quadrupole and out-of-plane dipole modes for NPTs or both. We also performed control experiments using either light irradiation or H_2O_2 flow only. When only irradiation was used, without introducing any H_2O_2, the process yielded only spherical NPs, with an absorption spectrum close to that shown in Figure 7 when only H_2O_2 was introduced in the solution, without light irradiation, the transformation happened only to some extent (see Figure 7a). We also performed a further control experiment, using no citrate in the solution. In this case, we observed an absorption spectrum with a single broad and asymmetrical feature (Figure 7b), suggesting that only a broad distribution of spherical particles was formed. Such results indicate that citrate, light irradiation, and H_2O_2 are all essential ingredients that cooperate in a successful process.

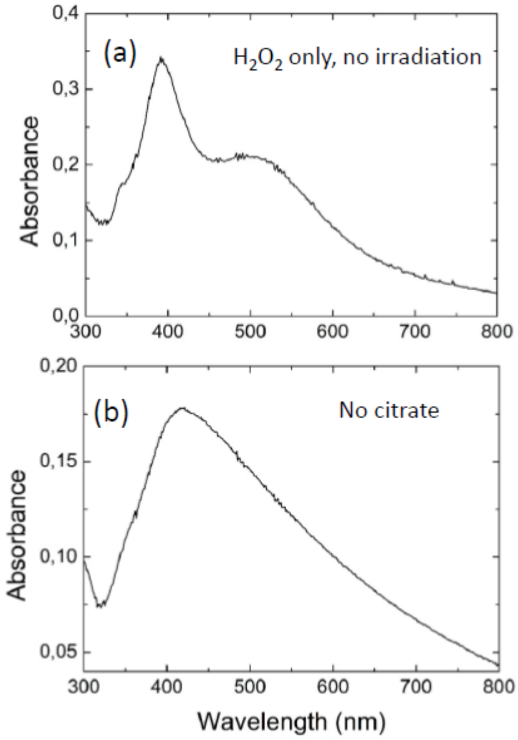

Figure 7: Spectra obtained by changing the operational parameters.

Figure 8 a,b shows representative SEM images of Ag NPTs produced by our process. We can observe Ag NPTs showing a mixture of shapes, including triangles, hexagons, circles, and other irregular ones. The size distribution shows that most NPTs were 70–90 nm in size (Figure 8c).

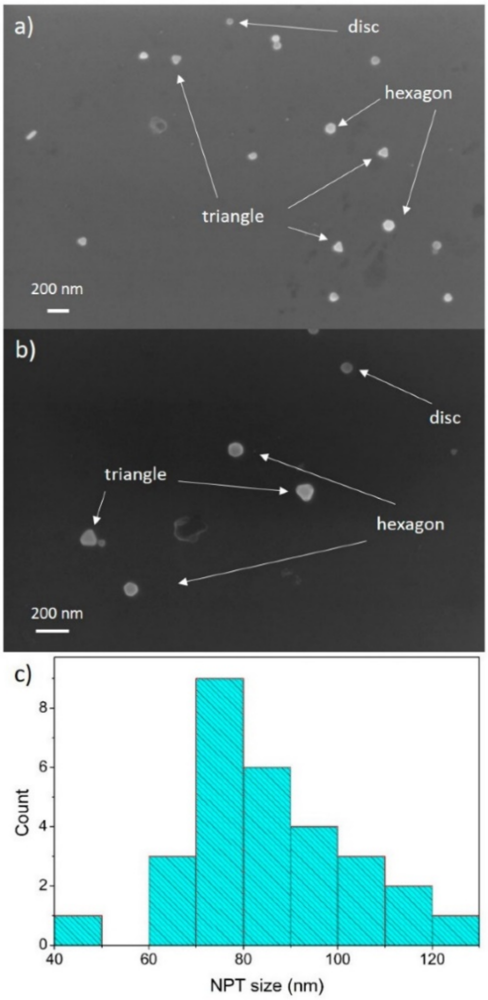

Figure 8: SEM images and relative distribution size

Figure 9 shows an AFM image and the profiles obtained from the same samples analyzed by SEM. Figure 9a also shows NPTs with mixed shapes, and Figure 9b shows the thickness ranging between 10 nm and 25 nm.

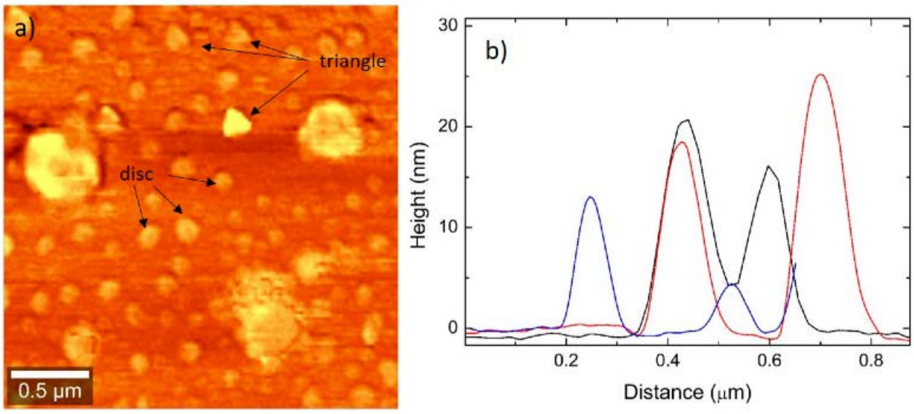

Figure 9: a)AFM image, b) Sections

The growth mechanism in this process can be elucidated within the framework of the reactions taking place among citrate, Ag, and H_2O_2 in the presence of light. It is known that, in the presence of light, citrate is able to reduce Ag+ to Ag0[111].

$$\text{Citrate}^{3-} + \lambda \rightarrow \text{Acetone-1,3-dicarboxylate}^{2-} + CO_2 + H^+ + 2e^-$$

$$Ag^+ + e^- \rightarrow Ag^0$$

At the same time, H_2O_2 can both oxidize and reduce silver[112].

$$2Ag + H_2O_2 \rightarrow 2Ag^+ + 2OH^-$$

$$H_2O_2 + 2Ag^+ + 2OH^- \rightarrow 2Ag + 2H_2O + O_2$$

Besides reducing Ag in the presence of light, citrate also has the function of being a capping agent for Ag NPs, as it easily binds to the (111) facets of silver. This allows both NP stabilization in solution and their preferential growth along the Ag (100) direction, which is less preferred by citrate. Hence, Ag NPs initially produced by the laser ablation process were first oxidized by H_2O_2, being partially dissolved in the liquid medium, and then reduced back by citrate, supported by H_2O_2, adding preferentially to the uncapped (100) Ag facet. It is interesting to note that the absorption spectrum shown in Figure 10 did not dramatically change its shape after about 10 min of this process, while the intensity increased and then stabilized over time as reported in figure 10. This suggests that an equilibrium was reached within the solution between the production of NPs by laser ablation and their conversion into NPT and that after reaching this equilibrium, the process only increased the NPT concentration in the solution.

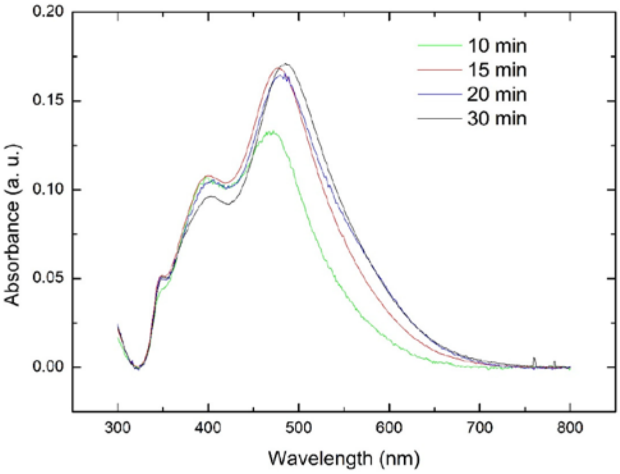

Figure 10: NPT formation over the time

3.5 Simulations of the extinction spectra

Simulations of the extinction spectra were performed to support and complement the experimental results. Simulations were performed using the commercial COMSOL Multiphysics package (from COMSOL Inc., Stockholm, Sweden) in the frequency domain. The simulated spectra were obtained using radiation perpendicular to the flat/larger side of the NPT, with polarization parallel to the same side[113].

Figure 11 shows simulated extinction spectra for NPTs of a round and hexagonal shape, with a size of 70 nm and 82.5 nm and a thickness of 10 and 20 nm, representative of the structures observed by SEM and AFM.

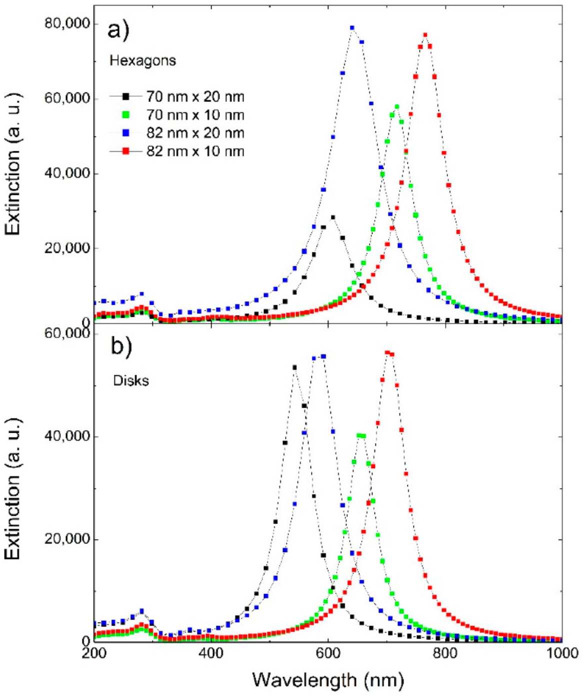

Figure 11: simulated extinction spectra for NPTs of a round and hexagonal shape, with a size of 70 nm and 82.5 nm and a thickness

Figure 12 shows the experimental absorption spectrum, already shown in Figure 6, with the simulated ones. It can be observed that the simulated spectra were mainly in agreement with the longer wavelength part of the experimental spectrum. This partial disagreement might be due to the fact that the simulated spectra were obtained for isolated NPTs, thus not taking into account the interaction among the particles and the particles distribution itself. However, this aspect is still unclear and will be subject to further investigation.

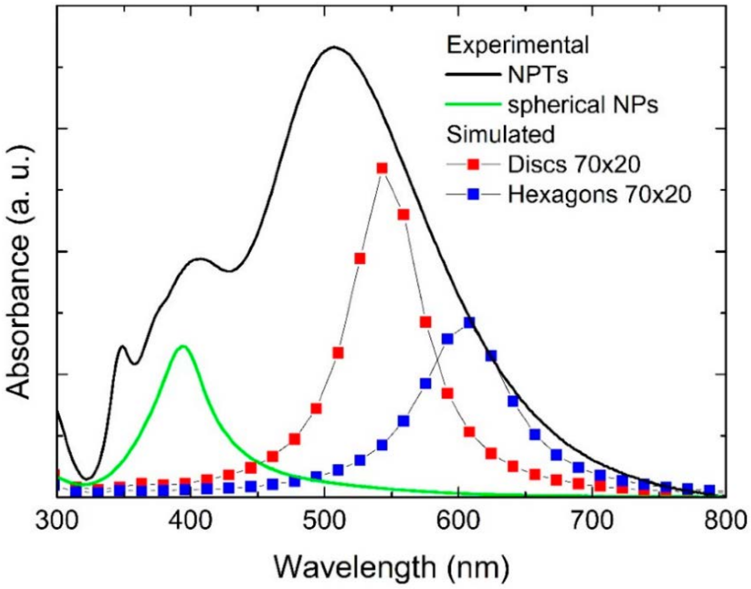

Figure12 : Comparation between the experimental spectra with the simulated ones

3.6 Plasmon sensitivity

The obtained NPTs were finally tested for plasmon sensitivity (S), i.e., the variation of the plasmon resonance peak position due to a change in the refractive index ($S = \Delta\lambda/\Delta n$), which is typically reported in terms of nm/RIU (refractive index unit). To change the refractive index, we used sucrose solutions at set concentrations, since the relation between sucrose concentration in water and the refractive index is well established[114]. Figure 13 shows the plasmon resonance peak position of a Ag NPT solution produced by our process by varying the refractive index, along with the data simulated for disks of 70 nm in size and 20 nm in thickness. Fitting the data yielded a plasmon sensitivity S of 216 nm/RIU, close to that obtained by the simulations. This value is comparable to the others, typically below 250 RIU, reported in the literature for Ag NPTs with a similar plasmon resonance[115], with the advantage of obtaining the nanostructures in a fast and simple one-step process, despite the poor SPR tunability. If we compare the experimental data with those obtained from the simulation of discs and hexagons (70 nm × 20 nm), we observe that the simulated data showed a higher plasmon sensitivity. This was probably due to a higher SPR wavelength in the simulated spectra, which was expected to exhibit higher plasmon sensitivity.

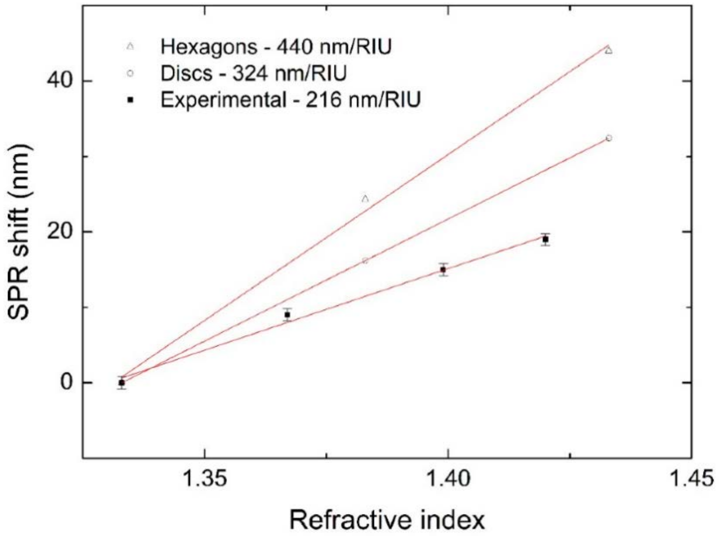

Figure 13. Comparation between Plasmon sensitivity fitting of the experimental nanoparticles with simulated nanoparticles

3.7 Light reshaping of laser ablated spherical particles into nanoplates

In a second set of experiments, laser produced spherical particles were subsequently transformed by adding small amounts of H_2O_2 (up to 1µl per ml of solution) at intervals of approximately 5 minutes while the solution was stirred under LED irradiation at wavelengths of 405 nm (600 mW), 515 nm (160 mW), and 730 nm (350 mW). A small amount of sodium chloride (18 µm) was added to the solution before adding H_2O_2. The irradiated solution was in a cuvette for optical measurements and the LEDs were focused inside such cuvette with a spot of around 7mm x 7mm. LEDs were sourced from Prizmatix.

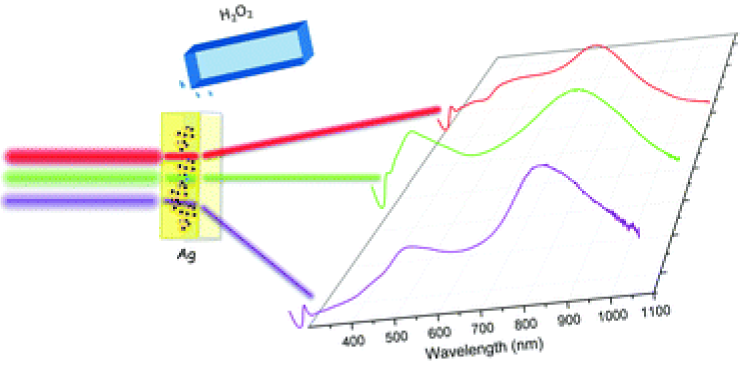

Figure 14: Absorption spectra of silver nanoplates exposed with three different monochromatic irradiation

In figure 14 the optical absorption spectra of our Ag NP solutions are shown, while they are exposed to cumulative H_2O_2 additions under three different monochromatic irradiation wavelengths (405 nm, 515 nm, and 730 nm) at the maximum power available and at different trisodium citrate (TSC) concentrations (1 mM and 10 mM). TSC concentration is set before the PLAL process and no longer modified during the subsequent steps. The absorption spectrum of the initial NPs, involving a solution diluted three times and measured in cuvettes with a 10 mm optical path, shows a plasmon resonance centered around 393 nm, regardless of the TSC concentration. This corresponds to an approximate size of 10 nm[116]. Since the optical extinction coefficient increases sharply with particle size, larger particles weigh more in the absorption spectrum, thus a particle distribution of 5–10 nm can be inferred. All experiments started from a similar concentration of nanospheres in the region of 80 mg L^{-1} or 7.5×10^{-4} M in total Ag, as estimated after weighing the Ag target before and after the PLAL process. This translates into a 12 nM concentration of Ag nanoparticles, as estimated using an extinction coefficient ε = 6.5×10^8 L mol^{-1} cm^{-1}. To estimate this concentration we had to dilute the original solution 20 times in order for it to fall in the range of linearity of the Lambert–Beer law. The [TSC]/[Ag] ratio is thus ~13 for [TSC]=10 mM and ~1.3 for [TSC]=1 mM.

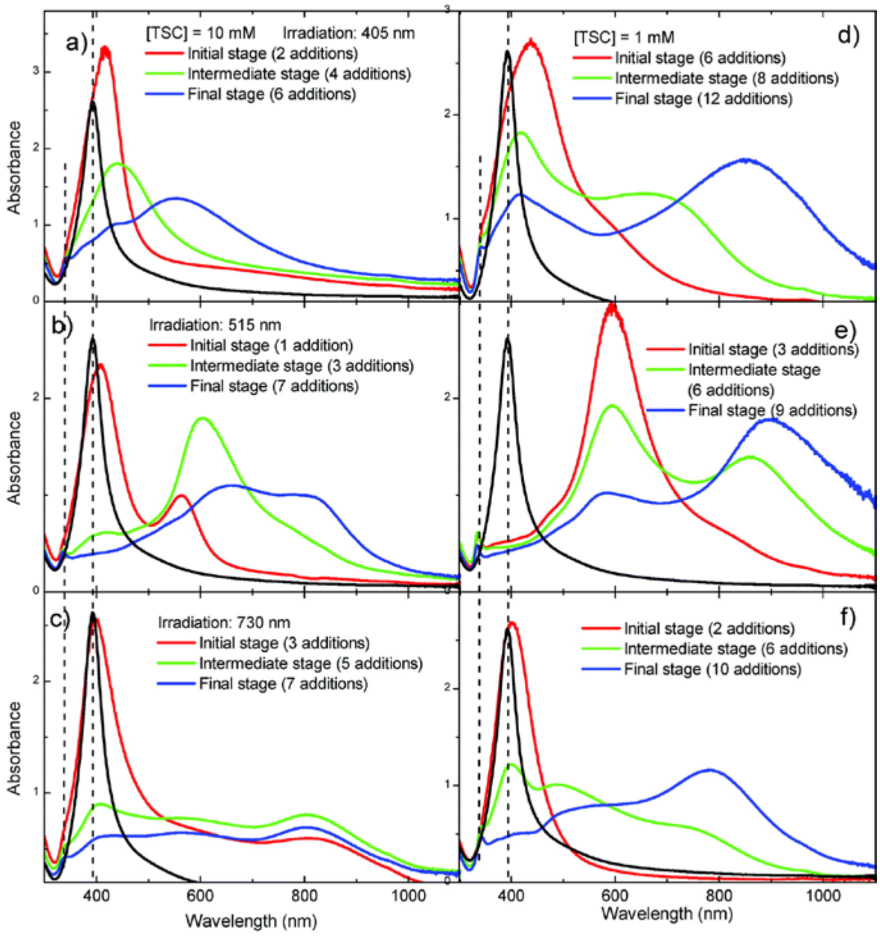

Figure 15: Absorption spectra from Ag nanoplates, at early (red lines), intermediate (green lines) and final (blue lines) growth stage at TSC 10 mM (left column) and 1 mM (right column) and at 405 nm (top line), 515 nm (middle line) and 730 nm (bottom line) irradiation wavelength, and initial spherical nanoparticles (black lines). Vertical dashed lines correspond to the plasmon resonance of sherical nanoparticles at 393 nm and to the transverse quadrupole resonance of flat nanoplates at 330-345 nm.

Absorption spectra obtained from all processes shown in undergo a dramatic shape change as well as a significant red-shift upon multiple subsequent

H_2O_2 additions during irradiation. While the absorption spectrum of spherical Ag nanoparticles shows a single, narrow peak at 393 nm, after H_2O_2 addition and irradiation the spectra show broader plasmon resonances, red-shifted from spherical particles, with in-plane dipole mode peak positions dependent on particle size. We also observe the longitudinal quadrupole and transverse dipole modes around 400 nm, which can be overshadowed if spherical particles are still present in the solution, and the transverse out-of-plane quadrupole mode in the region of 330–345 nm, which is an indication of anisotropy and suggests the presence of flat particles. Hence, this suggests that initial spherical Ag NPs are being converted into flat nanoplates. However, different irradiation wavelengths, as well as different TSC concentrations, have a significant impact on the transformation process. At [TSC]=10 mM, all processes seem to begin with Ag NP growth. This is evident from the broadened plasmon resonance peak in the region between 400 and 420 nm, appearing after 1–3 H_2O_2 additions, and red-shifted from the initial one at 393 nm. At 405 nm irradiation, subsequent H2O2 additions cause the spectra to red-shift only up to 550 nm, indicating the formation of small nanoplates. At 515 nm irradiation, a two-step growth seems to occur, as spherical NPs are initially converted into nanoplates with plasmon resonance around 600 nm, to form bigger structures, with a broad plasmon resonance that extends beyond 800 nm, at a later stage. At 730 nm irradiation, the initial spherical NPs are converted straight into large nanoplates, with plasmon resonance around 800 nm. Nonetheless, the yield seems to be low, as most NPs seem to be lost in the process, compared to irradiation at the shorter wavelengths. The process, at 730 nm irradiation, looks similar at [TSC]=1 mM, although the yield appears slightly higher. On the other hand, irradiation at 405 nm and 515 nm at [TSC]=1 mM allows the growth of larger nanoplates, as evident from a red-shifted plasmon resonance, compared to the corresponding systems observed at TSC 10 mM. At 405 nm irradiation, the difference caused by lowering the TSC concentration is particularly dramatic as the plasmon resonance lies around 850 nm at the end of the conversion process, compared to 550 nm at higher TSC concentration. At 515 nm irradiation, we observe an immediate conversion into flat structures after only three H_2O_2 additions, with plasmon resonance around 600 nm, which then progresses towards larger structures with plasmon resonance around 900 nm after nine H_2O_2 additions. It is clear that, except for the 730 nm irradiation case, lowering the TSC concentration causes a red-shift of the plasmon resonance, indicating the formation of larger structures. We also note that the transverse quadrupole mode has a shift depending on the irradiation wavelength (see figure 15 for a close-up view). It lies at 340–342 nm under 405 nm irradiation and 333–334 nm under 515 nm irradiation, regardless of TSC concentration. On the other hand, at 730 nm irradiation this mode appears at 335 nm at 10 mM TSC and 342 nm at 1 mM TSC.

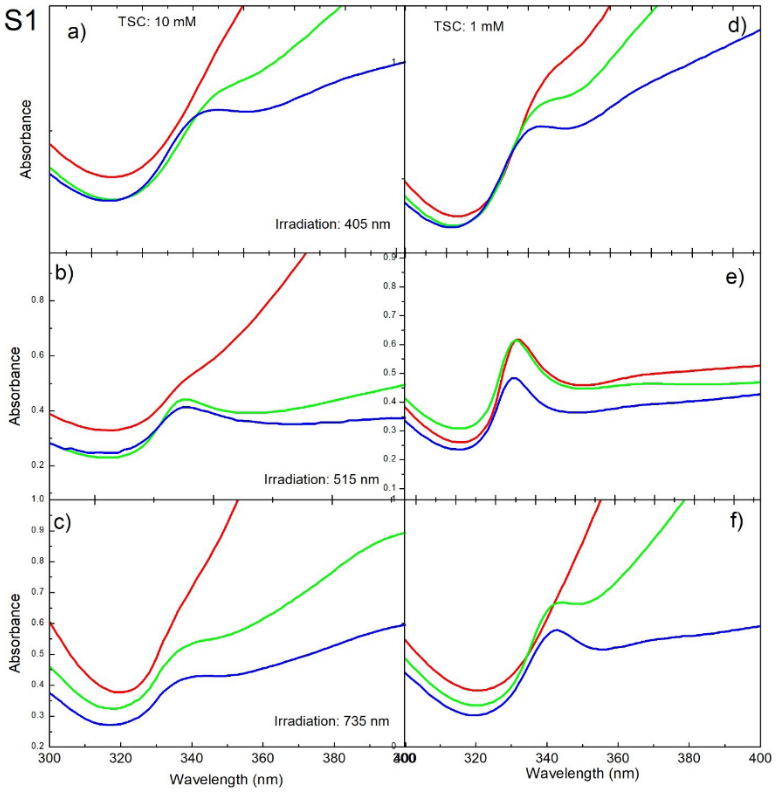

Figure 16: Transverse quadrupole shift due to different monochromatic light irradiation wavelengths

Similar experiments carried out at low power irradiation at 515 nm did not produce significant differences as shown in figure 16.

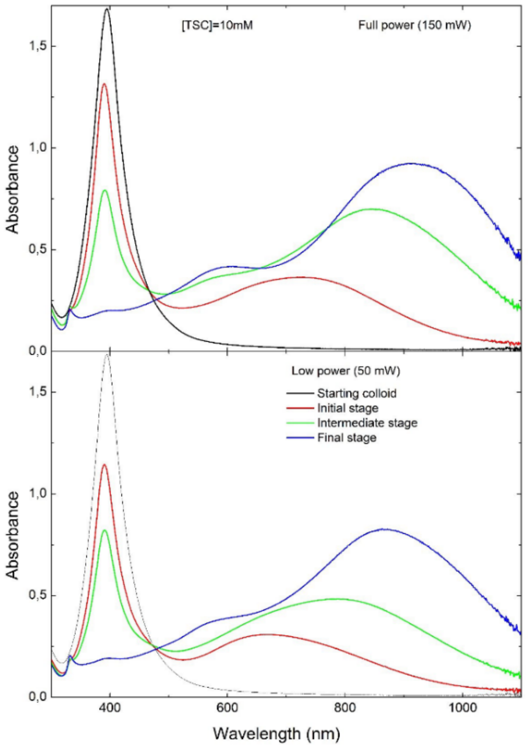

Figure 17: Similar experiments as figure 15 but with different irradiation power

It is important to point out that, under irradiation only, without the addition of H_2O_2, initial NPs undergo very limited transformation at 405 nm and 515 nm, or none at all at 730 nm (figure 17 a,b,c). Adding H_2O_2 in the absence of light irradiation produces very broad plasmon resonances (figure 17 d). It is thus clear that the three elements, irradiation, TSC and H_2O_2 work synergistically for the successful completion of the process.

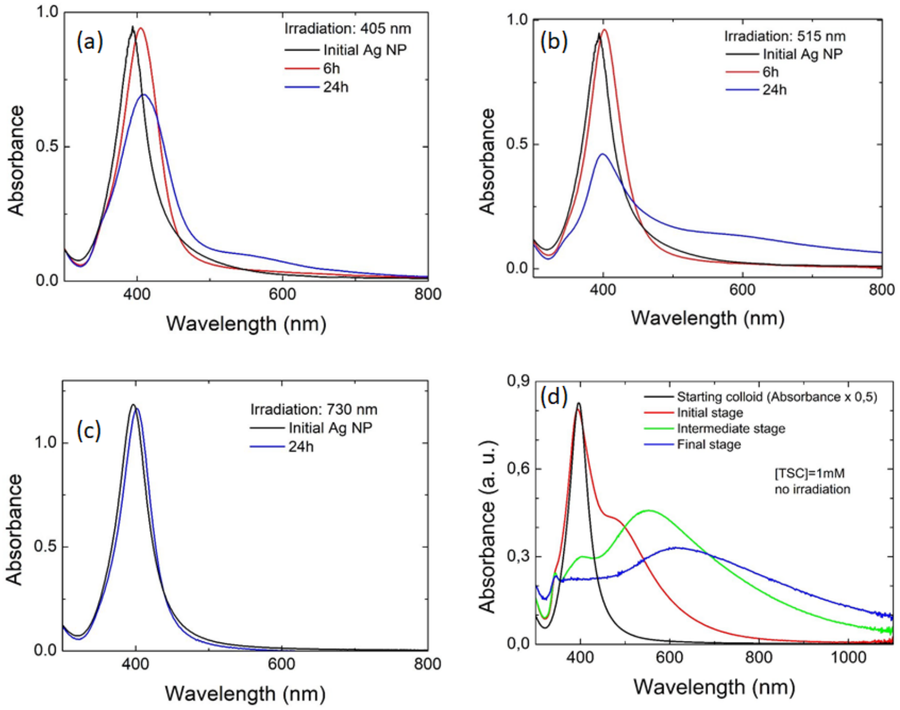

Figure 18 :a,b,c) very limited transformation at 405 nm and 515 nm, or none at all at 730 nm with only light irradiation. d) Adding H_2O_2 in the absence of light irradiation

Interestingly, having the incident light in resonance with the plasmon does not have a significant impact on the growth of the nanoplates and their size. It is also important to note that our method of rapid addition of H_2O_2 molecules allows the complete transformation of spherical nanoparticles into flat nanoplates within 1–2 hours, while in many cases, the reported process requires a time of several hours to two days. Scanning electron microscopy (SEM) has been performed on samples taken from all solutions shown in Figure 18. Table 1 summarizes the average size of the Ag nanoplates as measured from SEM images under all conditions discussed here. Indeed, under 405 nm and 515 nm irradiation the average size of the Ag nanoplates is higher at lower TSC concentrations. It is important to note that differences in values are tested for statistical significance using the Student t-test, which confirmed that the values are actually different within significance levels lower than 0.0005.

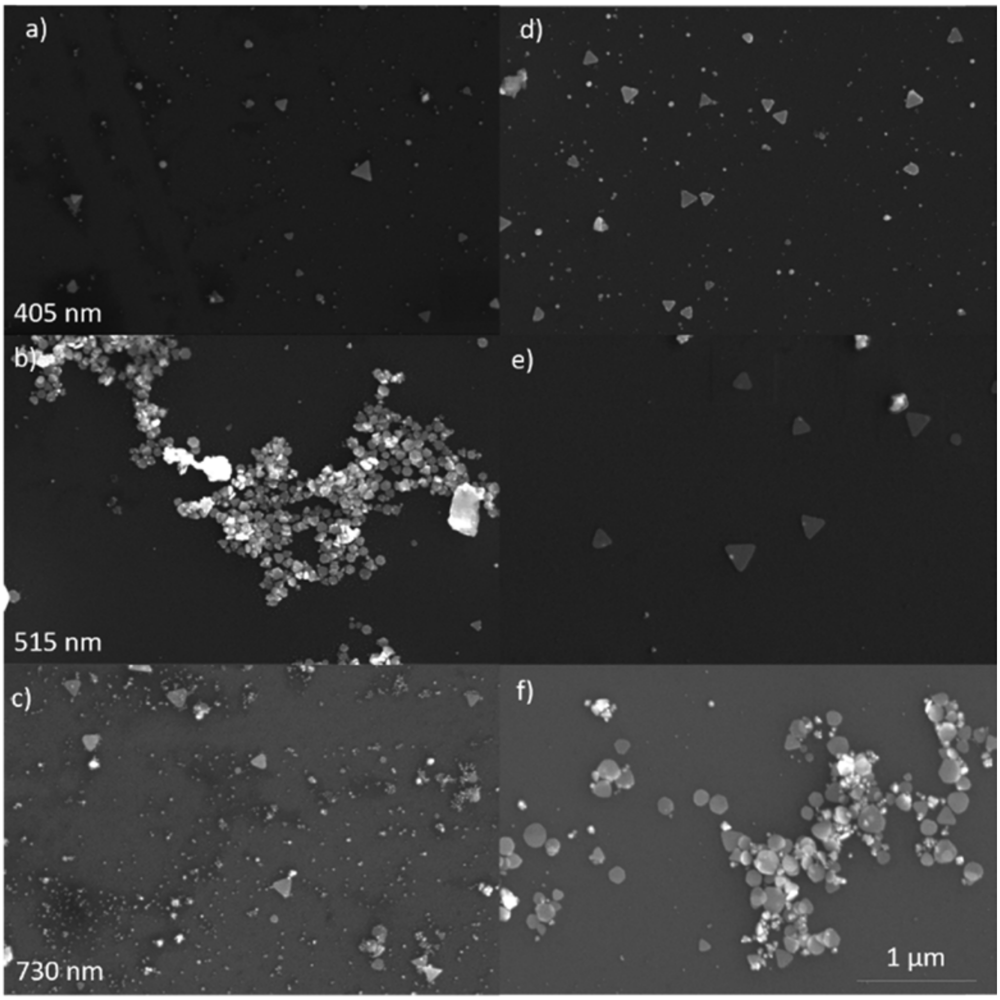

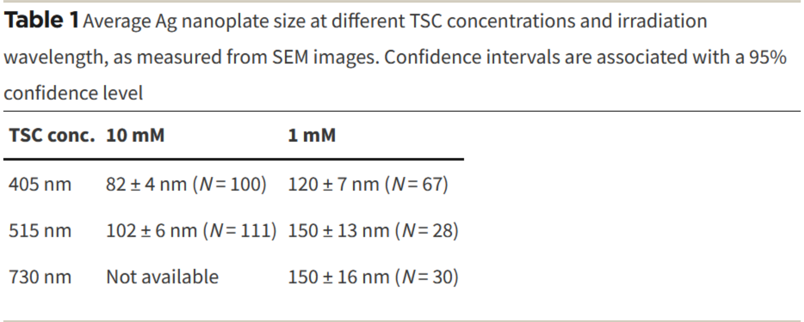

Table 1 Average Ag nanoplate size at different TSC concentrations and irradiation wavelength, as measured from SEM images. Confidence intervals are associated with a 95% confidence level

TSC conc.	10 mM	1 mM
405 nm	82 ± 4 nm (*N* = 100)	120 ± 7 nm (*N* = 67)
515 nm	102 ± 6 nm (*N* = 111)	150 ± 13 nm (*N* = 28)
730 nm	Not available	150 ± 16 nm (*N* = 30)

Fig 19: SEM images of Ag NPTs grown at [TSC]= 1mM

Fig. 18 shows SEM images of Ag nanoplates grown at [TSC]=1 mM at different stages of the transformation process, and are related to the absorption spectra shown in Fig. 19d–f. At 405 nm irradiation the nanoplates are already triangular at the intermediate stage and retain their shape until the end of the process (Fig. 19a and d). Under 515 nm irradiation, the nanoplates are present in a mixture of shapes, mainly hexagons, at the intermediate stage, while in the final stage all nanoplates show up as regular triangles, with rounded tips (Fig. 18b and e). At 730 nm the situation seems flipped, as we can observe the majority of triangular nanoplates at the intermediate stage and a mixture of shapes, mainly rounded, at the final stage (Fig. 18c and f). Residual smaller nanoparticles can be noted under 405 nm and 730 nm irradiation. Figure 20 shows SEM images of the Ag nanoplates transformed at [TSC]=10 mM. Compared to Fig. 2, the nanoplates appear smaller. Indeed, our investigation shows an average size of 82 nm at [TSC]=10 mM compared to 120 nm at [TSC]=1 mM at 405 nm, and an average size of 100 nm at [TSC]=10 mM compared to an average size of 150 nm at [TSC]=1 mM at 515 nm (Table 1).

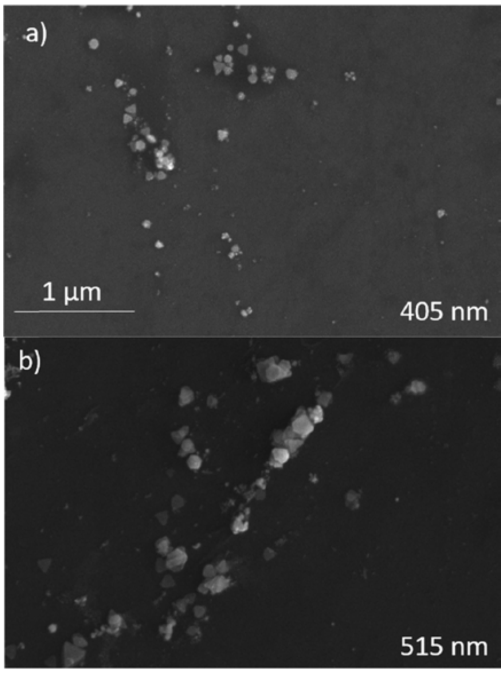

Fig 20: SEM images of the Ag nanoplates transformed at [TSC]=10 mM.

Conclusion

Here we demonstrated the fast and facile synthesis of Ag NPTs in a single step by combining laser ablation in liquids with light irradiation in the presence of H_2O_2. We obtained flat NPTs of mixed shapes with sizes between 60 and 80 nm and thicknesses of 10–20 nm. The SPR resonance of these nanostructures fell around 500 nm. While at this stage, the process seems to be efficient in a narrow range of parameters, with poor SPR tuning capability, we foresee that exploring a wider range of conditions, such as laser ablation parameters or the chemical composition of the solution, might provide some SPR tuning capability to some extent. Changing the refractive index of the surrounding medium yielded a plasmon sensitivity of 216 nm/RIU.

Moreover we investigated the transformation of spherical Ag nanoparticles, produced by PLAL in the presence of citrate, into triangular nanoplates under different irradiation conditions and rapid addition of H_2O_2 molecules. Results clearly show that citrate with a higher concentration produces smaller and thinner nanoplates, while citrate with a lower concentration promotes the formation of larger and thicker nanoplates, wherein plasmon resonance is significantly red-shifted towards the near IR optical region. Overall, by simultaneously manipulating irradiation conditions and the solution environment, we are able to tune the plasmon resonance across a wide range in the visible and near IR optical regions.

Chapter 4: Surface deposition and Plasmonic sensing devices

Noble metal nanoparticles have found a lot of applications in different scientifical and technological area such as sensing, solar cells and biological and medical field due to their capability to couple with the electromagnetic radiation in the visible and infrared(IR) regions. Metal nanostructure's plasmon response is involved in different phenomena relating to molecular sensing. The collective electron oscillations confined at the surface of a noble metal nanostructure (Localized Surface Plasmon Resonance, LSPR), naturally couple with the electromagnetic waves, and propagate at the boundary between the metal and adjacent dielectric. As we seen in the previous chapter LSPR depends on the metal, the geometry of the particles and dielectric properties of the environment. Variation of the refractive index for non-absorbing environment causes a plasmon wavelength shift. Due to this behaviour metal nanoparticles can be used in the sensor field and this feature is known as plasmon sensitivity, in the previous chapter it was described plasmon sensitivity in liquid. So nowadays, LSPR based sensors attract wide interest because of versatile application fields and relatively easy instrumental implementation, as recently reviewed[117]. Optical properties in terms of scattering, absorption, and extinction cross section depends on the materials and the shape of the nanoparticles so one of the most important tasks is the control of the morphology of the nanoparticles is needed. In a previous chapter it was discussed the synthesis of some silver nanoparticles in the colloidal state obtained through a Seed Mediated Growth (SMG) method in colloidal state and it was demonstrated that SMG is one of the most efficient and versatile method to synthetize in general all kind of noble metal nanoparticles in colloidal solution, with controllable size and shape with controllable plasmonic properties. For this reason, the obtained nanoparticles are particularly useful for imaging in the biology field and medical therapies and/or diagnostics[118–123]. Besides the nanoparticle's features, a LSPR sensing device must be designed according to the production strategy under consideration. For example, plasmonic nanostructures can be directly produced on a substrate, as in lithographic approaches (such as electron beam lithography). In this case, the control on the formation of the deposit is high, but the system is generally too expensive for practical applications. Other deposition methods, such as island annealing or sintering, cannot control the shape of the nanoparticles, while nanoimprinting hardly creates elemental components with gap distances of a few nanometers[124]. Spin coating is known to be widely adopted, but also requires a high amount of material, most of which is simply wasted[125]. Screen, or inkjet, printed substrates, on the other hand, are interesting techniques for large-scale productions, but printing parameters and ink formulations require challenging optimizations[126]. The aim of this chapter is related to the easy fabrication of a low-cost and reusable plasmonic sensing device by transferring the LSPR features of different Ag nanoplates onto the surface of the inner walls of disposable PMMA cuvettes and the fabrication of low cost plasmonic bio sensor device.

This chapter is based on the results published in the paper: M.Condorelli, L.Litti, M.Pulvirenti, V.Scardaci, M.Meneghetti, G Compagnini,"Silver nanoplates paved PMMA cuvettes as a cheap and re-usable plasmonic sensing device" Appl. Surf. Sci. 566 (2021) 150701

4.1 Review of some metal nanoparticles deposition methods

Currently available method for metallic nanostructure film includes electron beam lithography, solid-state thermal dewetting and self assembling methods.

4.1.1 Electron beam lithography

Electron beam lithography (often abbreviated as e-beam lithography or EBL) is the process of transferring a pattern onto the surface of a substrate by first scanning a thin layer of organic film (called resist) on the surface by a tightly focused and precisely controlled electron beam (exposure) and then selectively removing the exposed or nonexposed regions of the resist in a solvent (developing). The process allows patterning of very small features, often with the dimensions of sub-micrometer down to a few nanometers, either covering the selected areas of the surface by the resist or exposing otherwise resist-covered areas. The exposed areas could be further processed for etching or thin-film deposition while the covered parts are protected during these processes. The advantage of e-beam lithography coupled with SEM consists on using accelerated electrons that have shorter wavelength compared to the wavelength of ultraviolet (UV) light used in photolithography, which allows defining much smaller diffraction-limited features. On the other hand, direct writing of patterns by scanning electron beam is a slow process and results in low throughput. Therefore, EBL is used for preparing photomasks for photolithography or for direct writing of small-area, low-volume patterns for research purposes. EBL, on the other hand, is a modified SEM system in the figure 1 are reported two typical schemes.

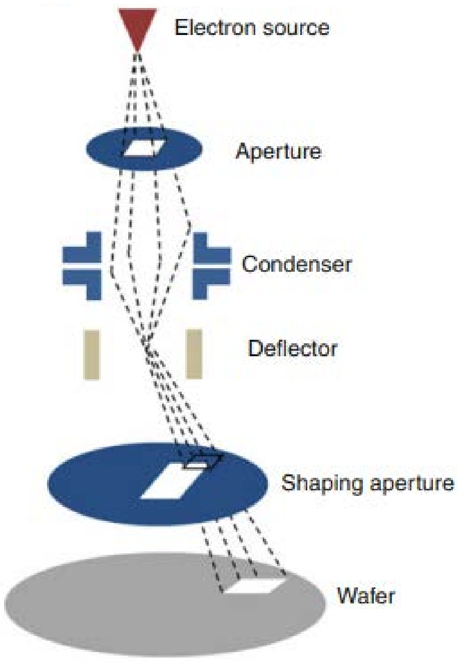

Figure 1: Different EBL modified SEM scheme

Electron beam lithography (EBL) has consolidated as one of the most common techniques for patterning at the nanoscale meter range. It has enabled the nanofabrication of structures and devices within the research field of nanotechnology and nanoscience such as the precise placement and design of arbitrarily shaped NPs with a large selection of geometries of various sizes with fine features. It offers a high resolution of around 10 nm since it is not limited by diffraction limits unlike other optical lithography methods[127,128]. In the following figure 2 are reported two SEM images of silver nanoparticles synthetized with EBL technique

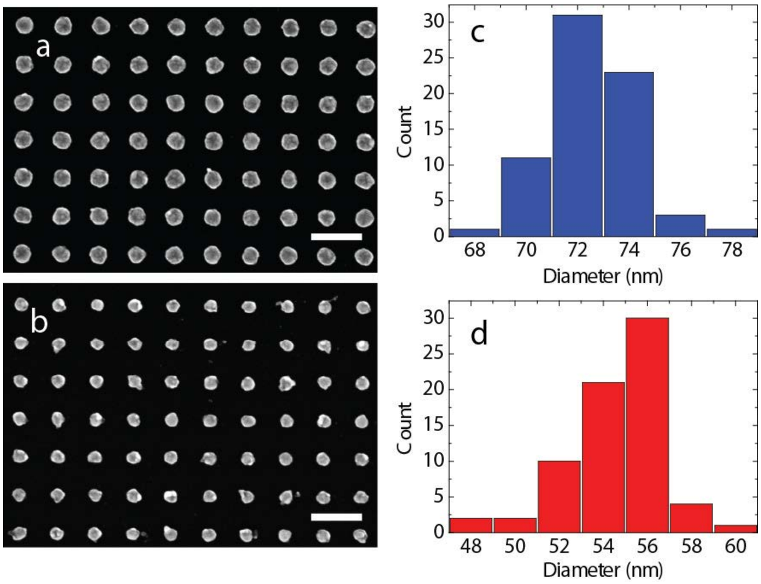

Figure 2: Two different family of silver nanoparticles synthetized with EBL technique with relative size statistics[129]

4.1.2 *Solid-state de-wetting*

Solid-state de-wetting (SSD) is a simple, low-cost, and industrially known scalable approach for the fabrication of substrate-bound metallic nanoparticles arrays onto various substrates, including glass, α-$Fe_2O_3(0001)/\alpha\text{-}Al_2O_3(0001)$,α-$Fe_2O_3(0001)/SrTiO_3(111)$, and ceramic single-crystals such as c-plane sapphire (α-Al_2O_3) and silicon[130]. In recent years, it has received a lot of interest as a viable approach for the large-scale fabrication of advanced photonic nanostructures[131,132]. SSD is a spontaneous phenomenon where a continuous polycrystalline metallic thin film onto a surface rearranges itself into an ensemble of separated islands or droplets upon appropriate annealing[131,132]. The original continuous film breaks apart into numerous particles in the same way as a water layer would on a hydrophobic surface, and this process is known as de-wetting [131,132]. The SSD process can be induced by thermal annealing[133], pulsed laser heating[134], combined thermal annealing and pulsed laser heating[135], ion beam irradiation[136], electron beam irradiation[137], and inductively coupled plasma discharge[138]. Nonetheless, thermal annealing is probably the simplest way to promote de-wetting, particularly when working on large areas. Deposited metallic films with thickness of a few nanometers are defective metastable layers that are comprised of polycrystalline grains (formed in a Volmer–Wever growth mode) with nanoscale islands that strain toward each other as they merge[131,132]. Then, de-wetting can occur at temperatures considerably below the melting point of the material, highlighting the island structure, which appears in the initial pristine polycrystalline precursor film [131,132]. The main driving force for SSD is the reduction in the total free energy at the interfaces between the air, film, and substrate, which occurs via diffusive mass transfer at the surface, interface, or grain boundaries[131,132]. Thus, controlling the SSD process parameters in a precise way creates the possibility of obtaining nano-objects with a pre-defined statistical size and spatial distribution (starting from a thin polycrystalline metallic film), avoiding complicated and expensive lithographical subtractive processes, Figure 3 shows nanoparticles self-assemble after de-wetting process.

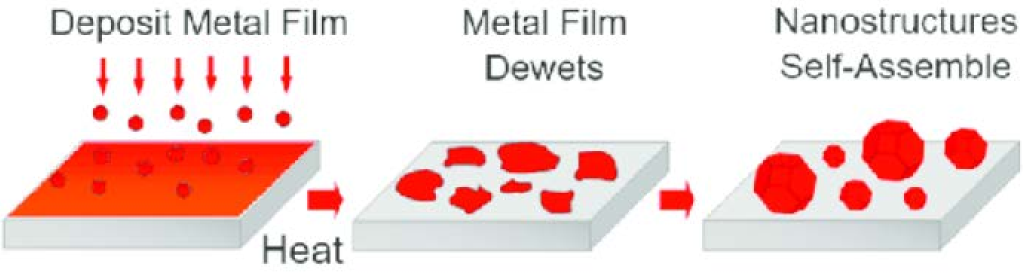

Figure 3: Scheme of typical nanoparticle dewetting synthesis

4.1.3 Deposition of preformed metal nanoparticles through organic self assembled monolayers

Molecular self-assembly or self-organization is a technique which is widely used for the spontaneous arrangement of nanomaterials. Coupling agents such as thiol-terminated, amine terminated, alkyl-terminated and phenyl-terminated silanes on metal nanoparticles (so called adsorbates) attach on various substrates through their terminal groups[139,140]. Among them, amino-propyl-triethoxysilane (APTES) is probably the best-known coupling agent used for surface functionalization. APTES has three hydrolysable ethoxy groups that attach to the metal nanoparticle surface (known as silanization process) and the amine (NH_2) from the aminopropyl groups (pointing away from the surface) for further functionalization[141]. APTES has been extensively studied, and it has been reported that the orientation and attachment of APTES on surfaces depend on temperature, humidity, concentration of APTES and deposition time[142]. To achieve NH_2 groups as the interface between APTES molecule and nanoparticles is a major issue in silanization processes. During the self-assembly process, terminal amine(NH_2) can be folded to form hydrogen bonds with free silanol groups, which leads to multilayer deposition of APTES molecules[123]. Thus, NH_2-terminated APTES deposition on any substrate is extremely important for further surface modification. It is possible attach to form films of silver nanoparticles by functionalize them with PVP and ascorbic acid[143] the film formation does not require specialized equipment for their preparation for this reason are well suited in nanotechnology because are easy to prepare in figure 4 I have reported a typical scheme that resume the whole process.

In this work I used both methods (PVP an Silanization) to study morphological properties of silver nanoparticles, and to functionalize proper substrate to develop plasmonic sensors.

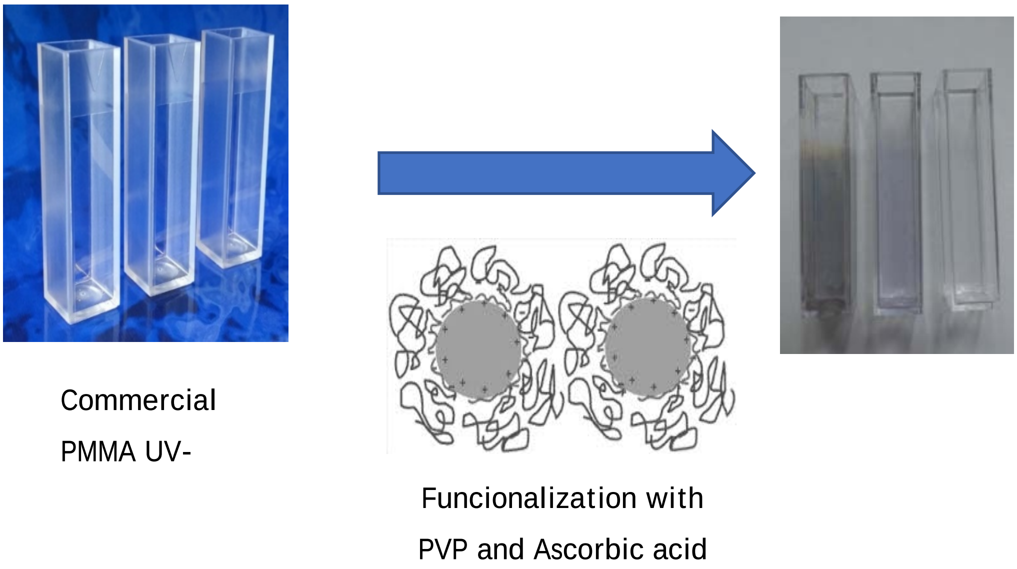

Figure 4: Grafting the inner walls of PMMA with silver nanoparticles

4.2 Paving PMMA cuvettes and plasmon sensing applications

In this section it will be shown how to fabricate a simple, reusable, and low cost plasmonic label-free sensor by paving the inner walls of PMMA cuvettes with silver nanoparticles (PVP method). The sensitivity of the NIR dipole plasmonic transition has been evaluated in the “as prepared” colloids as well as after the fabrication of the paved cuvettes. We have found that the plasmonic resonance has a smaller variation for the paved devices. However, advantages in using the paved cuvettes are in their reusability and their reliability in environments usually avoided for colloids, as with high ionic strength thus giving higher reproducibility in the detection of refractive index changes in the medium. These results open scenarios for further advanced engineered functionalization, as with molecular recognition agents.

4.2.1 Experimental procedure

Briefly silver nanoparticles were synthetized through Seed Mediated Growth method with the following agents:

Silver nitrate ($AgNO_3$, 99.9%), tri-sodium citrate (TSC, 99%), sodium borohydride ($NaBH_4$, 99%), hydrated hydrazine ($N_2H_4{\cdot}{}_2H_2O$ 50–60%), D-Sucrose (99.5%), Polyvinylpyrrolidone (PVP $(C_6H_9NO)_n$ wt. 360.000) and Ascorbic Acid (AA $C_6H_8O_6$ 99%) were purchased from Sigma-Aldrich and used as received without further treatment. To carry out the whole synthesis deionized water (>18.4 MΩ·cm) was used in all the synthesis processes. To carry out our results we used UV–vis-NIR spectra in the region from 300 nm to 1100 nm were obtained by a Cary 60 spectrometer by Agilent Technologies, Atomic Force Microscopy (AFM) images were obtained in alternate contact mode with a force modulation tip, by using a Witech Alpha 300 RS, Scaning Electron Microscopy (SEM) images were acquired using a ZEISS SUPRA 55 VP FE-SEM, and ImageJ was used to elaborate electron microscopy images. Boundary Element Method simulations were performed with the MNPBEM17 Matlab toolbox, using Matlab R2019b.

4.2.2 Results and discussions

The seed-mediated synthetic approach allows close control over the shape and size of the nanoparticles with simple variations of the experimental conditions[144]. Two different samples were synthesized with main plasmon resonances centered at around 600 and 800 nm (from here referred to as #600 and #800 samples, Fig. 5a). The most intense extinction band in each colloid can be attributed to a dipole in-plane oscillation, whereas other bands of minor intensities can be ascribed to out of the plane (below 400 nm) and in-plane multipole resonances[117]. Each "as prepared" colloid was characterized by SEM, (Fig. 5 b,c) and AFM (Fig. 6). SEM images reported in the inset of Fig. 5b and 5c show a variety of different shapes, from triangles (with variable rounded vertices) to hexagons. In particular, the sample with the main resonance at 600 nm presents a nanoparticles (NPTs) size distribution with Feret diameters, namely the maximum hindrance, centered at 70 nm. Instead, the sample with the main resonance at 800 nm shows a bimodal size distribution centered at 40 nm, related to the smaller nanoparticles and 130 nm related to the bigger and triangular structures.

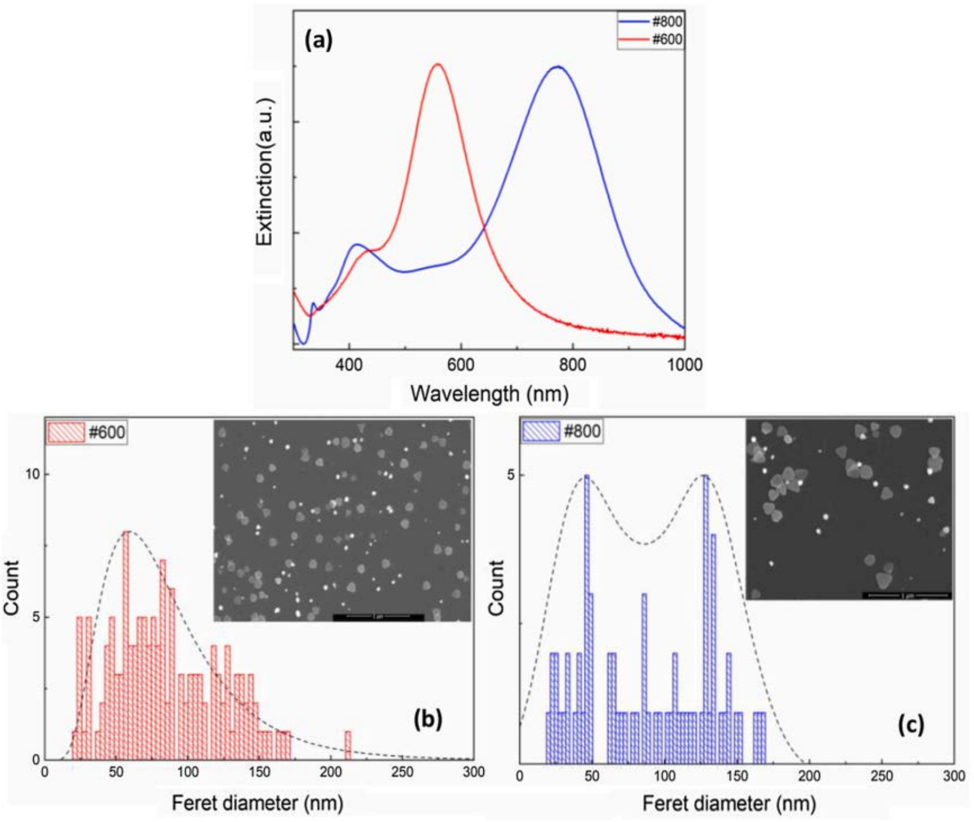

Fig. 5. Plasmon resonance extinction spectra for #600 and #800 colloids (a). Distribution of Feret diameters obtained by the SEM analysis of Ag NPTs with resonances at 600 nm (b) and 800 nm (c). The insets report the SEM images for the two samples.

The AFM images reported in Fig. 6a and 6b agree with the SEM analysis. Moreover a section analysis (Fig. 6c) shows that the thickness of the nanoplates lies between 8 and 10 nm for both samples. The morphological data were used to build-up six models (NPT1-3 for #600 and NPT4-6 for #800) for the simulation of the extinction spectrum by Boundary Element Method calculations [see references in chapter 2 in the section of BEM simulations]. Each set of these modeled NPTs has been chosen according to SEM and AFM observations.

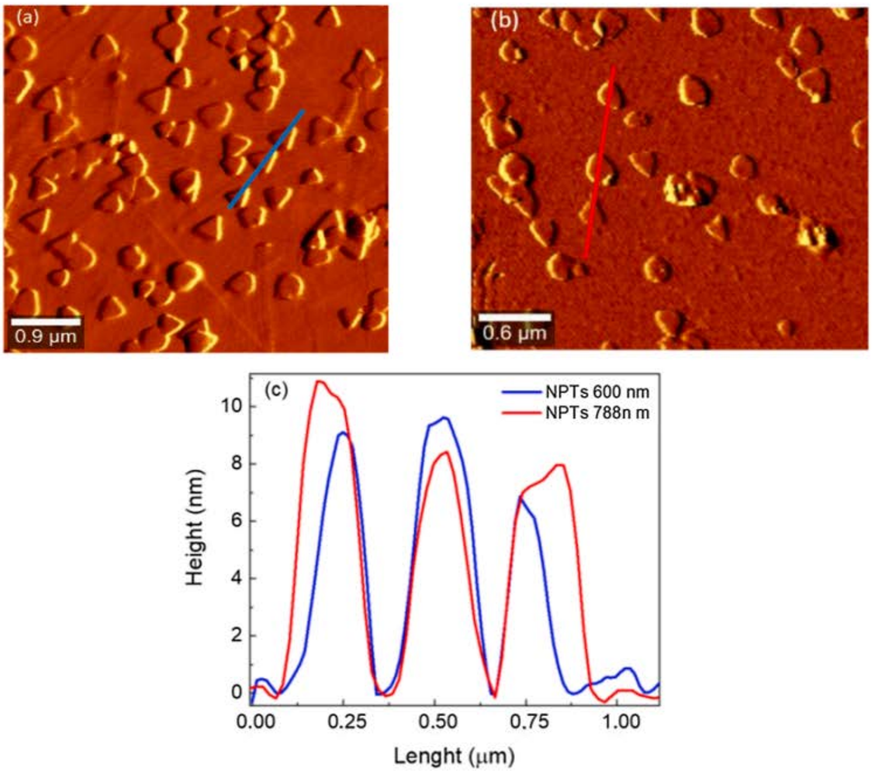

Fig. 6. AFM images of Ag NPTs #600 (a) and #800 (b). Section profiles are reported in (c).

The calculated extinction spectra are reported in Fig. 7a and 7b and their convolution shows a good agreement with the experimental findings. In addition to the parameters discussed above, the calculated data suggest that the position of the dipole in-plane resonance depends on the geometrical features of the NPTs. Sharper tips, as well as bigger particles, or particles with an higher aspect ratio (ratio between Feret diameter and thickness), have the main resonance at higher wavelengths. One also notes that the #800 sample does not present any significant contribution from the fraction of smaller NPTs with Ferret diameters of about 40 nm (Fig. 5c) because of their lower extinction cross-section (Fig. 7c, d), with respect to bigger NPTs. The deposition of a homogeneous layer of preformed plasmonic nanoparticles onto a defined surface is a delicate task if the plasmon features observed in the colloidal form must be preserved. It is necessary to ensure a certain distance among the deposited nanoparticles to avoid plasmon coupling which modifies the plasmon resonances observed for the colloids. At the same time, the layer should be able to give a good signal/noise ratio in the extinction spectrum. In this frame, it was reported that a PMMA surface is particularly suitable for monolayer deposition of silver nanoparticles surrounded by a PVP shell[145]. For this reason, among the commercially available cuvettes for VIS-NIR absorption spectroscopy, we have considered those made of PMMA.

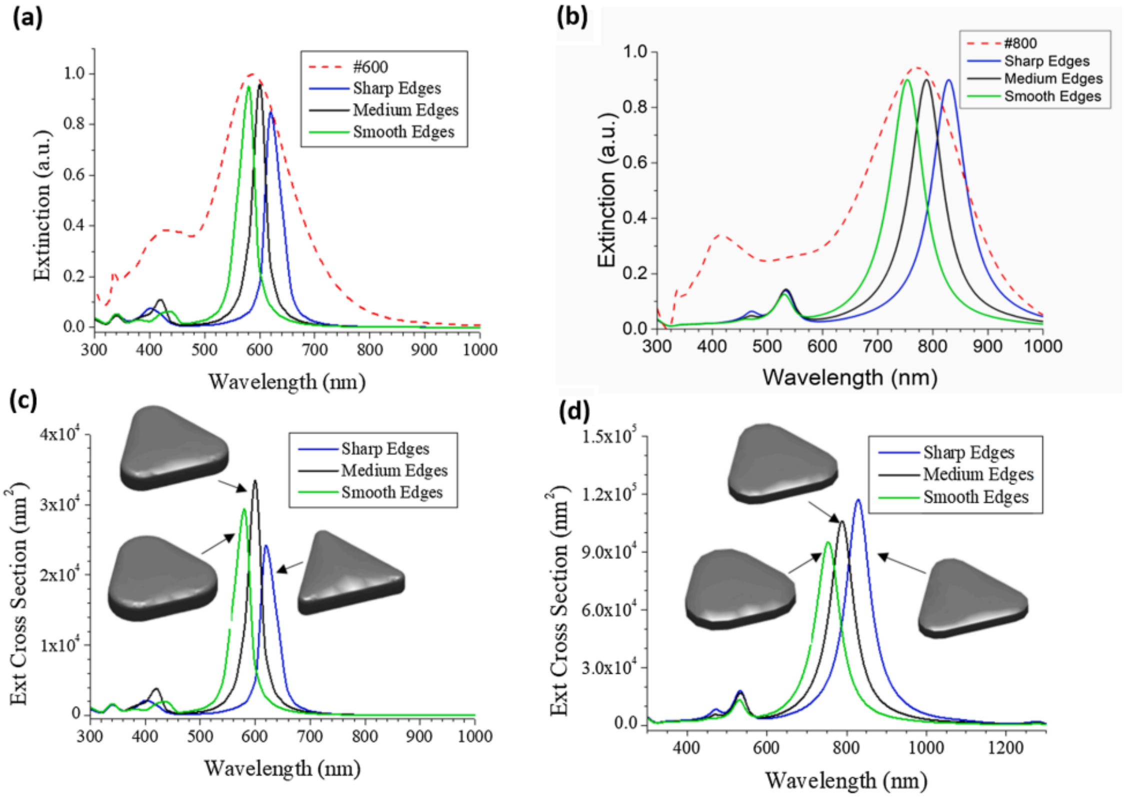

Fig. 7. (a) and (b), the experimental spectra for the #600 and #800 samples are normalized and superimposed with the ones obtained by BEM simulations of silver nanotriangles with edges and thickens dimension coherent with the TEM and AFM measures, but with different tips roundness the calculated optical extinction cross-sections show that, as expected, the three bigger particles in (d) have extinctions almost three times higher than those in (c).

The cuvette's pavement it was obtained by using 10 mL of PVP solution (2 mM MW 10000 Da) and 20 mL of Ag colloid added under strong stirring. Then, 3 mL of AA solution (100 mM) was added to this solution always under strong stirring for 10 min. The PMMA cuvettes, cleaned with water and dried with nitrogen, were filled with the final solution whose extinction in a 1 mm cuvette is 0.3. After 20 h, the cuvette was emptied, rinsed with water, and dried with nitrogen. Pavement efficiency has been optimized by using proper PVP and AA concentrations during the colloid synthesis. The method reported here is considered particularly efficient for many noble metal nanoparticles, regardless of their shape, and has been used in our case to pave cuvettes also with spherical silver nanoparticles. Fig. 8a compares the extinction spectra of the two as prepared colloids (solid lines) with those of the corresponding paved empty cuvettes (dotted lines). One can see that the functionalized cuvette spectra are significantly blue shifted. This can be understood considering that the NPTs in the colloidal suspension are surrounded by water, whereas a particle on top of a PMMA surface has two different boundaries with distinct refractive indices: PMMA (n = 1.49) and air (n = 1). Fig. 8 (b) shows a picture in which we compare an "as received" (right) and a functionalized (left) cuvette.

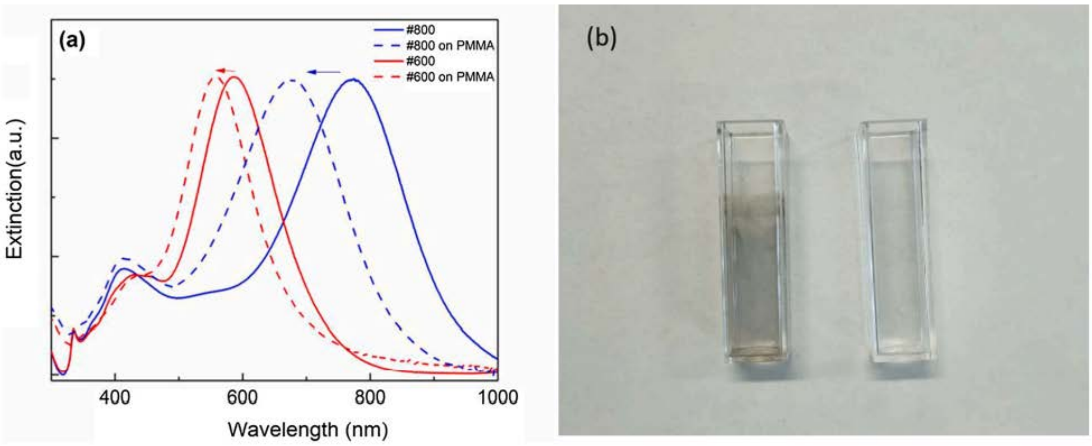

Fig.8. (a) Comparison between the extinction spectra of the as-prepared colloids (full lines) and those of the corresponding paved empty cuvette (dashed lines). (b) Image of the paved cuvettes (left) compared with an "as-received" one (right).

The plasmon features of the paved cuvettes are quite stable, even after ten cycles of water and tert-butanol liquid exchange, as reported in Fig. 9. In this case water and tert-butanol have been selected because they have strongly different polarities (0.39 for tert-butanol with respect to water). Although the different polarities might have favored particle detaching, the spectra intensities and the positions of the main resonance peak are unchanged after the test, confirming the optimal stability of the deposited particles. The high stability of the deposited nanoparticles opens up the possibility to reuse the device for several refractive index measurements. Up to now, the detection of refractive index variation of an analyte through the shift of LSPR, using a transmittance configuration, has been pursued with disposable devices. Commonly, drops of a metallic nanoparticle colloid are added directly to the solution to be analysed, thus contaminating the sample, and making it unusable for further analysis. Moreover, the waste of metal nanoparticles is neither economically nor environmentally sustainable. Conversely, our new LSPR device demonstrates a high stability without any detachment of nanoparticles, as demonstrated by Fig. 9(b). This high stability ensures the integrity of the analysed sample (from particles contaminations) and provides a reusable device instead of disposable metal nanoparticles solutions. This type of analysis is fast as well as economically and environmentally sustainable.

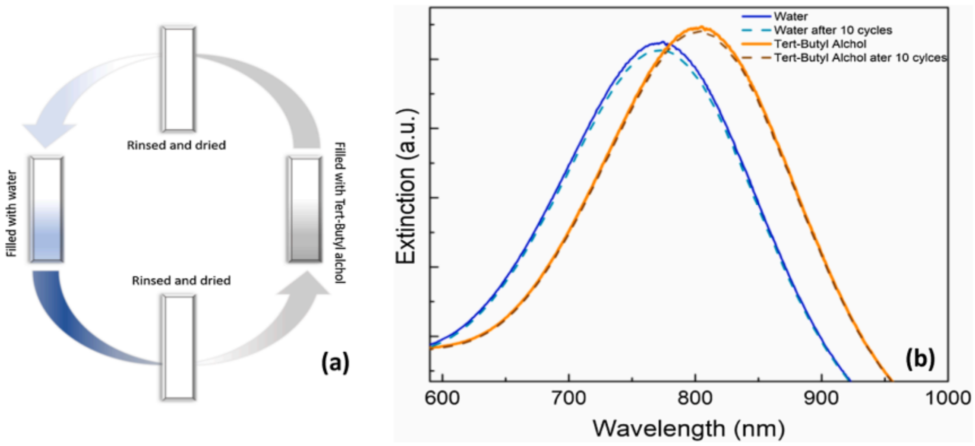

Fig. 9. (a) Schematic representation of the stability test for the paved cuvette carried out in water and tert-butyl alcohol. The cycle was repeated ten times. (b) Absorption spectra for sample #800 before and after the stability test.

The DRS is defined as the variation of the plasmon resonance position (λ_{LSPR}) with the average relative refractive index (n):

$$DRS = \frac{d\lambda_{LSPR}}{dn}$$

To determine sensitivity values of silver nanoplates in water (n = 1.33) the refractive index, surrounding the plates in suspension, has been varied up to 1.42, by adding different aliquots of a sucrose solution. DRS values of 342 nm/ RIU (refractive index units) and 457 nm/RIU are found for the #600 and #800 colloids, respectively. The results are shown in Fig. 10 as full dots. These values agree with those reported in literature, even higher in the case of #800. Differently shaped noble metal NPs (spherical, cubic, pyramidal) has also been also studied by H.Chen et al., with results in the range between 44 and 390 nm/RIU.

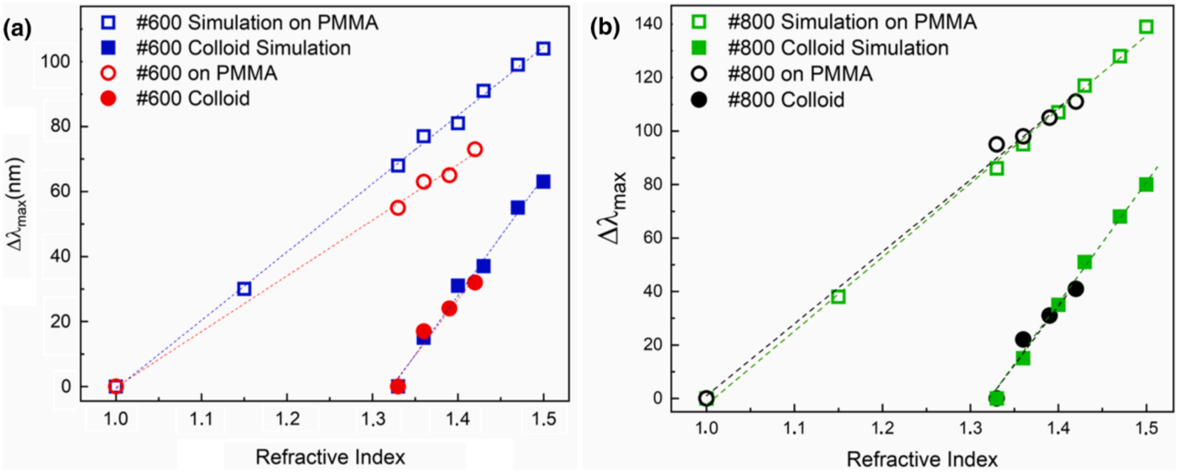

Fig. 10. Refractive index changes response curves for the #600 (a) and #800 (b) samples. The full symbols are referred to the particles as colloid dispersion, while the empty symbols to the paved PMMA cuvettes. BEM simulations (squares) confirm the trend observed in the experiments (circles).

The same Fig. 10 reports some measurements performed after paving the inner walls of a PMMA cuvette with the #600 and #800 colloids (empty dots). In this case DRS values of 171 nm/RIU and 269 nm/RIU have been obtained. We observe larger DRS for plasmonic resonances in the NIR region, i.e. the #800 sample. It is important to observe that the DRS values measured for the colloids are almost doubled than those obtained for the paved cuvettes. However, advantages in using the paved cuvettes are in their reusability and their reliability in environments usually avoided for colloids, as with high ionic strength thus giving higher reproducibility in the detection of refractive index changes in the medium. The Limit of Detections(LOD) for the cuvettes, paved with the #600 and #800 colloids, were calculated according to Loock et al[146]. Three cuvettes were paved, for each colloid, and measured independently. Each cuvette was filled with water and the position of the dipole plasmon bands recorded and stored as the “zero reference”. The center of a Gaussian curve fit was used as the band position. Then, each cuvette was emptied and re-filled with water three more times and the position of the dipole plasmon bands measured in respect of the relative “zero reference”. As a result, three independently paved cuvettes were measured three times for each of the #600 and #800 colloidal batch. The LOD is therefore calculated according to equation (1):

$$LOD[RIU] = 1.33 + \frac{3s_{\Delta\lambda}}{r}$$

Where $S_{\Delta\lambda}$ (0.823 nm for #600 sample and 0.802 nm for #800 sample) is the standard deviation for the relative position of the dipole plasmon band in respect of the “zero reference” for each of the three measures of the three independent cuvettes (i.e. 9 measures for each colloid). r is the slope of the calibration curves in Fig. 10 (171 nm/RIU for #600 sample and 269 nm/RIU for #800 sample). Paved cuvettes filled with water (RIU = 1.33) were considered as the blank. The LOD calculated for both the #600 and #800 nm samples are 1.34 RIU. BEM calculations help in understanding the correlation between the experimental results and the nanoparticle features. Simulations were performed with the geometries NPT#2 and NPT#5 used for the calculations of the #600 and #800 samples spectra reported in Fig. 5. The extinction spectra were calculated for the nanoplates embedded into a homogeneous environment, with refractive indices from 1.33 (pure water) to 1.5, and for the nanoplates leaning on a PMMA surface (n = 1.49) and surrounded by an environment with the same variation of the refractive index. The case with n = 1 was also considered (empty cuvettes). We found that the interface between the particle and the PMMA surface could influence the DRS that is lower than in the case of colloids. The relative band positions (Δλ, in respect of the empty cuvette or of water in case of a colloid), plotted against the solvent refractive index, are in strong agreement with the experimental data, confirming that the PMMA surface is the main cause for the DRS reduction. The simulations well reproduce the experimental data, confirming that these plasmonic systems are excellent sensors for a refractive index variation of the surrounding environment. As previously mentioned, DRSs for the colloidal state are higher (higher slope of the curves in Fig. 10) than those of the corresponding paved cuvette. This derives from the exposure of all the faces of the NPTs to the environmental solution when NPTs are dispersed as a colloid. A lower DRS value for the paved cuvettes could be misunderstood as a disadvantage for plasmon sensing applications with respect to the colloidal solution. However, paved cuvettes are certainly a kind of devices that can be used for a wide range of liquids and solutions. For instance, solutions with a large variety of ionic strength can be considered using the present device, since no severe aggregation phenomena can occur between the metallic nano-objects, which could alter the dipole peak positions. Moreover, the analyzed solution could be used for further analysis because the NPTs does not detach from the surface of the cuvettes not contaminating the sample.

4.3 Paved glass cuvettes for plasmon biosensing applications

Diagnostic tests and analytical procedures are in high demand and biosensors are at the frontline of analytical approaches. Biosensors are diagnostic tools that comprise a biosensing component and a transducer. The sensing substance, ie, the biorecognition element, can comprise of enzymes, antibodies, bacteria, tissues, organelles, DNA and RNA. These components create digital electrical signals in response to biomolecular interaction enabling labeled as well as “label-free” analyte detection[147]. Generally speaking biosensors have many advantages that are affordability, convenience, rapid response, good sensitivity as well as specificity over larger traditional instrument-dependent technologies. Surface plasmon resonance (SPR) refers to an optical phenomenon that can be used in quantifying molecular bonding in real-time and in a label-free manner. Historically speaking SPR was first demonstrated as an optical biosensor by Liedberg and Nylander in 1982. Fundamental bio-monitory studies, research in medical sciences, drug development, clinical diagnostics, even environmental and agricultural monitoring all have benefited from the usage of SPR biosensors[148,149]. Plasmonic nanomaterials (P-NMs) are the basis of nano-plasmonic biosensors. Metallic nanoparticles like gold, silver, platinum, and carbon nanotubes have been developed. Hybrid plasmonic nanomaterials, such as bimetal nanoparticles, core–shell MNP, and MNP-enhanced carbon nanotubes (MNP-CNT) have been designed to obtain an improved plasmonic effect. The overall specificity of localized detection and point-of-care diagnosis platforms has increased because of P-NMs[150,151]. In this section we will talk about the development of plasmonic label free biosensor based on same studies did in the section the paved cuvettes, but using glass cuvettes instead of PMMA cuvettes due to their low resistance solvent. To demonstrate the biosensing capability of our paved cuvettes we have taking into account to use one of the most famous case of study that is the biological interaction between biotin and avidin. Avidin is a basic tetrameric glycoprotein composed of four identical subunits, each binds to biotin with high specificity and affinity (K_d $\sim 10^{-15}$ M). Therefore, the avidin-biotin interaction serves as a great tool in the biomedical and nanotechnological applications. On the other hand, biotin-based conjugates are easy to synthesize and have less impact on the activity of the biomolecules. In this work we have studied paving process through silanization, studied the morphological properties of the paved glass cuvettes to carry out the surface density of our system and basing on this data we have calculated the number of biotin molecule per particles, then we have bound biotin onto the surface of our paved glass cuvettes, studied the plasmon response in the presence of different concentrations of avidin ranging from ($3x10^{-8}$ M) to (10^{-5}M) by reporting the limit of detection of our systems, and we have supported our data with numerical simulations.

4.3.1 Experimental procedure

Silver nitrate ($AgNO_3$, 99.9%), tri-sodium citrate (TSC, 99%), sodium borohydride ($NaBH_4$, 99%), hydrated hydrazine ($N_2H_4{\cdot}{}_2H_2O$ 50–60%), D-Sucrose (99.5%), Avidin from Egg White, (+)- Biotin N-hydroxysuccinimide ester (98%), Cysteamine (95%) and N,N-Dimethylformamide were purchased from Sigma-Aldrich and used as received without further treatment. To carry out the whole synthesis deionized water (>18.4 MΩ·cm) was used in all the synthesis processes.

To carry out our results we used UV–vis-NIR spectra in the region from 300 nm to 1100 nm were obtained by a Cary 60 spectrometer by Agilent Technologies, Atomic Force Microscopy (AFM) images were obtained in alternate contact mode with a force modulation tip, by using a Witech Alpha 300 RS, Scaning Electron Microscopy (SEM) images were acquired using a ZEISS SUPRA 55 VP FE-SEM, and ImageJ was used to elaborate electron microscopy images. Boundary Element Method simulations were performed with the MNPBEM17 Matlab toolbox, using Matlab R2019b.

To pave glass cuvette with silver nanoparticles we used silanization process. In particular the surface of the glass cuvettes needs to be activated and the activation process was carried out through an inverse piranha solution. The solution is formed with oxygen water (H_2O_2) and sulfuric acid (H_2SO_4) with ratio 3:1. So the glass cuvettes are filled with piranha solution and put on a hot plate for an hour with temperature of 90°C. Activation process consist in the formation of hydroxyl groups on glass surface as shown in the figure 11 below

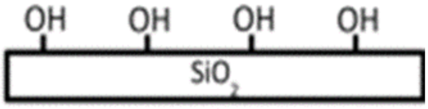

Figure 11: Activated silica surface

At the end of piranha treatment, the glass cuvettes were washed rapidly with a sodium hydroxide solution, after that washed with abundant deionized water and rinsed with nitrogen flux. After the activation process the glass cuvettes were filled with 1% v/v in of APTES in H_2O solution for 5 hours. At the end of the process the substrates were rinsed, dried and to verify the efficiency of the process they were carried out measurements of water contact angle.

4.3.2 Results and discussion

Contact angle is a measure that describes and determine the ability of a solid substrate to repel a liquid. They can be used to detect the presence of films, coatings, or similar contaminants, which have a surface energy that is different from the substrate. The detection capability of this method is directly related to the difference in their relative surface energies. In the simplest case, the hydrophobicity (water-repellent property) of the substrate is tested by setting a drop of water on the substrate surface. With increasing contact angles against a certain liquid, the property of the substrate to repel this liquid is also increased. In the case of water as testing liquid, substrates with a contact angle of >90° are considered to be hydrophobic, or in other words water-repellent. To verify silanization process we have carried out a study of the water contact angle during the whole process. So the first measurement was carried out after the activation process as reported in figure 12

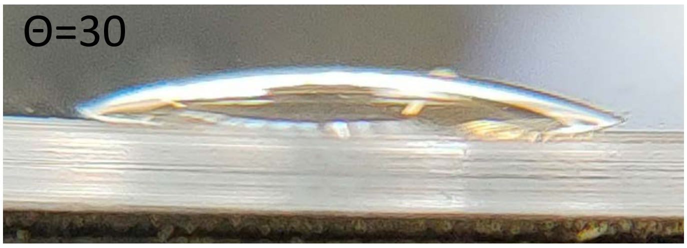

Figure 12: Contact angle measurement after the activation process

The sample has a value of contact angle of 30°, and this value is representative because the surface after the activation process is rich of hydroxyl group. Hydroxyl groups possess a good degree of interaction with water. The second angle contact measurements were carried out after the silanization process, and in the figure 13 is shown that the contact angle is almost doubled.

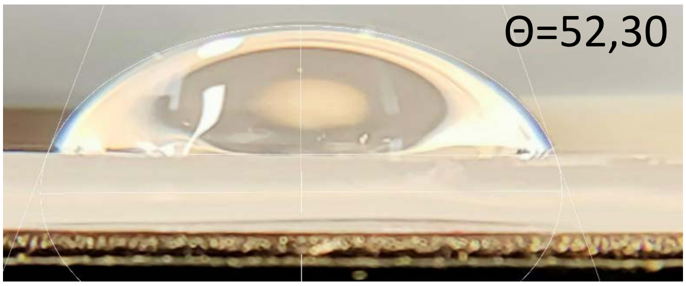

Figure 13: Contact angle measurement after silanization process

Contact angle values depends mainly on two factors:

1. Functionalization time
2. Concentration of APTES solution

To study the influence of both parameters, we have prepared two solution of APTES with different concentrations (1% and 2,5%) and we have monitored the variation of contact angle measurements at different functionalization time in a arc of time between 15 minutes to 24 hours as shown in the figure 14

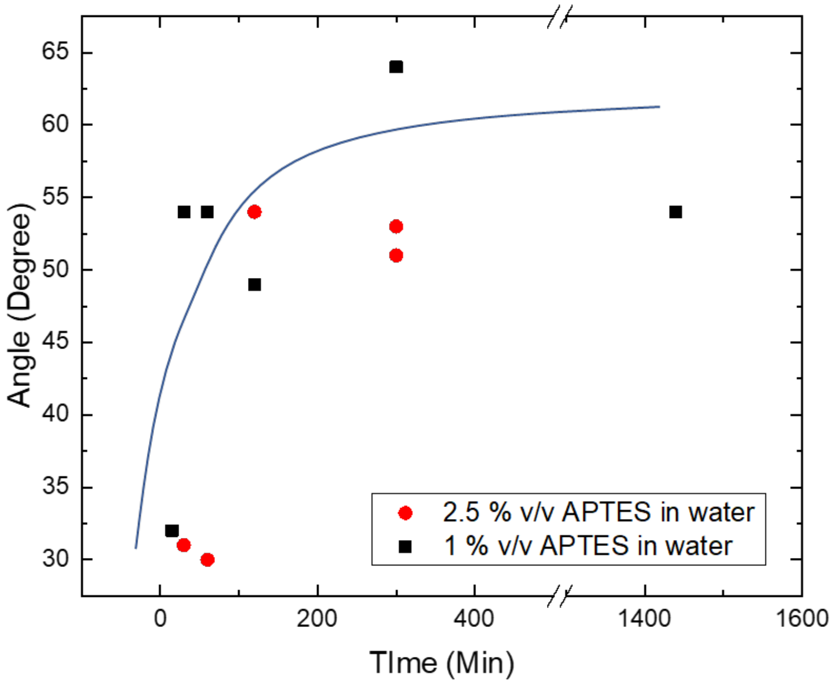

Figure 14: Contact angle degree as a function of time at two different APTES concentrations

From the figure is possible to verify that contact angle value is independent from the concentration and above all is strictly dependent from functionalization time. After one hundred minutes contact angle value does not change, the only explanation to this behaviour is due to the fact that the surface reaches the high degree of APTES molecules coverage. Even with this parametric study the only thing that remains unexplained is the contact angle out of the average values of 50°. To comprehend the meaning behind that value (corresponding to 60°, see the figure) we have to see APTES molecules geometry on to the surface of generically silanized substrate. So, to explain this difference in terms of contact angle value scientist have supposed four different type of interface between APTES molecules and surface that can be formed during the process as shown in the figure 15

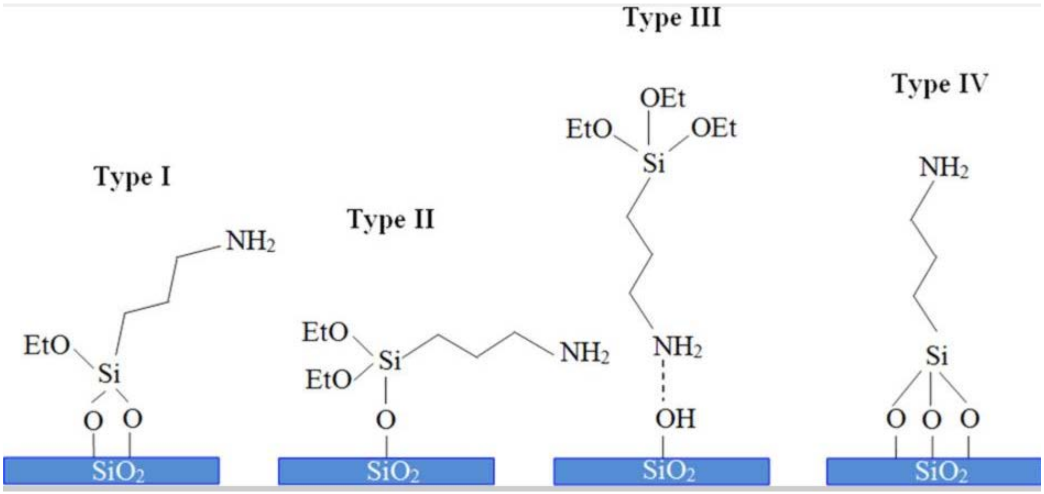

Figure 15: Four types of interfaces glass cuvette APTES[152]

In the figure 15 we have four types of interfaces[153,154] formed during the process and respectively are:

- Type I) Two ethoxy group bonded to the surface.
- Type II) One ethoxy group bonded to the surface.
- Type III) Hydrogen bond is formed between -NH_2 terminal group and -OH from hydroxylated glass substrate.
- Type IV) Corresponding to each ethoxy group bonded to the surface.

In the presence of configuration, I and II free ethoxy group can react with other free ethoxy group by creating cross-linking of APTES molecules and in the worst rare scenario can cross-link with -NH_2 free terminal group. Cross-linking with -NH_2 group lowers the deposition efficiency of our silver nanoparticles onto substrates because free amine group are capable to interacts electrostatically with silver nanoparticles. In the type III scenario silver nanoparticle, they cannot interact with the surface due to the absence of free amine terminal group and as a result it cannot be possible pave the surface. In the ideal case (type IV) the paving efficiency is maximized due to the absence of free ethoxy group. These possible configurations of APTES molecules on the surface play a key role regarding the wetting properties of the substrate. This is the reason why contact angle measurements are a powerful instrument to understand the success of silanization process. In literature is reported a study that relates the APTES configurations with water contact value as reported in the figure16.

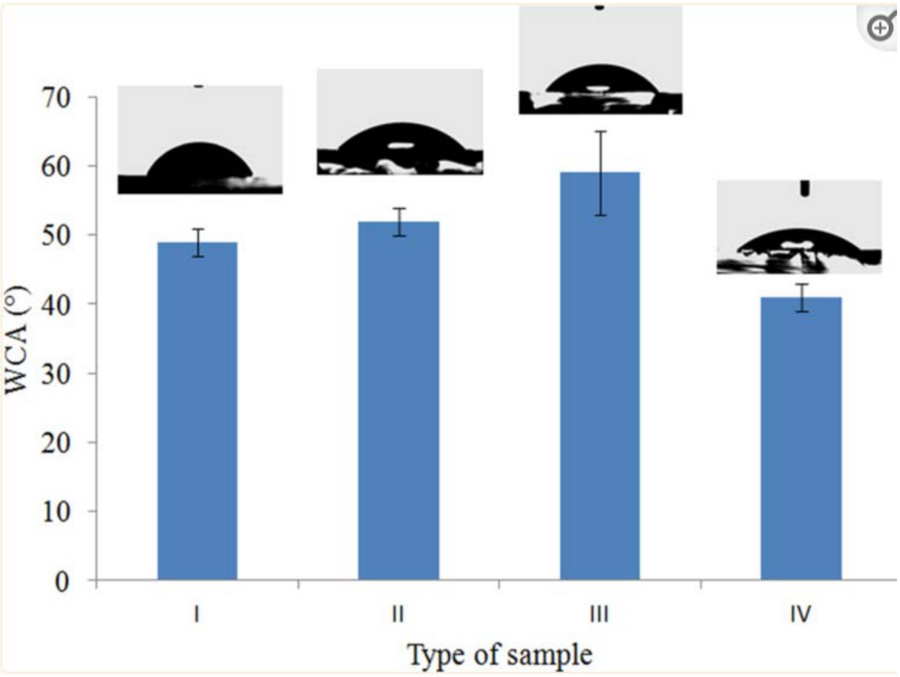

Figure 16: Water contact angle in relation to the configuration type[152]

In the figure 16 are reported the measurements between water contact angle between water and silanized surface. Basing on the configuration type are observed four type of wetting properties corresponding to a specific value of contact angle. So for the type IV, corresponding to the ideal scenario, contact angle value is 41° due to the precence of only free amine hydrophilc group. Configuration I and II possess respectively contact values of 49° and 52° that are higher than configuration I due to ethoxy free group. More are free ethoxy groups more higher are contact values angle. Due to to this beaviour configuration III possess the highest contact values which correspond to 59°. So, considering the parametric studied carried out by the group of H.Kiaw et Hal now we are able to identify the reason of the value of contact angle out of the average shown in the figure 16 and the configuration of our substrates is corresponding to the type 2 because our average contact angle is corresponding to 52° which is the same value reported in the parametric study reported from the literature. Paving process was carried out by filling the silanized glass cuvette with SMG synthetized silver nanoplates, having plasmon resonance at 750 in colloidal state and maintaining the colloid for two hours into the glass cuvette. After 2 hours the glass cuvette was rinsed and dried and then spectra measurement was carried out to evaluate the correct transfer of silver nanoparticles plasmon properties onto the wall of the silanized glass cuvette as shown in the figure 17

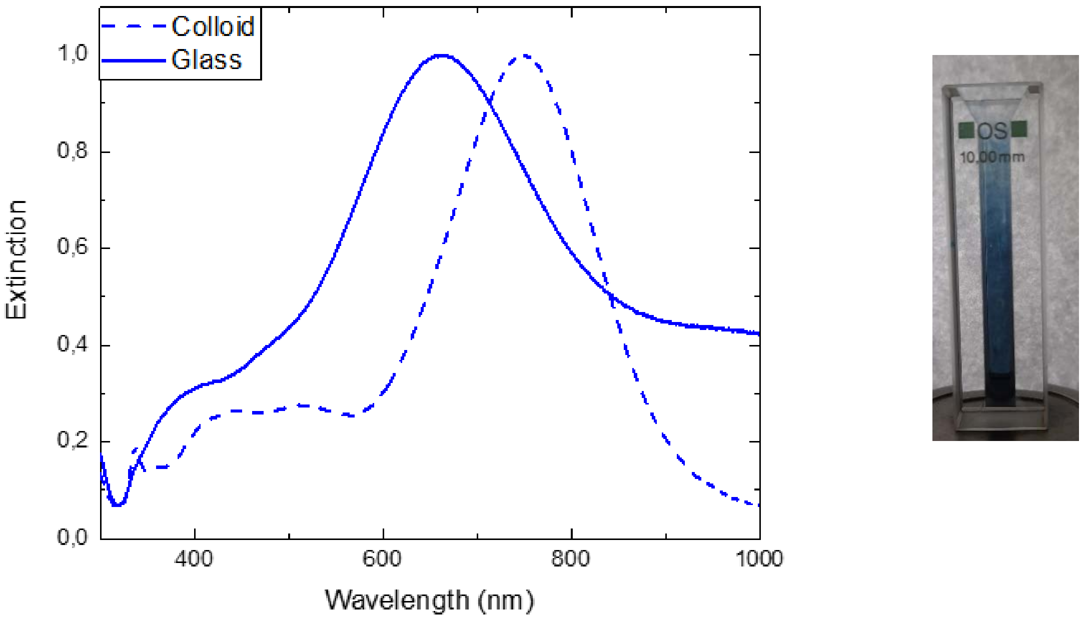

Figure 17: a) blue shift of the main plasmon peak due to the transfer of silver nanoparticles onto the glass cuvette b) glass paved cuvette

In the figure 17 we compare the extinction spectra of the as prepared colloid (solid lines) with the corresponding paved empty cuvette (dotted lines). So, in the same way as seen in the section of the paved PMMA cuvettes functionalized cuvette spectra are significantly blue shifted and this can be explained by considering that the NPTs in the colloidal suspension are surrounded by water, whereas a particle on top of a glass surface has two different boundaries with distinct refractive indices: glass (n = 1.5) and air (n = 1). In the figure 17b is shown the result of silanization paving process. To develop our biosensor device, we evaluated the the particles density through AFM measurements. Due to mechanical difficulties to carry out AFM measurements inside the glass paved cuvette we have paved a glass microscope slide with the same silver nanoplates batch used for the cuvette and with the same parameters in order to calculate surface density data and to study the morphology of silver nanoplates deposited onto the glass slide surface. In the figure 18a is shown AFM images and a section of a single nanoparticles 18b.

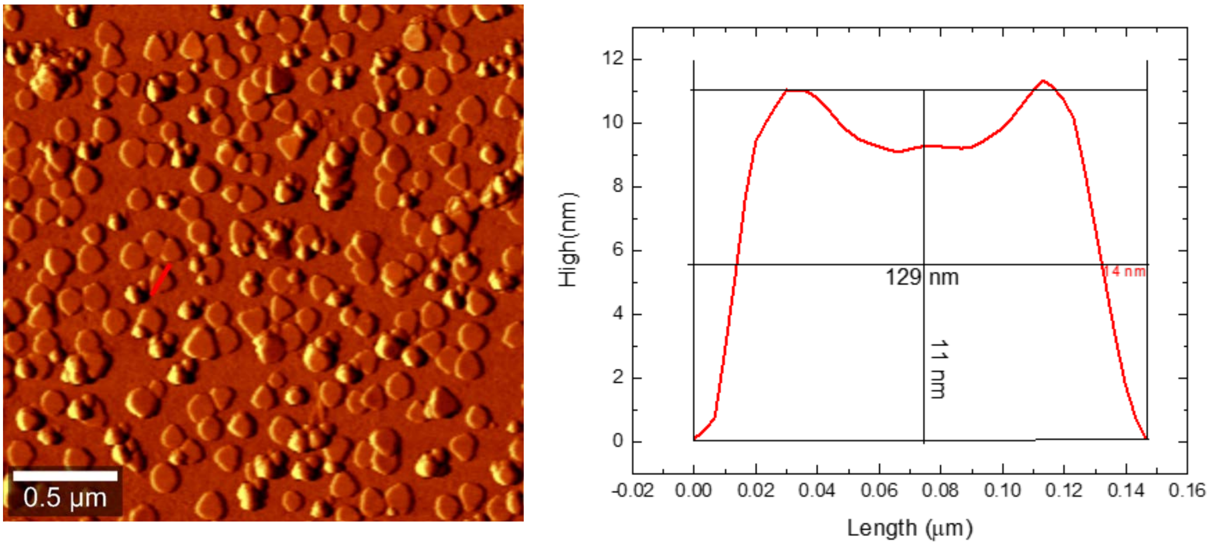

Figure 18: a) AFM images of paved glass slide b) Section of a silver nanoprisms

From the section in (figure 18 b) we have established that the nanoparticles average size is 129 nm and average thickness is 11 nm. By considering the number of nanoparticles constant in the whole functionalized area of the glass slide, corresponding to 25 mm x 25 mm, we have calculated the particles number in the whole pave glass slide area and the number of particles in a surface of 1m^2. In the table below are reported the values.

Surface	**Particles number for surface unity**
25x25 mm (glass)	2,45 X 10^{10}
1 m^2	3,92 X 10^{13}

From now on we consider the values reported in the table the same for our glass paved cuvette and we can possibly consider the same density values because we have used the same nanoparticles used for the pavement of both glass slide and glass cuvette. So, in order to calculate the maximum number molecule of cysteamine that can directly interact with the silver nanoplate anchored onto the glass cuvette, we used the density values and the maximum number of cysteamine molecules adsorbed by a single nanoparticle. We have found a work in literature done by the group of Amanda J. et al[155] in which is reported that for a plate of average size of 100 nm the cysteamine molecules number adsorbed for a single particles is equal to 6x10^4 molecules. So, we have calculated by using the particles density value in 2,5 cm^2 and using the data reported from the literature (6x10^4 molecules of cysteamine for single particles) that the maximum molecules number of cysteamine is equal to1,6x10^{14} molecules/cm^2. Knowing the number of cysteamine is fundamental because thanks to that value we could calculate the concentration of cysteamine needed to link biotin to the silver nanoplates. In order to carry out biotinylating process we have conducted the whole process in anhydrous N,N-Dimethylformamide because water molecules cannot allow the interaction between Cysteamine and Biotin see figure 19b below. To attach Cysteamine onto the surface we have filled our glass cuvette with a solution of Cysteamine 1,42mM for four hours, then rinsed the glass cuvette with N, N-Dimethylformamide in a controlled environment. After that we have filled the glass cuvette with a biotin solution 9,8mM for 12 hours. At the end of the process, we have rinsed the glass biotinylating cuvette with deionized water and dried with N_2 flux and then keep in a vacuum oven for thirty minutes at 40°C. The vacuum step is fundamental to remove any traces of N, N-Dimethylformamide from the surface of glass biotinylating cuvette in order to measure the main plasmon peak shift after the whole process as shown in the figure 19a

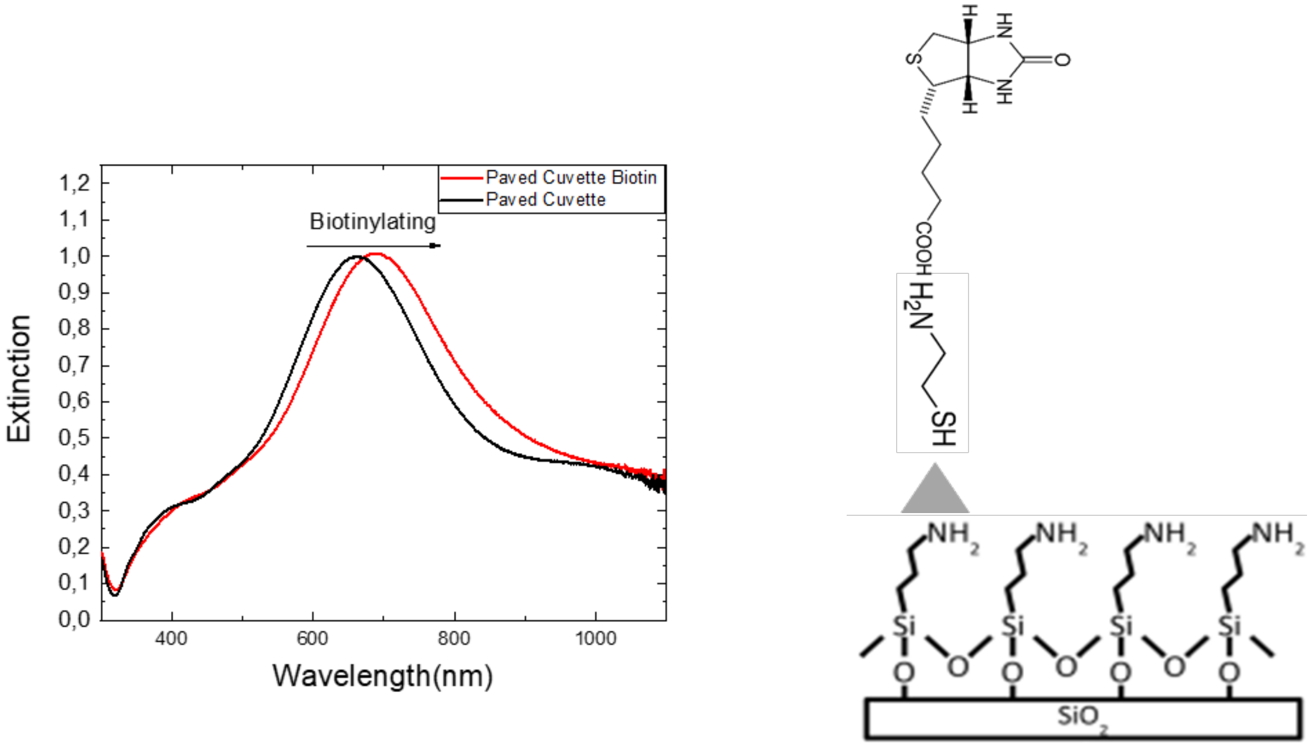

Figure 19:a) Red shift of main plasmon resonance peak due to biotinylating process b) Molecular scheme of biotinylated glass paved cuvette

We have carried out plasmon resonance spectra after biotinylating process, and as we can see from the figure 19 the main plasmon resonance is red shifted in respect of main plasmon resonance of the glass cuvette this shift is equal to 27nm. There is only one explanation to this red shift and is related to molecular linking of biotin on to the surface of silver nanoplates. So at start of the process the main plasmon resonance peak had initial value of 662nm at the end of biotinylating process the main plasmon peak has assumed the value of 689 nm. Now the sensor is ready to use and to carry out the measurements we have filled the sensor by using different concentrations of avidin starting from the lowest one that corresponds to $1x10^{-8}$ M. We have worked with a of Avidin concentration interval ranging from $1x10^{-8}$ M to $1x10^{-5}$ M. For each measurement we have filled the sensor with different

Avidin concentrations starting with the lowest one as said before and then keep the solution into the cuvette for two hours then rinsing with water then dried with N_2 flux and then keep the sensor into vacuum oven for thirty minutes at 40°C as said before the vacuum step is fundamental in order to completely remove the water. The sensor is very sensitive to any environmental change and when we perform the measurements, we need to be sure that all water is removed in the figure 20 below is shown the biotin-avidin sensor process treatment.

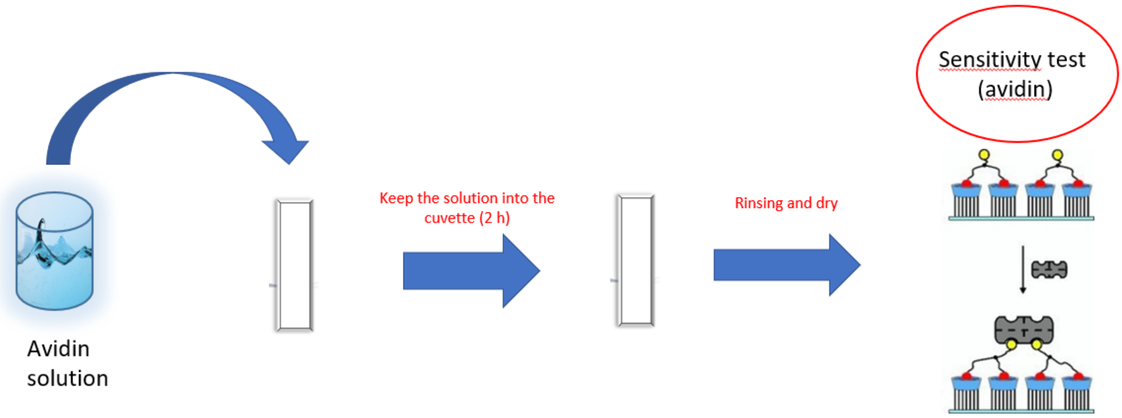

Figure 20: Schematic procedure of biotin avidin sensor process treatment

We have performed sensor measurements by maintaining avidin solution inside the sensor and by removing the solution as shown in the upper figure. So, in one case our silver nanoparticles as a boundary have water (n=1.33) and glass (n=1.55) in the other case have air (n=1) and glass (1.55). As shown in the figure 21a below the test sensitivity of Avidin with boundary air exhibit a total shift of main plasmon resonance peak of 70nm.

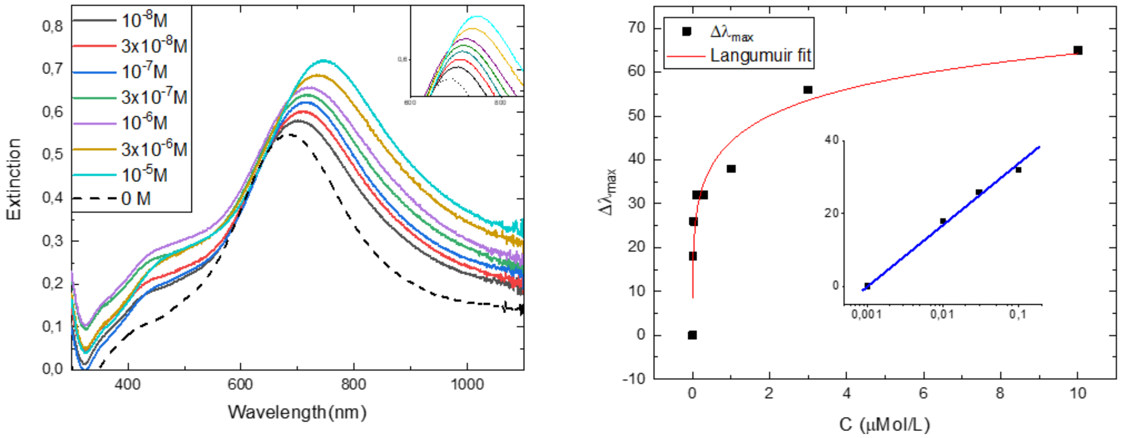

Figure 21: a) Sensitivity test (boundaries air) starting from the lowest concentration 10^{-8} to the higher concentration 10^{-5} b) Langmuir fit model with a caption representing the linearity interval of the fit function

In the figure 21b is reported the plasmon shift as a function of the concentration of avidin and the data are fitted with Langmuir fit model, which means that our sensor above concentrations of 10^{-5}M of avidin reaches the saturation. This behaviour can be explained in the same way as Langmuir isotherm absorption model. Briefly this model starts from the assumption that for every single site can be absorbed one molecule and the process can be reversible. In our case in the presence of saturation every single biotin site is occupied by one avidin molecule but due to their high affinity ($K_d \sim 10^{-15}$ M) the process is not reversible, nevertheless the Langmuir fits works and fully describe the whole situation. Sensitivity test having as a boundaries water are reported in the figure 22 below. In the case of water boundaries there is no sign of plasmon shift, probably there is no difference in refractive index between max protein concentrations at the surface and to verify these

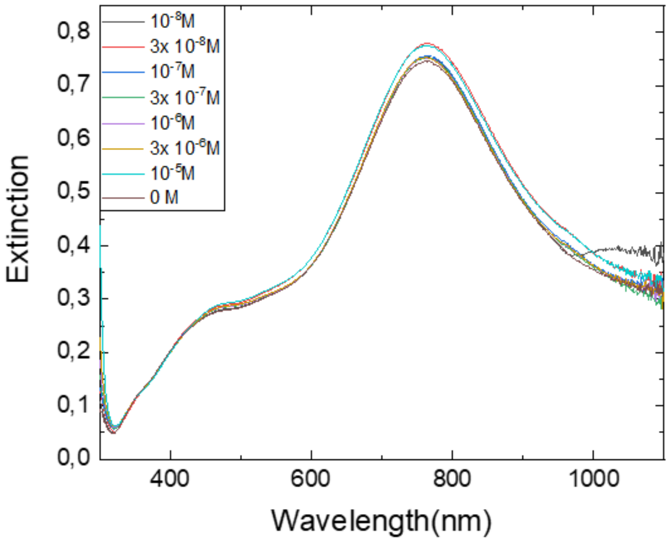

Figure 22: Sensitivity test with water boundaries

hypothesis were carried out numerical simulations that will be see later in this section. To carry out the Limit of detection (LOD) of the sensor (Avidin air) the cuvette was filled with water and then dried and the position of the dipole plasmon bands recorded and stored as the "zero reference". The center of a Gaussian curve fit was used as the band position. Then, each cuvette was re-filled and re-emptied with water eight more times and the position of the dipole plasmon bands measured in respect of the relative "zero reference". In the figure 23a below are shown the measurements of "zero reference" of main plasmon peak.

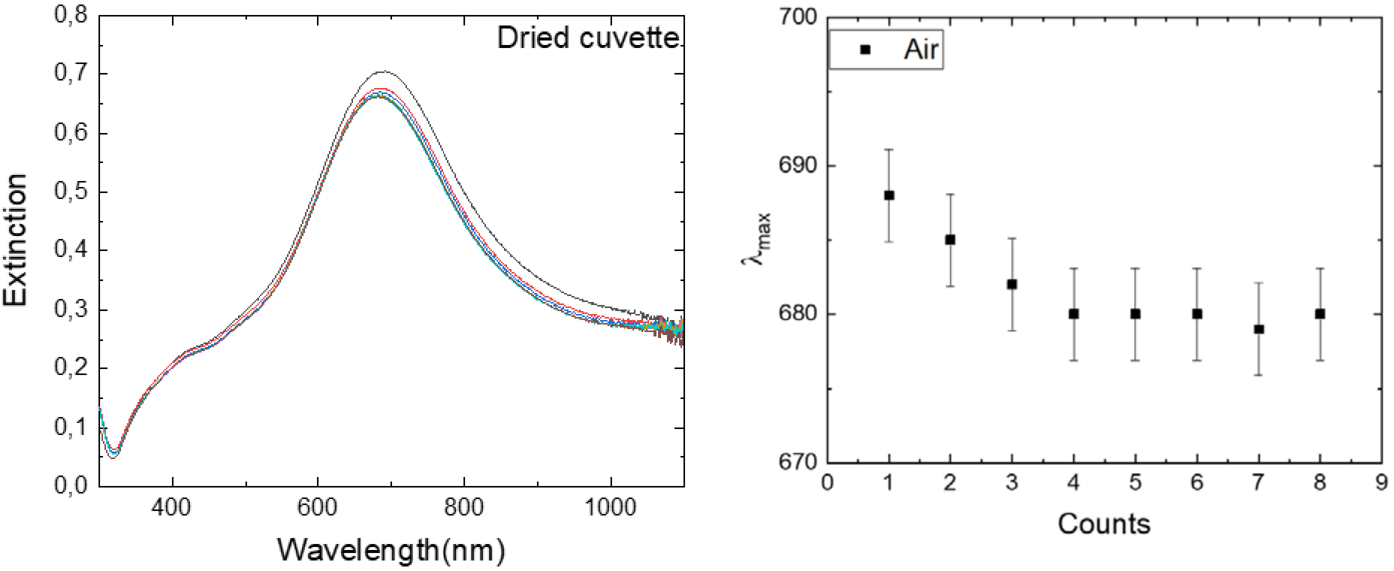

Figure 23: a) Zero reference measurements of main plasmon peak b) measurements with relative error bars of λ_{max}reproducibility value

By doing different cycle numbers of the spectra to the same cuvette by measuring λ_{max} signal, the reproducibility of $\Delta\lambda_{max}$ it was calculated, the corresponding value is equal to 3,1 nm. The slope value was obtained by doing linear regression of the linear interval present in the fit shown in figure 21b. With both slope and standard deviation corresponding to the reproducibility of $\Delta\lambda_{max}$ value the LOD is equal:

$$L.O.D = \frac{3S_{\Delta\lambda max}}{r} = 3{,}72 \cdot 10^{-8}M$$

We also tested the selectivity of the biotin sensor toward Bovine Serum Avidin and Avidin with air boundaries from egg with the results are shown in the figure below 24

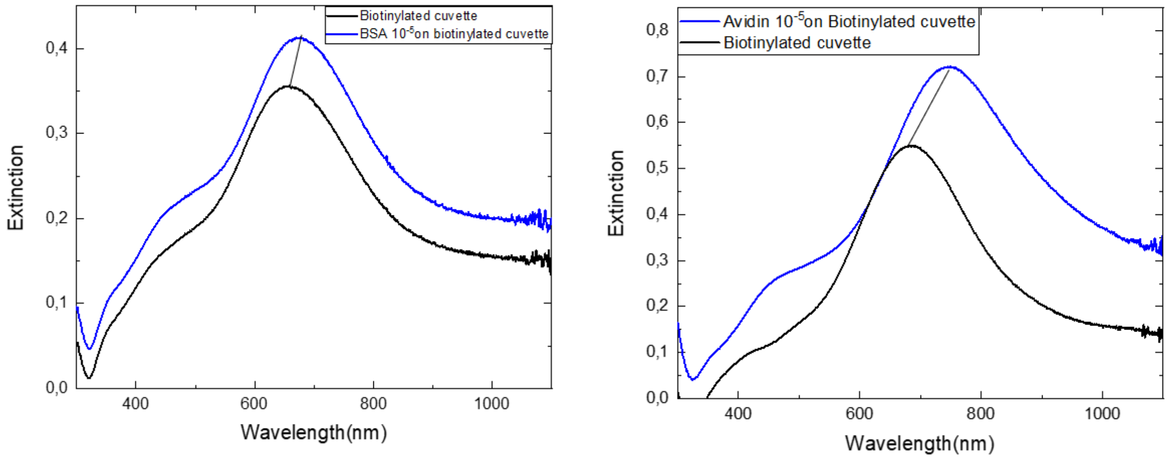

Figure 24: Selectivity measurements of BSA and Avidin from egg white

We tested the selectivity of the sensor by using the same protein concentration and as we can see from the figure the sensor gives two different plasmon response respectively a plasmon shift of 70 nm for Avidin and 15 nm for BSA. From the results we have demonstrated that the sensor is selective but not specific in relation to the concentration of two different species.

As seen in figure 22 in presence of the water as medium there is no sign of plasmon shift, probably there is no difference in refractive index between max protein concentrations at the surface so we have carried out numerical simulations. The simulation model was built basing on the following hypothesis:

- Avidin forms a uniform layer on the surface of the sensor.
- The effective refractive index value on the layer is an average value of the protein refractive index when the surface of the sensor is full of avidin molecules and the refractive index near to the glass surface sensor.

- The refractive index of the protein in saturation conditions is equal to the refractive index value of the water

In figure 25 are reported numerical simulations based on different refractive index values corresponding to different avidin layer thickness onto a single nanoparticle which represents the sensor

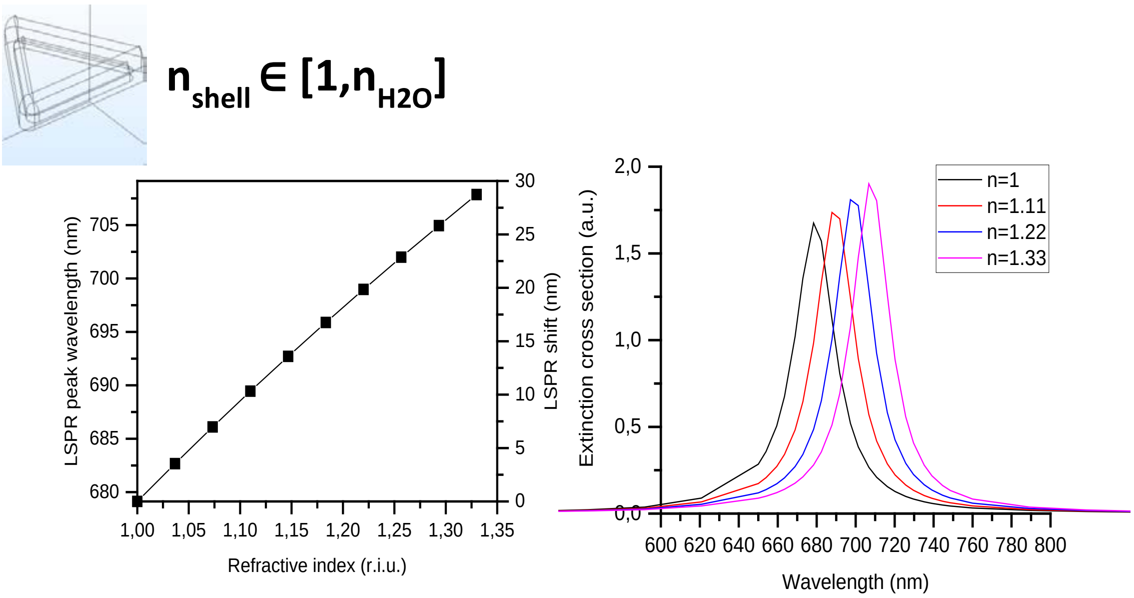

Figure 25: a) Schematic representation of avidin layer with refractive index values ranging from 1(air) to 1.33(water). b) Plasmon sensitivity values obtained by using the numerical model based on the previous hypothesis c) Plasmon resonance with different avidin layer thickness

As reported in figure 25 the numerical data obtained are in accordance with the experimental data obtained in figure 21. In conclusion the bio sensor so far discussed works when in the cuvette is not present any kind of solvent.

Conclusions

Sensors based on surface plasmon resonance(SPR) has received considerable attention due to their prompt responses and because they do not need complex and high cost instrumentation to work properly. In particular the high sensitivity of the plasmon band position due to refractive index changes is not only the most studied effect, but the most relevant one.

In the first part of this thesis, I have shown some different synthesis methodologies to produce anisotropic noble metal nanoparticles. Particularly the attention will be focused on the synthesis of anisotropic silver nanoparticles through seed mediated growth and laser ablation in liquids. Nanoparticles obtained with both methods will be characterized from optical e morphological point of view.

In the second part I have described the correlation between optical and morphological features of the produced nanosystems, while the third part I have presented the development of a sensor device, based on the plasmon sensitivity properties of silver anisotropic nanoparticles. The device presented is cost-effective, reusable, and high-responsive.

I used the same method for glass cuvettes for which specific biosensor device based on the biotin-avidin interaction is presented.

The results shown can serve as a first step and proof in order to develop low cost plasmonic sensor device based on refractive index changes suitable for a future integration and miniaturization.

References

1. Xia, Y., Xiong, Y., Lim, B. & Skrabalak, S. E. Cover Picture: Shape-Controlled Synthesis of Metal Nanocrystals: Simple Chemistry Meets Complex Physics? (Angew. Chem. Int. Ed. 1/2009). *Angewandte Chemie International Edition* **48**, 1–1 (2009).

2. Nehl, C. L. & Hafner, J. H. Shape-dependent plasmon resonances of gold nanoparticles. *J Mater Chem* **18**, 2415–2419 (2008).

3. Murphy, C. J. *et al.* Anisotropic metal nanoparticles: Synthesis, assembly, and optical applications. *Journal of Physical Chemistry B* **109**, 13857–13870 (2005).

4. Freestone, I., Meeks, N., Sax, M. & Higgitt, C. The Lycurgus Cup - A Roman nanotechnology. *Gold Bull* **40**, 270–277 (2008).

5. Barber, D. J. & Freestone, I. C. AN INVESTIGATION OF THE ORIGIN OF THE COLOUR OF THE LYCURGUS CUP BY ANALYTICAL TRANSMISSION ELECTRON MICROSCOPY. **32**, 33–45 (1990).

6. Bayda, S., Adeel, M., Tuccinardi, T., Cordani, M. & Rizzolio, F. The History of Nanoscience and Nanotechnology: From Chemical–Physical Applications to Nanomedicine. *Molecules 2020, Vol. 25, Page 112* **25**, 112 (2019).

7. Jana, N. R., Gearheart, L. & Murphy, C. J. Wet chemical synthesis of silver nanorods and nanowiresof controllable aspect ratio. *Chemical Communications* 617–618 (2001) doi:10.1039/B100521I.

8. Sau, T. K. & Murphy, C. J. Room temperature, high-yield synthesis of multiple shapes of gold nanoparticles in aqueous solution. *J Am Chem Soc* **126**, 8648–8649 (2004).

9. Jena, B. K. & Raj, C. R. Shape-controlled synthesis of gold nanoprism and nanoperiwinkles with pronounced electrocatalytic activity. *Journal of Physical Chemistry C* **111**, 15146–15153 (2007).

10. Zhao, Q., Hou, L., Huang, R. & Li, S. Controlled growth of gold nanowhiskers via a soft chemistry method. *Mater Chem Phys* **85**, 180–183 (2004).

11. Chen, J., Herricks, T. & Xia, Y. Polyol Synthesis of Platinum Nanostructures: Control of Morphology through the Manipulation of Reduction Kinetics. *Angewandte Chemie International Edition* **44**, 2589–2592 (2005).

12. Bakshi, M. S., Possmayer, F. & Petersen, N. O. Role of different phospholipids in the synthesis of pearl-necklace-type gold-silver bimetallic nanoparticles as bioconjugate materials. *Journal of Physical Chemistry C* **111**, 14113–14124 (2007).

13. Yang, S., Zhang, R., Wang, Q., Ding, B. & Wang, Y. Coral-shaped 3D assemblies of gold nuclei induced by UV irradiation and its disintegration. *Colloids Surf A Physicochem Eng Asp* **311**, 174–179 (2007).

14. Bououdina, M. Emerging research on bioinspired materials engineering. *Emerging Research on Bioinspired Materials Engineering* 1–441 (2016) doi:10.4018/978-1-4666-9811-6.

15. Kanitz, A. *et al.* Review on experimental and theoretical investigations of the early stage, femtoseconds to microseconds processes during laser ablation in liquid-phase for the synthesis of colloidal nanoparticles. *Plasma Sources Sci Technol* **28**, 103001 (2019).

16. Condorelli, M. *et al.* Plasmon sensing and enhancement of laser prepared silver colloidal nanoplates. *Appl Surf Sci* **475**, 633–638 (2019).

17. Laser Micro-Nano-Manufacturing and 3D Microprinting. **309**, (2020).

18. Kimling, J. *et al.* Turkevich method for gold nanoparticle synthesis revisited. *Journal of Physical Chemistry B* **110**, 15700–15707 (2006).

19. Thanh, N. T. K., Maclean, N. & Mahiddine, S. Mechanisms of nucleation and growth of nanoparticles in solution. *Chem Rev* **114**, 7610–7630 (2014).

20. Reches, M. & Gazit, E. Casting metal nanowires within discrete self-assembled peptide nanotubes. *Science (1979)* **300**, 625–627 (2003).

21. Djalali, R., Chen, Y. fou & Matsui, H. Au nanowire fabrication from sequenced histidine-rich peptide. *J Am Chem Soc* **124**, 13660–13661 (2002).

22. Yang, J., Elim, H. I., Zhang, Q. B., Lee, J. Y. & Ji, W. Rational synthesis, self-assembly, and optical properties of PbS-Au heterogeneous nanostructures via preferential deposition. *J Am Chem Soc* **128**, 11921–11926 (2006).

23. Chen, C. L., Zhang, P. & Rosi, N. L. A new peptide-based method for the design and synthesis of nanoparticle superstructures: Construction of highly ordered gold nanoparticle double helices. *J Am Chem Soc* **130**, 13555–13557 (2008).

24. Jones, M. R., Osberg, K. D., MacFarlane, R. J., Langille, M. R. & Mirkin, C. A. Templated techniques for the synthesis and assembly of plasmonic nanostructures. *Chem Rev* **111**, 3736–3827 (2011).

25. Poolakkandy, R. R. & Menamparambath, M. M. Soft-template-assisted synthesis: a promising approach for the fabrication of transition metal oxides. *Nanoscale Adv* **2**, 5015–5045 (2020).

26. Mayer, A. B. R., Grebner, W. & Wannemacher, R. Preparation of silver-latex composites. *Journal of Physical Chemistry B* **104**, 7278–7285 (2000).

27. Zhou, H. S., Honma, I., Komiyama, H. & Haus, J. W. Controlled synthesis and quantum-size effect in gold-coated nanoparticles. *Phys Rev B* **50**, 12052 (1994).

28. Barnickel, P. & Wokaun, A. Silver coated latex spheres. *http://dx.doi.org/10.1080/00268978900101861* **67**, 1355–1372 (2006).

29. Xu, Z., Hou, Y. & Sun, S. Magnetic core/shell Fe3O4/Au and Fe3O 4/Au/Ag nanoparticles with tunable plasmonic properties. *J Am Chem Soc* **129**, 8698–8699 (2007).

30. Tsang, S. C., Chen, Y. K., Harris, P. J. F. & Green, M. L. H. A simple chemical method of opening and filling carbon nanotubes. *Nature 1994 372:6502* **372**, 159–162 (1994).

31. Aherne, D., Ledwith, D. M., Gara, M. & Kelly, J. M. Optical Properties and Growth Aspects of Silver Nanoprisms Produced by a Highly Reproducible and Rapid Synthesis at Room Temperature. *Adv Funct Mater* **18**, 2005–2016 (2008).

32. Millstone, J. E., Métraux, G. S. & Mirkin, C. A. Controlling the Edge Length of Gold Nanoprisms via a Seed-Mediated Approach. *Adv Funct Mater* **16**, 1209–1214 (2006).

33. Pietrobon, B. & Kitaev, V. Photochemical synthesis of monodisperse size-controlled silver decahedral nanoparticles and their remarkable optical properties. *Chemistry of Materials* **20**, 5186–5190 (2008).

34. Xia, Y. *et al.* Seed-Mediated Growth Approach for Shape-Controlled Synthesis of Spheroidal and Rod-like Gold Nanoparticles Using a Surfactant Template**. *Physical Chemistry of Surfaces* **99**, 18 (1999).

35. Pietrobon, B., McEachran, M. & Kitaev, V. Synthesis of size-controlled faceted pentagonal silver nanorods with tunable plasmonic properties and self-assembly of these nanorods. *ACS Nano* **3**, 21–26 (2009).

36. Liu, M. & Guyot-Sionnest, P. Mechanism of silver(I)-assisted growth of gold nanorods and bipyramids. *Journal of Physical Chemistry B* **109**, 22192–22200 (2005).

37. Gole, A. & Murphy, C. J. Seed-mediated synthesis of gold nanorods: Role of the size and nature of the seed. *Chemistry of Materials* **16**, 3633–3640 (2004).

38. Senthil Kumar, P., Pastoriza-Santos, I., Rodríguez-González, B., Javier García De Abajo, F. & Liz-Marzán, L. M. High-yield synthesis and optical response of gold nanostars. *Nanotechnology* **19**, 015606 (2007).

39. Habas, S. E., Lee, H., Radmilovic, V., Somorjai, G. A. & Yang, P. Shaping binary metal nanocrystals through epitaxial seeded growth. *Nature Materials 2007 6:9* **6**, 692–697 (2007).

40. Sau, T. K. & Murphy, C. J. Role of ions in the colloidal synthesis of gold nanowires. *http://dx.doi.org/10.1080/14786430601110356* **87**, 2143–2158 (2007).

41. Jiang, X., Zeng, Q. & Yu, A. A self-seeding coreduction method for shape control of silver nanoplates. *Nanotechnology* **17**, 4929 (2006).

42. Liu, X., Huang, R. & Zhu, J. Functional faceted silver nano-hexapods: Synthesis, structure characterizations, and optical properties. *Chemistry of Materials* **20**, 192–197 (2008).

43. Bock, C., Paquet, C., Couillard, M., Botton, G. A. & MacDougall, B. R. Size-selected synthesis of PtRu nano-catalysts: Reaction and size control mechanism. *J Am Chem Soc* **126**, 8028–8037 (2004).

44. Kaabipour, S. & Hemmati, S. A review on the green and sustainable synthesis of silver nanoparticles and one-dimensional silver nanostructures. *Beilstein Journal of Nanotechnology 12:9* **12**, 102–136 (2021).

45. Bonet, F. *et al.* Electrochemical reduction of noble metal compounds in ethylene glycol. *International Journal of Inorganic Materials* **1**, 47–51 (1999).

46. Krichevski, O. & Markovich, G. Growth of colloidal gold nanostars and nanowires induced by palladium doping. *Langmuir* **23**, 1496–1499 (2007).

47. Shukla, S. *et al.* Porous gold nanospheres by controlled transmetalation reaction: A novel material for application in cell imaging. *Chemistry of Materials* **17**, 5000–5005 (2005).

48. Selvakannan, P. R. & Sastry, M. Hollow gold and platinum nanoparticles by a transmetallation reaction in an organic solution. *Chemical Communications* 1684–1686 (2005) doi:10.1039/B418566H.

49. Triangular Nanoframes Made of Gold and Silver | Nano Letters. https://pubs.acs.org/doi/full/10.1021/nl034097%2B.

50. Optical Properties of Metal Clusters - Uwe Kreibig, Michael Vollmer - Google Libri.

51. Brongersma M L and Kik P G, Surface Plasmon Nanophotonics... - Google Scholar.

52. Maier, S. A. Plasmonics: Metal nanostructures for subwavelength photonic devices. *IEEE Journal on Selected Topics in Quantum Electronics* **12**, 1214–1220 (2006).

53. Barnes, W. L., Dereux, A. & Ebbesen, T. W. Surface plasmon subwavelength optics. *Nature 2003 424:6950* **424**, 824–830 (2003).

54. Fritzsche, W. & Taton, T. A. Metal nanoparticles as labels for heterogeneous, chip-based DNA detection. *Nanotechnology* **14**, R63 (2003).

55. Hu, M. *et al.* Gold nanostructures: engineering their plasmonic properties for biomedical applications. *Chem Soc Rev* **35**, 1084–1094 (2006).

56. Eustis, S. & El-Sayed, M. A. Why gold nanoparticles are more precious than pretty gold: Noble metal surface plasmon resonance and its enhancement of the radiative and nonradiative properties of nanocrystals of different shapes. *Chem Soc Rev* **35**, 209–217 (2006).

57. Garcia, M. A. “Surface Plamons in biomedicine.” Recent... - Google Scholar.
.

58. Catchpole, K. R. *et al.* Plasmonics and nanophotonics for photovoltaics. *MRS Bull* **36**, 461–467 (2011).

59. Boltasseva, A. & Atwater, H. A. Low-Loss Plasmonic Metamaterials. *Science (1979)* **331**, 290–291 (2011).

60. Matheu, P., Lim, S. H., Derkacs, D., McPheeters, C. & Yu, E. T. Metal and dielectric nanoparticle scattering for improved optical absorption in photovoltaic devices. *Appl Phys Lett* **93**, 113108 (2008).

61. Narayanan, R. & El-Sayed, M. A. Catalysis with transition metal nanoparticles in colloidal solution: Nanoparticle shape dependence and stability. *Journal of Physical Chemistry B* **109**, 12663–12676 (2005).

62. Awazu, K. *et al.* A plasmonic photocatalyst consisting of silver nanoparticles embedded in titanium dioxide. *J Am Chem Soc* **130**, 1676–1680 (2008).

63. Larsson, E. M., Langhammer, C., Zorić, I. & Kasemo, B. Nanoplasmonic probes of catalytic reactions. *Science (1979)* **326**, 1091–1094 (2009).

64. Homola, J. & Piliarik, M. Surface Plasmon Resonance (SPR) Sensors. 45–67 (2006) doi:10.1007/5346_014.

65. Ozbay, E. Plasmonics: Merging Photonics and Electronics at Nanoscale Dimensions. *Science (1979)* **311**, 189–193 (2006).

66. Garcia, M. A. Surface plasmons in metallic nanoparticles: fundamentals and applications. *J Phys D Appl Phys* **44**, 283001 (2011).

67. Leatherdale, C. A., Woo, W. K., Mikulec, F. v. & Bawendi, M. G. On the absorption cross section of CdSe nanocrystal quantum dots. *Journal of Physical Chemistry B* **106**, 7619–7622 (2002).

68. Jia, W., Douglas, E. P., Guo, F. & Sun, W. Optical limiting of semiconductor nanoparticles for nanosecond laser pulses. *Appl Phys Lett* **85**, 6326 (2004).

69. Mie, G. Beiträge zur Optik trüber Medien, speziell kolloidaler Metallösungen. *Ann Phys* **330**, 377–445 (1908).

70. Hövel, H., Fritz, S., Hilger, A., Kreibig, U. & Vollmer, M. Width of cluster plasmon resonances: Bulk dielectric functions and chemical interface damping. *Phys Rev B* **48**, 18178 (1993).

71. Ji, X. *et al.* Size control of gold nanocrystals in citrate reduction: The third role of citrate. *J Am Chem Soc* **129**, 13939–13948 (2007).

72. Compagnini, G. *et al.* Growth kinetics and sensing features of colloidal silver nanoplates. *J Nanomater* **2019**, (2019).

73. Crystallization - J W Mullin - Google Libri.

74. Strey, R., Wagner, / P E & Viisanen, Y. The Problem of Measuring Homogeneous Nucleation Rates and the Molecular Contents of Nuclei: Progress in the Form of Nucleation Pulse Measurements. *J. Phys. Chem* **98**, 7748–7758 (1994).

75. Speliotis, D. E. Magnetic recording beyond the first 100 Years. *J Magn Magn Mater* **193**, 29–35 (1999).

76. Monodispersed Particles - Tadao Sugimoto - Google Libri.

77. T. Sugimoto , Adv. Colloid Interfac. Sci. 1987 , 28 , 65 - Google Scholar.

78. Talapin, D. v., Rogach, A. L., Haase, M. & Weller, H. Evolution of an ensemble of nanoparticles in a colloidal solution: Theoretical study. *Journal of Physical Chemistry B* **105**, 12278–12285 (2001).

79. Talapin, D. v. *et al.* Dynamic distribution of growth rates within the ensembles of colloidal II-VI and III-V semiconductor nanocrystals as a factor governing their photoluminescence efficiency. *J Am Chem Soc* **124**, 5782–5790 (2002).

80. Kabalnov, A. S. & Shchukin, E. D. Ostwald ripening theory: applications to fluorocarbon emulsion stability. *Adv Colloid Interface Sci* **38**, 69–97 (1992).

81. Kilin, D. S., Prezhdo, O. v. & Xia, Y. Shape-controlled synthesis of silver nanoparticles: Ab initio study of preferential surface coordination with citric acid. *Chem Phys Lett* **458**, 113–116 (2008).

82. Nikoobakht, B. & El-Sayed, M. A. Preparation and growth mechanism of gold nanorods (NRs) using seed-mediated growth method. *Chemistry of Materials* **15**, 1957–1962 (2003).

83. Haes, A. J. & van Duyne, R. P. A nanoscale optical biosensor: Sensitivity and selectivity of an approach based on the localized surface plasmon resonance spectroscopy of triangular silver nanoparticles. *J Am Chem Soc* **124**, 10596–10604 (2002).

84. Xia, Y., Gilroy, K. D., Peng, H. C. & Xia, X. Seed-Mediated Growth of Colloidal Metal Nanocrystals. *Angewandte Chemie International Edition* **56**, 60–95 (2017).

85. Agnihotri, S., Mukherji, S. & Mukherji, S. Size-controlled silver nanoparticles synthesized over the range 5–100 nm using the same protocol and their antibacterial efficacy. *RSC Adv* **4**, 3974–3983 (2013).

86. Xiao, M. *et al.* Plasmon-enhanced chemical reactions. *J Mater Chem A Mater* **1**, 5790–5805 (2013).

87. Zhang, X. Y. *et al.* Self-assembly of large-scale and ultrathin silver nanoplate films with tunable plasmon resonance properties. *ACS Nano* **5**, 9082–9092 (2011).

88. Miller, M. M. & Lazarides, A. A. Sensitivity of metal nanoparticle surface plasmon resonance to the dielectric environment. *Journal of Physical Chemistry B* **109**, 21556–21565 (2005).

89. Liu, Y. *et al.* Precision Synthesis: Designing Hot Spots over Hot Spots via Selective Gold Deposition on Silver Octahedra Edges. *Small* **10**, 4940–4950 (2014).

90. Saison-Francioso, O., Lévêque, G., Boukherroub, R., Szunerits, S. & Akjouj, A. Dependence between the Refractive-Index Sensitivity of Metallic Nanoparticles and the Spectral Position of Their Localized Surface Plasmon Band: A Numerical and Analytical Study. *Journal of Physical Chemistry C* **119**, 28551–28559 (2015).

91. Saison-Francioso, O., Lévêque, G., Boukherroub, R., Szunerits, S. & Akjouj, A. Dependence between the Refractive-Index Sensitivity of Metallic Nanoparticles and the Spectral Position of Their Localized Surface Plasmon Band: A Numerical and Analytical Study. *Journal of Physical Chemistry C* **119**, 28551–28559 (2015).

92. Johnson, P. B. & Christy, R. W. Optical Constants of the Noble Metals. *Phys Rev B* **6**, 4370 (1972).

93. Waxenegger, J., Trügler, A. & Hohenester, U. Plasmonics simulations with the MNPBEM toolbox: Consideration of substrates and layer structures. *Comput Phys Commun* **193**, 138–150 (2015).

94. Hohenester, U. & Trügler, A. MNPBEM – A Matlab toolbox for the simulation of plasmonic nanoparticles. *Comput Phys Commun* **183**, 370–381 (2012).

95. Trügler, A. Optical Properties of Metallic Nanoparticles. **232**, (2016).

96. Chen, H., Kou, X., Yang, Z., Ni, W. & Wang, J. Shape- and size-dependent refractive index sensitivity of gold nanoparticles. *Langmuir* **24**, 5233–5237 (2008).

97. Condorelli, M. *et al.* Silver nanoplates paved PMMA cuvettes as a cheap and re-usable plasmonic sensing device. *Appl Surf Sci* **566**, 150701 (2021).

98. Tang, B., Sun, L., Li, J., Zhang, M. & Wang, X. Sunlight-driven synthesis of anisotropic silver nanoparticles. *Chemical Engineering Journal* **260**, 99–106 (2015).

99. Zhang, D. & Wada, H. Laser Ablation in Liquids for Nanomaterial Synthesis and Applications. *Handbook of Laser Micro- and Nano-Engineering* 1–35 (2021) doi:10.1007/978-3-319-69537-2_30-1.

100. Park, H. *et al.* Synthesis of Ultra-Small Palladium Nanoparticles Deposited on CdS Nanorods by Pulsed Laser Ablation in Liquid: Role of Metal Nanocrystal Size in the Photocatalytic Hydrogen Production. *Chemistry – A European Journal* **23**, 13112–13119 (2017).

101. Fazio, E. *et al.* Iron oxide nanoparticles prepared by laser ablation: Synthesis, structural properties and antimicrobial activity. *Colloids Surf A Physicochem Eng Asp* **490**, 98–103 (2016).

102. Fazio, E. *et al.* Nonlinear scattering and absorption effects in size-selected diphenylpolyynes. *Journal of Physical Chemistry C* **118**, 28812–28819 (2014).

103. Fazio, E., Neri, F., Patan, S., D'Urso, L. & Compagnini, G. Optical limiting effects in linear carbon chains. *Carbon N Y* **49**, 306–310 (2011).

104. Fazio, E. *et al.* Nanoparticles Engineering by Pulsed Laser Ablation in Liquids: Concepts and Applications. *Nanomaterials 2020, Vol. 10, Page 2317* **10**, 2317 (2020).

105. Casavola, A. *et al.* Experimental investigation and modelling of double pulse laser induced plasma spectroscopy under water. *Spectrochim Acta Part B At Spectrosc* **60**, 975–985 (2005).

106. Amendola, V. & Meneghetti, M. What controls the composition and the structure of nanomaterials generated by laser ablation in liquid solution? *Physical Chemistry Chemical Physics* **15**, 3027–3046 (2013).

107. Stamplecoskie, K. Silver Nanoparticle Controlled Synthesis and Implications in Spectroscopy, Biomedical and Optoelectronics Applications. (2013) doi:10.20381/RUOR-3005.

108. Rocha, T. C. R. & Zanchet, D. Structural defects and their role in the growth of ag triangular nanoplates. *Journal of Physical Chemistry C* **111**, 6989–6993 (2007).

109. Chimentão, R. J. *et al.* Different morphologies of silver nanoparticles as catalysts for the selective oxidation of styrene in the gas phase. *Chemical Communications* **4**, 846–847 (2004).

110. Jin, R. *et al.* Controlling anisotropic nanoparticle growth through plasmon excitation. *Nature 2003 425:6957* **425**, 487–490 (2003).

111. Elechiguerra, J. L., Reyes-Gasga, J. & Yacaman, M. J. The role of twinning in shape evolution of anisotropic noble metal nanostructures. *J Mater Chem* **16**, 3906–3919 (2006).

112. Parnklang, T. *et al.* H2O2-triggered shape transformation of silver nanospheres to nanoprisms with controllable longitudinal LSPR wavelengths. *RSC Adv* **3**, 12886–12894 (2013).

113. Introduction to Comsol Multiphysics ® Contact Information. (1998).

114. Yunus, W. M. bin M. & Rahman, A. bin A. Refractive index of solutions at high concentrations. *Applied Optics, Vol. 27, Issue 16, pp. 3341-3343* **27**, 3341–3343 (1988).

115. Potara, M., Gabudean, A. M. & Astilean, S. Solution-phase, dual LSPR-SERS plasmonic sensors of high sensitivity and stability based on chitosan-coated anisotropic silver nanoparticles. *J Mater Chem* **21**, 3625–3633 (2011).

116. Paramelle, D. *et al.* A rapid method to estimate the concentration of citrate capped silver nanoparticles from UV-visible light spectra. *Analyst* **139**, 4855–4861 (2014).

117. Chen, G., Roy, I., Yang, C. & Prasad, P. N. Nanochemistry and Nanomedicine for Nanoparticle-based Diagnostics and Therapy. *Chem Rev* **116**, 2826–2885 (2016).

118. He, G. S., Tan, L. S., Zheng, Q. & Prasad, P. N. Multiphoton absorbing materials: Molecular designs, characterizations, and applications. *Chem Rev* **108**, 1245–1330 (2008).

119. Zipfel, W. R., Williams, R. M. & Webb, W. W. Nonlinear magic: multiphoton microscopy in the biosciences. *Nature Biotechnology 2003 21:11* **21**, 1369–1377 (2003).

120. Mout, R., Moyano, D. F., Rana, S. & Rotello, V. M. Surface functionalization of nanoparticles for nanomedicine. *Chem Soc Rev* **41**, 2539–2544 (2012).

121. Boca, S. C. *et al.* Chitosan-coated triangular silver nanoparticles as a novel class of biocompatible, highly effective photothermal transducers for in vitro cancer cell therapy. *Cancer Lett* **311**, 131–140 (2011).

122. Bertorelle, F. *et al.* Safe core-satellite magneto-plasmonic nanostructures for efficient targeting and photothermal treatment of tumor cells. *Nanoscale* **10**, 976–984 (2018).

123. Jimenez de Aberasturi, D., Henriksen-Lacey, M., Litti, L., Langer, J. & Liz-Marzán, L. M. Using SERS Tags to Image the Three-Dimensional Structure of Complex Cell Models. *Adv Funct Mater* **30**, 1909655 (2020).

124. Ko, S. H. *et al.* Direct nanoimprinting of metal nanoparticles for nanoscale electronics fabrication. *Nano Lett* **7**, 1869–1877 (2007).

125. Chen, J. S., Chen, P. F., Lin, H. T. H. & Huang, N. T. A Localized surface plasmon resonance (LSPR) sensor integrated automated microfluidic system for multiplex inflammatory biomarker detection. *Analyst* **145**, 7654–7661 (2020).

126. Begines, B. *et al.* Design of highly stabilized nanocomposite inks based on biodegradable polymer-matrix and gold nanoparticles for inkjet printing. doi:10.1038/s41598-019-52314-2.

127. Berger, C. E. H., Beumer, T. A. M., Kooyman, R. P. H. & Greve, J. Surface Plasmon Resonance Multisensing. *Anal Chem* **70**, 703–706 (1998).

128. Heaton, R. J., Peterson, A. W. & Georgiadis, R. M. Electrostatic surface plasmon resonance: Direct electric field-induced hybridization and denaturation in monolayer nucleic acid films and label-free discrimination of base mismatches. *Proceedings of the National Academy of Sciences* **98**, 3701–3704 (2001).

129. Johnson, . R P *et al.* Electron beam lithography designed silver nano-disks used as label free nano-biosensors based on localized surface plasmon resonance. *Optics Express, Vol. 20, Issue 3, pp. 2587-2597* **20**, 2587–2597 (2012).

130. Serrano, A. *et al.* Ag-AgO nanostructures on glass substrates by solid-state dewetting: From extended to localized surface plasmons. *J Appl Phys* **124**, 133103 (2018).

131. le Bris, A., Maloum, F., Teisseire, J. & Sorin, F. Self-organized ordered silver nanoparticle arrays obtained by solid state dewetting. *Appl Phys Lett* **105**, 203102 (2014).

132. Ye, J., Zuev, D. & Makarov, S. Dewetting mechanisms and their exploitation for the large-scale fabrication of advanced nanophotonic systems. *https://doi.org/10.1080/09506608.2018.1543832* **64**, 439–477 (2018).

133. Łapiński, M., Kozioł, R., Cymann, A., Sadowski, W. & Kościelska, B. Substrate Dependence in the Formation of Au Nanoislands for Plasmonic Platform Application. *Plasmonics* **15**, 101–107 (2020).

134. Oh, H., Pyatenko, A. & Lee, M. A hybrid dewetting approach to generate highly sensitive plasmonic silver nanoparticles with a narrow size distribution. *Appl Surf Sci* **542**, 148613 (2021).

135. Lin, H. K., Huang, C. W., Lin, Y. H., Chuang, W. S. & Huang, J. C. Effects of Accumulated Energy on Nanoparticle Formation in Pulsed-Laser Dewetting of AgCu Thin Films. *Nanoscale Res Lett* **16**, 110 (2021).

136. Hu, X., Cahill, D. G. & Averback, R. S. Nanoscale pattern formation in Pt thin films due to ion-beam-induced dewetting. *Appl Phys Lett* **76**, 3215 (2000).

137. Kojima, Y. & Kato, T. Nanoparticle formation in Au thin films by electron-beam-induced dewetting. *Nanotechnology* **19**, 255605 (2008).

138. Rusciano, G., Capaccio, A., Martinez, A. & Sasso, A. Nanoporous silver films produced by solid-state dewetting for SERS applications. *https://doi.org/10.1117/12.2592391* **11772**, 32–36 (2021).

139. Herzer, N., Hoeppener, S. & Schubert, U. S. Fabrication of patterned silane based self-assembled monolayers by photolithography and surface reactions on silicon-oxide substrates. *Chemical Communications* **46**, 5634–5652 (2010).

140. Donley, C. L. *et al.* Thin Films of Polymerized Rodlike Phthalocyanine Aggregates †. (2003) doi:10.1021/LA034271.

141. Terracciano, M., Rea, I., Politi, J. & de Stefano, L. Optical characterization of aminosilane-modified silicon dioxide surface for biosensing. *J Eur Opt Soc Rapid Publ* **8**, 13075 (2013).

142. Klug, J., Pérez, L. A., Coronado, E. A. & Lacconi, G. I. Chemical and electrochemical oxidation of silicon surfaces functionalized with APTES: The role of surface roughness in the AuNPs anchoring kinetics. *Journal of Physical Chemistry C* **117**, 11317–11327 (2013).

143. Zhang, X. Y. *et al.* Self-assembly of large-scale and ultrathin silver nanoplate films with tunable plasmon resonance properties. *ACS Nano* **5**, 9082–9092 (2011).

144. Compagnini, G. *et al.* Growth kinetics and sensing features of colloidal silver nanoplates. *J Nanomater* **2019**, (2019).

145. Zhang, X. Y. *et al.* Self-assembly of large-scale and ultrathin silver nanoplate films with tunable plasmon resonance properties. *ACS Nano* **5**, 9082–9092 (2011).

146. Loock, H. P. & Wentzell, P. D. Detection limits of chemical sensors: Applications and misapplications. *Sens Actuators B Chem* **173**, 157–163 (2012).

147. Meza-Sánchez, D. E., Maravillas-Montero, J. L. & Luis Maravillas-Montero, J. Clinical and Biomedical Applications of Surface Plasmon Resonance Systems. doi:10.24875/RIC.18002754.

148. Mousavi, M. Z. *et al.* Urinary micro-RNA biomarker detection using capped gold nanoslit SPR in a microfluidic chip. *Analyst* **140**, 4097–4104 (2015).

149. Singh, P. SPR Biosensors: Historical Perspectives and Current Challenges. *Sens Actuators B Chem* **229**, 110–130 (2016).

150. Mody, V. v., Siwale, R., Singh, A. & Mody, H. R. Introduction to metallic nanoparticles. *J Pharm Bioallied Sci* **2**, 282 (2010).

151. Lee, J., Lee, K. & Park, S. S. Environmentally friendly preparation of nanoparticle-decorated carbon nanotube or graphene hybrid structures and their potential applications. *Journal of Materials Science 2015 51:6* **51**, 2761–2770 (2015).

152. Kyaw, H. H., Al-Harthi, S. H., Sellai, A. & Dutta, J. Self-organization of gold nanoparticles on silanated surfaces. *Beilstein Journal of Nanotechnology* **6**, 2345 (2015).

153. Acres, R. G. *et al.* Molecular structure of 3-aminopropyltriethoxysilane layers formed on silanol-terminated silicon surfaces. *Journal of Physical Chemistry C* **116**, 6289–6297 (2012).

154. ben Haddada, M. *et al.* Optimizing the immobilization of gold nanoparticles on functionalized silicon surfaces: Amine- vs thiol-terminated silane. *Gold Bull* **46**, 335–341 (2013).

155. and, A. J. H. & Duyne*, R. P. van. A Nanoscale Optical Biosensor: Sensitivity and Selectivity of an Approach Based on the Localized Surface Plasmon Resonance Spectroscopy of Triangular Silver Nanoparticles. *J Am Chem Soc* **124**, 10596–10604 (2002).

Ringraziamenti

Desidero ringraziare mia madre, la mia famiglia, i miei più cari amici, il professore Compagnini e i miei colleghi di lavoro per tutto il supporto datomi in questo percorso di dottorato.